QUANTITATIVE METALLOGRAPHY, OPTIMIZATION OF HVHPDC PROCESSES AND MODELLING SOLUTE HOMOGENIZATION DURING SOLUTIONIZING OF Al-4Zn-1Mg-1.2Fe-0.1Ti ALLOY

QUANTITATIVE METALLOGRAPHY, OPTIMIZATION OF HVHPDC PROCESSES AND MODELLING SOLUTE HOMOGENIZATION DURING SOLUTIONIZING OF Al-4Zn-1Mg-1.2Fe-0.1Ti ALLOY

By: CHUFAN WU B. Eng.

A THESIS SUBMITTED TO THE SCHOOL OF GRADUATE STUDIES IN PARTIAL FULFILLMENT OF THE REQUIREMENTS FOR THE DEGREE OF MASTER OF APPLIED SCIENCE

MASTER OF APPLIED SCIENCE (2019)
McMaster University, Hamilton, Ontario

TITLE: Quantitative Metallography, Optimization of HVHPC Process and Modelling Solute Homogenization During Solutionizing of *Al-4Zn-1Mg-1.2Fe-0.1Ti* Alloy

Author: Chufan Wu
B. Eng (Materials Science and Engineering)
McMaster University, Hamilton, ON, Canada

Supervisor: Sumanth Shankar
Department of Mechanical Engineering
McMaster University, Hamilton, ON, Canada

Number of Pages: xii, 113

Acknowledgements

I would like to express my deepest gratitude to my supervisor, Sumanth Shankar, for his consistent help throughout my studies. He has taught me the power of thinking with an open mind and to always question what I think I know. He has given me lots of guidance and sparked numerous new ideas through our endless hours of discussions, and he will always be a strong motivation for me. Thank you for giving an unforgettable experience at LMCRC and McMaster University.

I would also like to thank Dr. Xiaochun Zeng for his training, expertise, and guidance throughout my experimental trials. His knowledge, patience, and organization proved to be of tremendous help in accurately and efficiently performing experiments. I would like to also extend my thanks to Mr. Mohamed Salim for his help with writing the MATLAB code for the homogenization model.

My sincere gratitude goes to my industry partners at Nemak, Glenn Byczynski, Anthony Lombardi, and Alan Gonzalez for their knowledgeable inputs and insightful ideas through our teleconference meetings. My deepest gratitude also goes to Dr. Kumar Sadayappan, Mr. Gabriel Birsan and Mr. Frank Benkel for their casting experience and help with high pressure die casting trials at CANMETMaterials.

Special thank you to the technicians at the Mechanical Engineering Machine Lab, especially Mr. Michael Lee for training me to use the milling machine and CNC machine and writing the program for machining the tensile bars. I am also thankful for for Mr. Doug Culley and Dr. Xiaogang Li from the Department of Materials Engineering for their insights on sample preparation and training on optical microscopy. Special thanks to Mr. Chris Butcher from the Canadian Centre of Electron Microscopy (CCEM) for his various microscopy and sample preparation training.

I am very grateful for Ontario Centre of Excellence (OCE) for providing me with the financial support needed to complete my project I would also like to thank CANMETMaterials for letting me use their facilities.

Last but certainly not least, thank you to my parents and friends for their endless support.

Abstract

High pressure die casting (HPDC) is both a cost-efficient and high throughput method for making near-net shape castings. 7xxx series aluminum alloys are excellent candidates for manufacturing structural components for significant light-weighting opportunities in the automotive industry. This project explores the development of a new 7xxx series aluminum alloy with iron additions to improve castability. The main objective of this project is to develop an optimized heat treatment process for the new Al-Zn-Mg-Fe alloy to achieve solute homogenization in the primary Al grains.

The rationale behind adding iron as an alloying element was presented, as well as an analysis of the Al-Fe intermetallic phases to show their mitigating effects on hot tearing.

A detailed analysis of the casting quality was carried out, including detailed microstructural analyses of defects and defect-free castings, correlating process parameters, shot profiles, uniaxial tensile properties, and fractography. Improvements on casting conditions and parameters were suggested.

Solution heat treatments were carried out between 0.25 and 24 hours and quenched with forced air. Bulk hardness measurements were obtained following solution heat treatment to determine the arrest times for the precipitation reactions during natural aging. The uniaxial tensile properties of the alloy in the F- and T4-tempers were presented. Microstructural analyses of the alloy were carried out by optical and electron microscopy (SEM), including phase identification, phase fraction, average grain size, and distribution.

A predictive model for the homogenization of the solutes in the Al matrix was developed using a one-dimensional diffusion model with spherical geometry, and a MATLAB code was developed to time for complete homogenization. Electron-dispersive X-ray spectroscopy (EDX) line scans were carried out on the F and T4 samples (0.25-2h) and the concentration profiles of Zn and Mg (the diffusing solutes) were extracted and analyzed. The models were verified and validated with experiment data.

Table of Contents

List of Figures

List of Tables

Chapter 1 INTRODUCTION

Climate change is affecting the entire world. In the Paris Summit of 2015, global efforts were set in place to reduce the emission of greenhouse gases (GHG) [1]. One of the most prevalent sources of GHG emissions is from the use of fossil fuels. Studies from the United States Environmental Protection Agency (EPA) have determined that the transportation sector is responsible for releasing approximately 29% of all CO_2 emissions globally from 1960 to 2014 [2]. Efforts to reduce carbon emissions are crucial for the automotive industry, in order to comply with the new environmental policies. Recent developments have mainly focused on the goal of decreasing the environmental impact of vehicles through lightweighting. A report from MIT in 2008 concluded that for every 100kg reduction in weight, the fuel consumption will decrease by 0.4L/100km [3]. The EPA has predicted that light-duty vehicles produced between 2017 and 2025 would have to reduce carbon emissions by 2 billion metric tonnes. These vehicles are mandated to reduce the consumption of fossil fuels by 4 billion barrels over their lifetime [3]. The mandated fuel economy for vehicles in 2025 is an average of 54.5 miles per gallon [4]. One of the most effective methods of increasing fuel efficiency is by significant reduction in the curb weight of vehicles.

Aluminum alloys are favourable candidates for lightweighting due to their high strength-to-weight ratios compared to their steel counterparts. Depending on the alloying elements, aluminum alloys can have variety of mechanical properties, from high ductility to high strength. Table 1-1 shows a list of the mechanical properties. According to the United States Geographical Survey (USGS) in 2005, approximately 87.3% of the curb weight of an average vehicle produced in the 1970s was from steel components, compared to 66.4% in 2004 [1]. Figure 1-1 shows the change in aluminum content from 1973 (81 lbs per vehicle) to 2002 (274 lbs per vehicle) in cars and trucks [5]. It is predicted that by 2028, vehicles will have an average of 7% (270 pounds) mass reduction and over five million vehicles will have nearly 850 pounds of total aluminum content or greater [3]. Despite the attractive advantages of these alloys, they are not widely used for two main reasons: the cost of aluminum is twice as much as steel, and the difficulties in manufacturing car components in large-scale production [3]. The production cost of aluminum alloys can be mitigated by recycling and reusing previous components. Furthermore, aluminum alloys are routinely studied and cast by every known process, which offers large volume and variability of components. Affordable, large-scale production with high dimensional accuracy can be obtained by high pressure die casting (HPDC).

HPDC is a near-net shape casting technique. During this process, molten metal is forced into a pre-heated die cavity with a large pressure, travelling at speeds of 20-45 m/s into water-cooled dies [5,6,7]. The metal is held under extreme pressure for rapid solidification, typically 100 to 200 °C/s. After which, the die is unlocked, and the casting ejected [6,7]. The process times are typically less than a minute [8]. HPDC allows components to be manufactured rapidly and at a large-scale with minimal post processing. It remains a very cost-effective and efficient method of mass-production.

Table 1-1: Typical ranges of mechanical properties of commercial aluminum alloys [5].

Tensile Strength (MPa)	70-505
Yield Strength (MPa)	20-455
Elongation (%)	<1-30

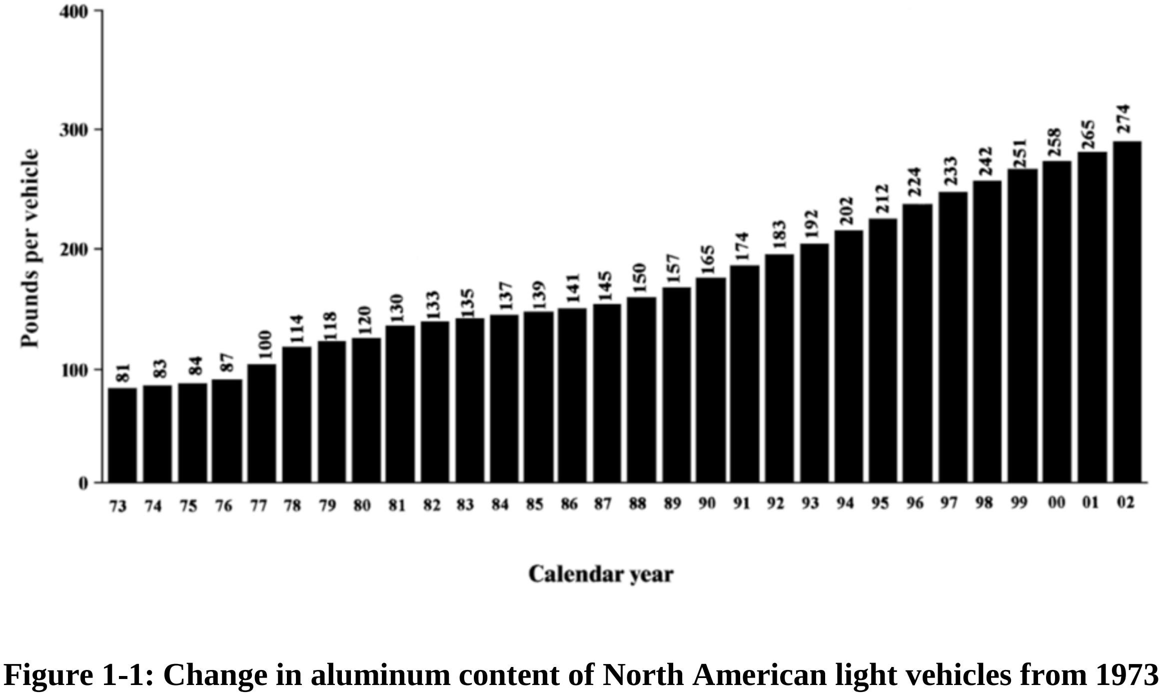

Figure 1-1: Change in aluminum content of North American light vehicles from 1973 to 2002 [5].

The most commonly used aluminum casting alloys for automotive applications are from the 200 and 300 series, from the Al-Cu and Al-Si-Mg systems, respectively [9]. These systems are well-studied and widely used due to their high fluidity at elevated temperature and resistance to hot tearing. Additionally, these alloys meet the ductility requirement needed for structural automotive components. An example from the Al-Si-Mg family for HPDC applications is Silafont-36 or also named A365. Table 1-2 shows its mechanical properties in multiple tempers for A365 alloy castings [10]. There are a few drawbacks that limit the widespread use of Al-Si-Mg alloys. Firstly, they are not completely recyclable, which increases its production cost and its environmental impacts. Secondly, they are not suitable for structural lightweighting applications due to their low tensile and yield strengths. For these alloys to replace their steel counterparts, one would need to increase the thickness of the component, thus defeating its low-density advantage.

Table 1-2: The typical mechanical properties of A365 Alloy [10].

Tempers	Tensile Strength (MPa)	Yield Strength (MPa)	Elongation (%)
F	250-290	120-150	5-11
T4	210-260	95-140	15-22
T6	290-340	210-280	7-12
T7	120-170	200-240	15-20

7xxx series alloys are the ideal candidate for lightweighting; they have the same low-density advantages and much higher strengths compared to their Al-Si-Mg alloy counterparts. They are also heat treatable and age hardenable, giving them a significantly larger range of mechanical properties. However, they are not widely used for casting applications due to their tendency to hot tear and render the castings unusable. The research team at the Light Metal Casting Research Centre (LMCRC) in McMaster University has created a new castable 7xxx series alloy (Al-Zn-Mg) with Fe additions to be used specifically for HPDC processes. Traditional heat treatments for these alloys can range from 24-48 hours, which is not viable for the automotive industry due to their added costs in large-scale production environments. The objective of my current research is to determine a short solution treatment process to increase the mechanical properties of the Al-Zn-Mg-Fe alloy and maintain feasibility for mass production.

Chapter 2 PROJECT OBJECTIVES AND STRATEGY

The overarching goal of the project is to establish a short solution treatment for the newly-developed Al-Zn-Mg-Fe family of alloys. Since they are newly developed, it was imperative to first study their mechanical and microstructural behaviour under a wide set of conditions to determine their suitability for HPDC application. Following this thought process; the following three objectives were laid out for the project:

- Quantitative microstructure analyses of the Al-4Zn-1Mg-1.2Fe-0.1Ti (all in weight percentage) alloy castings from the HVHPDC (High Vacuum High Pressure Die Casting) process. The characterization was carried out for as-cast (F) samples and those solutionized at 475 ˚C (T4) for various times intervals ranging from 0.25 h to 24 h.
- Identify relationships between microstructure of castings, mechanical properties, and the critical casting process variables.
- Develop and solve a mathematical model to predict the diffusion kinetics of Zn and Mg solutes in the primary Al grains during solution treatment at high temperature.

2.1 *Project Strategy*

Figure 2-1 presents the project strategy as a process flow chart; wherein, the characterization of microstructure and uniaxial tensile properties were carried out on the samples obtained from the corrosion plate and tensile bar castings, discussed in Section 4.1 Casting Process.

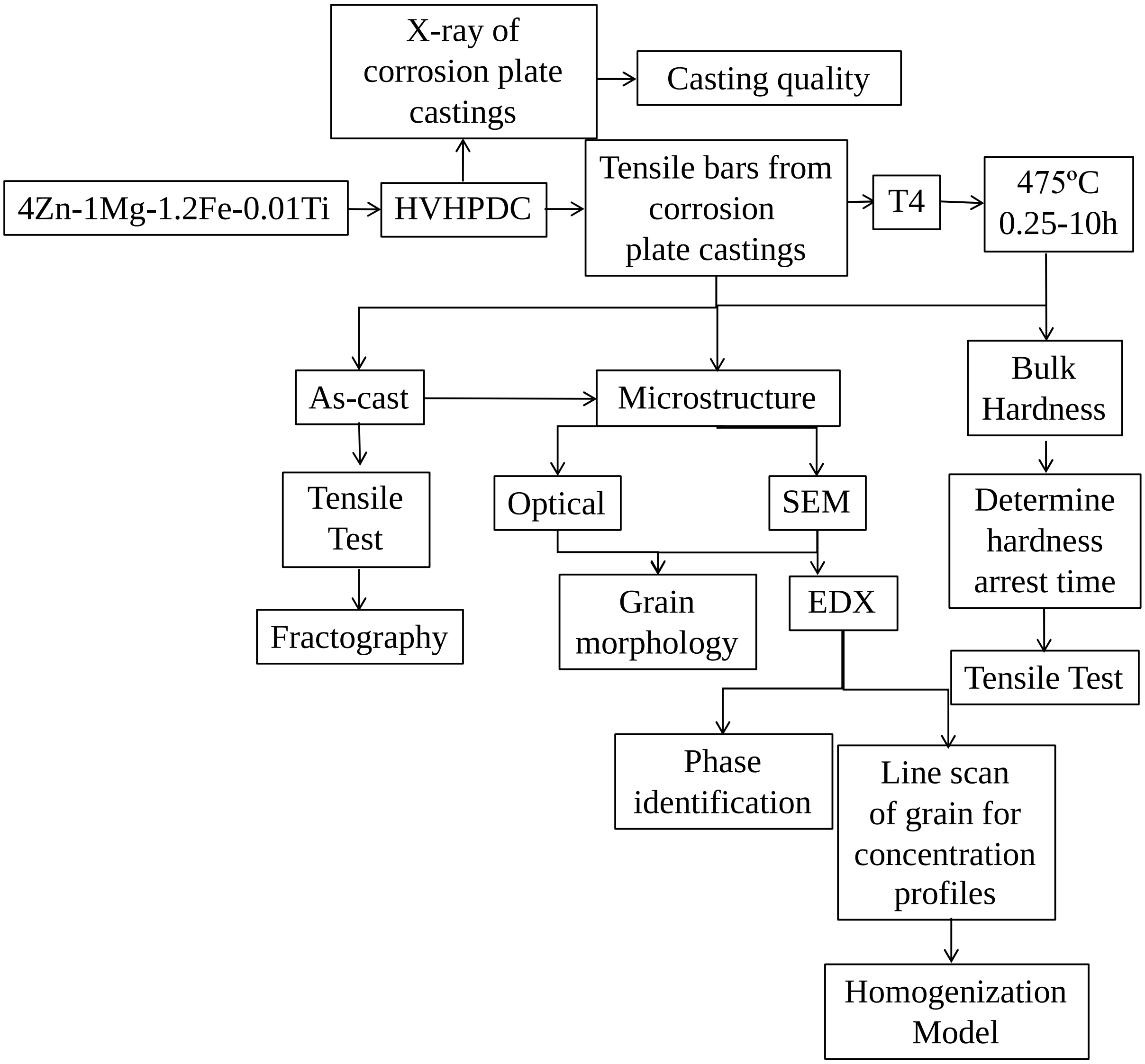
X-ray of corrosion plate castings
Casting quality
4Zn-1Mg-1.2Fe-0.01Ti
HVHPDC
Tensile bars from corrosion plate castings
T4
475ºC 0.25-10h
As-cast
Microstructure
Bulk Hardness
Tensile Test
Optical
SEM
Determine hardness arrest time
Fractography
Grain morphology
EDX
Tensile Test
Phase identification
Line scan of grain for concentration profiles
Homogenization Model

(a)

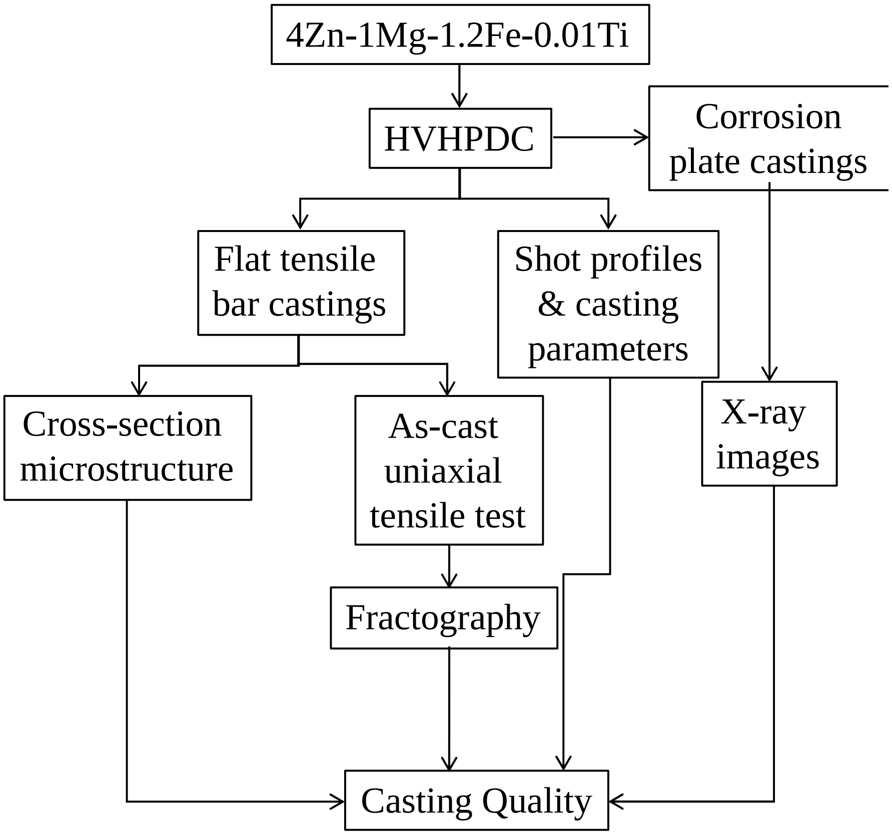

(b)

Figure 2-1: Flowcharts of the project strategy involving (a) corrosion plate castings, (b) flat tensile bar castings.

Chapter 3 LITERATURE REVIEW

The following section includes the prior knowledge needed to gain a better understanding of the various aspects of the project. The solidification behaviour of 7xxx aluminum alloys and working principles of HVHPDC process and its critical parameters were both important, since they affect the casting quality and tendencies of hot tearing. In terms of heat treatment and aging, the strengthening mechanisms of 7xxx series alloys were reviewed. The nucleation and growth of aging precipitates are also discussed. Therefore, this section includes comprehensive information on the following topics:

3.1 Aluminum Alloy Classification

Aluminum alloys can be generalized into two categories: cast and wrought alloys. The first number of both categories represents principal alloying element. Table 3-1summarizes the designation system. Cast alloys are assigned with a 3-digit decimal system, whereas wrought alloys are assigned with 4 digits [30]. Typically, the wrought alloys are primary single-phase alloys when solidified with a negligible amount of secondary / eutectic phases, while, the cast alloys are poly phase alloys with significant amounts of secondary and eutectic phases (>10 vol%) [11]. The cast alloys could be easily cast into near net shaped components, while the wrought counterparts do not lend themselves to net shaped casting due to being highly sensitive to hot tearing during solidification. Currently, the state-of-the-art alloy for structural automotive casting using HPDC, Silafont 36 (A365) falls within the 3xx.x family of cast alloys and the newly developed Al-4Zn-1Mg-1.2Fe-0.01 falls within the 7xxx family of wrought alloys with a nominal amount of Al-Fe (<3 vol%) intermetallic secondary phases evolving during solidification.

Table 3-1: Aluminum Association classification of Al alloys [12].

Cast Alloys	Primary Alloying Element	Wrought Alloys	Primary Alloying Element
1xx.x	99% Pure Al	1xxx	99% Pure Al
2xx.x	Cu	2xxx	Cu
3xx.x	Si-Cu/Si-Mg	3xxx	Mn
4xx.x	Si	4xxx	Si
5xx.x	Mg	5xxx	Mg
6xx.x	-	6xxx	Si-Mg
7xx.x	Zn	7xxx	Zn-Mg-(Cu)
8xx.x	Sn	8xxx	Sn
9xx.x	Other elements	9xxx	Other elements

3.2 <u>High Pressure Die Casting Process</u>

High pressure die casting (HPDC) is a time efficient form of near-net shape permanent mold casting. It is mostly used for metals with lower melting temperatures, such as zinc, aluminum and magnesium. In HPDC process, the castings have small wall thickness (~1.5 to 4 mm), high dimensional tolerances (<0.1mm) and desirably smooth surface quality [6,7]. The high throughput of the castings and low cost of operations make this a desirable process to cast large volumes of automotive castings in a foundry. The mechanisms of the HPDC process can be summarized in four steps [13,14]:

1. The steel die is installed onto the HPDC machine and a controlled amount of lubrication is sprayed (manually or automatically) on the surface of the die cavity to improve the ejection process. The die tool is the closed to prepare for casting.
2. The liquid metal is poured into a casting chamber and pushed into the die cavity using extremely high pressures exerted by a hydraulic press. The plunger initially starts with a low velocity (low injection speed) and increases at the end of the first phase length (high injection speed).

3. The metal is allowed to solidify under high pressure. During this time, the metal takes on the shape of the die cavity, which helps to form the casting. At the end of solidification, the injection pressure decreases.
4. When the cooling process has finished, the casting is removed. The ejector pins are used to push the casting out, and the die can be opened by the movable die half. The location of the ejector pins depends on the size of the casting.

There are two types of HPDC: cold chamber and hot chamber. Cold chamber indicates the liquid metal is poured (manually or automatically) into a cold shot sleeve and a hydraulic press pushes the metal into the die cavity. This method is typically used for metals with higher melting temperatures such as Al and Mg, since there is a chance high chance for solidification outside of the die cavity. Hot chamber HPDC uses a preheated shot sleeve and is employed for metals with lower melting temperatures such as Zn. The crucible furnace containing liquid metal is connected to the machine through an injection cylinder called the gooseneck [15,16]. During the filling stage, the plunger moves downward and pushes the metal through the nozzle and towards the die cavity. Once the casting solidifies, the plunger returns to its original position. Figure 3-1 (a) and (b) shows schematics of the cold-chamber and hot-chamber HPDC process, respectively.

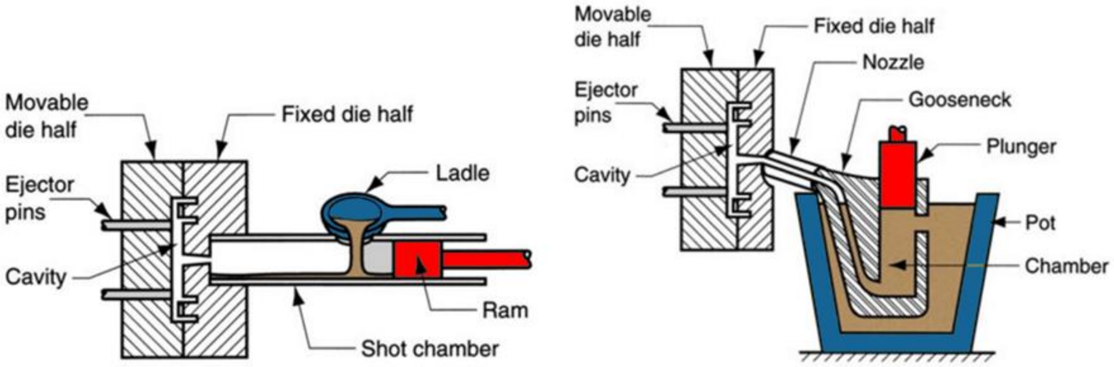

(a) (b)

Figure 3-1: Schematics of high pressure die casting system (a) cold-chamber (b) hot-chamber [17].

Typically, the conventional HPDC process is fraught with gas porosity arising from the copious amounts entrapped air and gases due to the highly turbulent filling mode of the liquid metal and the rapid solidification conditions. The air entrapment may lead to detrimental effects on mechanical properties and gas porosities near the surface of the castings may lead to blistering during solution heat treatment. To minimize the amount of entrapped gases and enable manufacturing of castings for structural applications using an integrated high vacuum system within the process: HVHPDC (High Vacuum High Pressure Die Casting). All the castings in this project were carried out using the cold chamber HVHPDC process for structural automotive components. A typical HVHPDC casting from a cold chamber process consists of six salient sections as shown in a typical casting in Figure 3-2: the biscuit, runner, gating, casting, overflow and vacuum port [18]. The biscuit is the part of metal that is solidified in the shot chamber. The runner and gating help to control the flow of the metal. Overflows gather the metal front and stores heat near thin wall sections of the casting [18]. The biscuit, runner, gating, and overflow are all considered to be die cast returns which would be scrapped or recycled, depending on the alloy used.

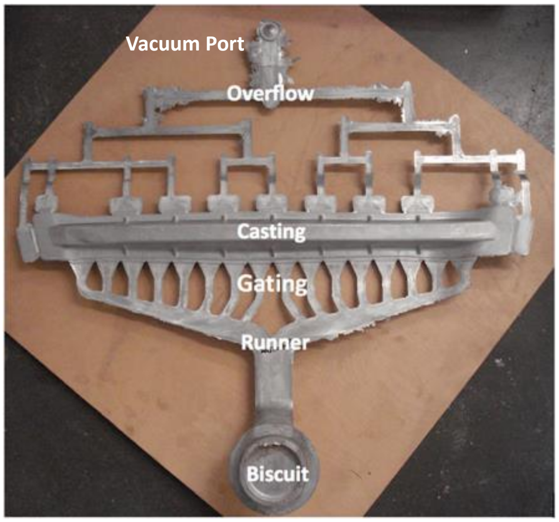

Figure 3-2: A full-shot casting from HPDC.

HPDC castings may potentially have many defects, including shrinkage porosities, blisters, scabs, hot-tearing etc. Many of these defects may be avoided with the correct control of parameters. Figure 3-3 shows a schematic of a typical shot profile in the HPDC process [18]. It can be divided into three stages: slow injection speed, fast injection speed, and pressurization. During the slow injection speed stage, a wave of turbulence is created that forces the air inside the shot sleeve to leave, effectively decreasing the amount of air entrapment. The correct speed needs to be selected, if the speed is too high, a break-away metal front wave may form, which leads to a large amount of entrapped air [18,19]. The second stage represents the fast injection speed, the speed at which the metal is pushed into the die cavity. If the transition time between stage 1 and stage 2 is too long, the metal faces risk of early solidification in the shot sleeve, leading to die clogging, incomplete filling and Externally Solidified Crystals (PSG). The third stage is the intensification pressure during solidification, which is used to further push the metal into the die cavity to feed the shrinkage of the casting. The pressure also helps to compress/collapse the entrapped air inside the castings.

Additional parameters that can affect the casting quality are: fast shot set point (or first phase length) and die cavity filling time. Tsoukalas [19] investigated the effects of all of the parameters on the porosity of aluminum die castings. It was concluded that the top three most important factors affecting the amount of porosity are: the intensification pressure, the die cavity filling time, and the fast injection speed.

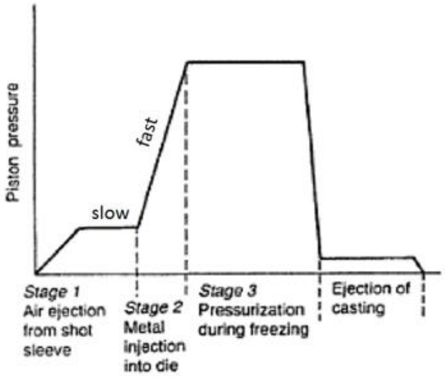

Figure 3-3: Schematic of a typical shot profile in a HPDC process [18].

The HVHPDC used an external vacuum pump system that is controlled and regulated by the feedback from HPDC process; where, sensors, strategically placed in the shot sleeve, casting cavity and overflow sections of the die tool enable rapid evacuation of a closed die (in milliseconds), immediately prior to the metal front filling the cavity [8]. This process enables a significantly rapid ejection of the entrapped air within the melt filling the cavity and results mitigating the porosity in the cast component and thereby, improving the properties and performance of the same to be used as a structural component. Vacuum-assisted HPDC was also found to improve the repeatability of the mechanical properties compared to conventional HPDC processes, particularly in ductility due to the reduction in defects [20,21,22].

3.2.1 Microstructure of HPDC Castings

The typical microstructure of a casting made by HPDC consists of three sections: the skin, defect band, and core. Figure 3-4 shows the microstructure of an A365 cast sample. The skin is located near the surface of the casting, where the liquid metal is in direct contact with the die cavity [23]. It is characterized by having finer grains due to a faster heat extraction from the die, resulting in a faster solidification rate. The thickness of the skin depends on the nature of the metal, geometry of the casting, and process parameters. A typical skin layer can be up to about 100 μm in thickness for the current Al-Si-Mg HPDC alloys [35]. For the particular casting in Figure 3-4, the skin is approximately 80μm in thickness. The defect band, or band of segregation, structure can be seen in Figure 3-5, it is a thin structure that tends to follow the contours of the casting surface. It is a region that consists of porosity and segregated eutectic phases [24,25]. Further explanation about these defect bands is provided in the following Section 3.2.2.3 of this thesis. The core region consists of larger, equiaxed grains due to slower solidification as well as the presence of pre-solidified grains (PSGs).

A365 is a cast aluminum alloy that is commonly used in HPDC processes for automotive components. Its microstructure can be seen in Figure 3-6. It is a near-eutectic Al-Si alloy consisting of two main components, the primary Al grains (in white) and the Al-Si eutectic phases (etched in gray).

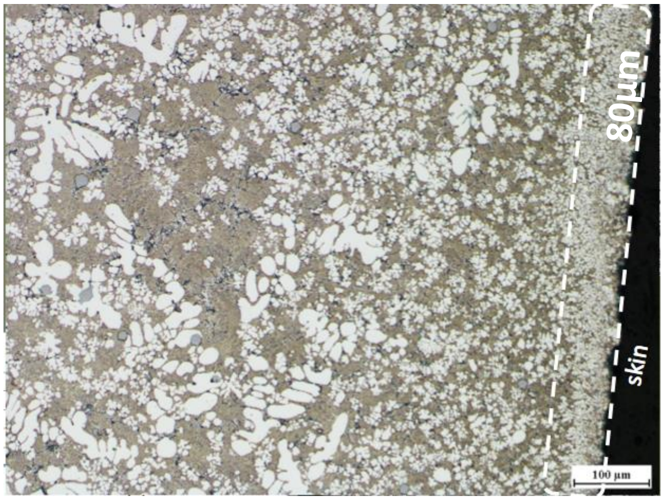

Figure 3-4: The typical microstructure of a HPDC casting, cast using A365, showing the skin.

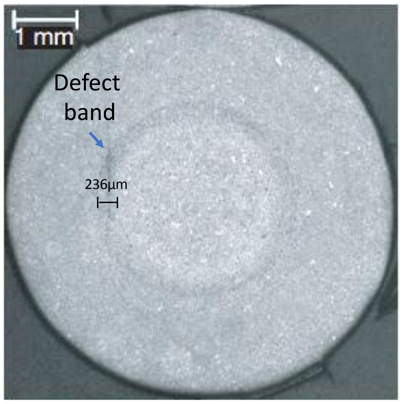

Figure 3-5: Cross section of an Al-7Si-0.3Mg alloy, cast using HPDC, showing the defect band, w=236μm, and modified [26].

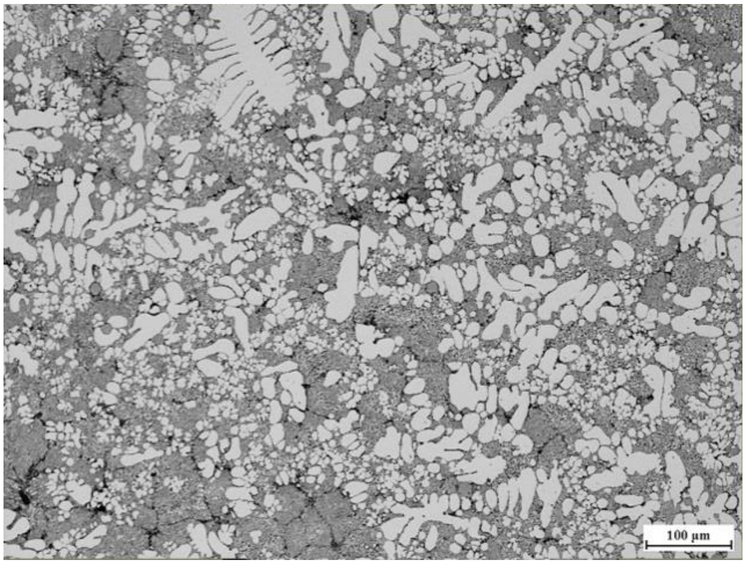

Figure 3-6: Typical microstructure of A365 cast using HPDC processes.

3.2.2 Defects of HPDC castings

There are often unique defects associated with HPDC castings due to their rapid solidification rates and abundance of critical parameters. The common types of defects include: gas porosity, shrinkage porosity, defect bands, and PSGs. Table 3-2 summarizes the morphology and causes of each type of defect.

Table 3-2: A summary of the types of defects in HPDC, their morphology, and origin.

Defect Type	Morphology	Origin
Gas porosity	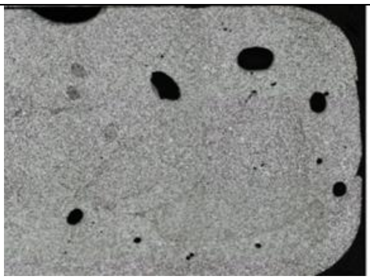	Gas entrapment during casting and H_2 rejection during solidification. Marked by smooth rounded interface with casting.
Shrinkage porosity	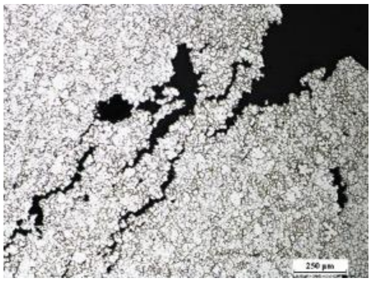	Lack of liquid metal feeding during solidification causing isolated liquid pools. As they solidify, stress increases and eventually leads to hot tearing. Marked by rugged intergranular cracks/tears.
Defect band		Built up of shearing in the mushy (two phase) zone.
PSG	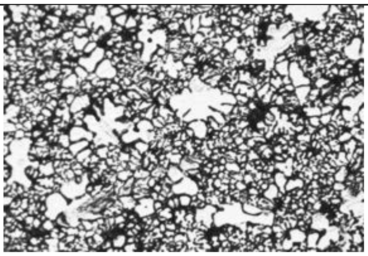	Pre-solidified crystals from the shot sleeve. They are pushed into the casting by the injection fast-shot.

3.2.2.1 Gas Porosity

Gas porosities can be identified by their globular shape. They are formed during solidification due to gas entrapment within the metal. Liquid metal can retain a larger amount of dissolved hydrogen than solid [27]. Figure 3-7 is a graph showing the maximum solubility of hydrogen in Al as a function of temperature. While the liquid melt is able to hold up to 1ml H_2/100g of Al, the solubility rapidly decreases at the melting point. The solid metal is only able to hold approximately 0.05ml H_2 per 100 g. Therefore, in the last stages of solidification, hydrogen rejection occurs at rapid rates and gas porosities are formed if the evolved hydrogen gasses are not allowed to escape the casting.

The amount and size of gas porosities can be effectively controlled by implementing the correct casting parameters. Firstly, the liquid melt should be degassed prior to casting, so as to remove the dissolved hydrogen by using a rotary degasser which bubbles ultra-high purity Ar gas (<2ppm O_2) through the melt for an extended time period [26,28]. A liquid flux that acts as a barrier between the liquid melt and the environment can also be used to prevent gas from re-entering and regassing the melt. Figure 3-8 shows a comparison of the difference in the amount of gas porosity between the cross-sections of two AlSr15 samples cast using sand moulds: one without degassing and one with 10 minutes of degassing with high purity Ar gas [29]. The slow and fast injection speeds should also be optimized to maximize ejection of the air from the die cavity.

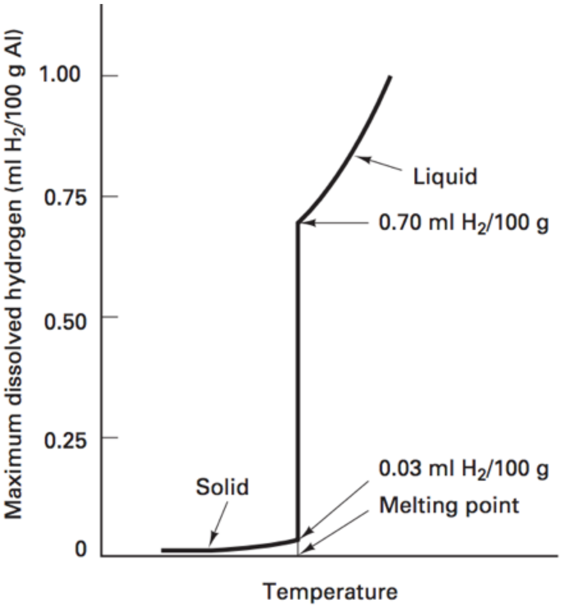

Figure 3-7: The dissolved hydrogen in pure Al, as a function of temperature [28]

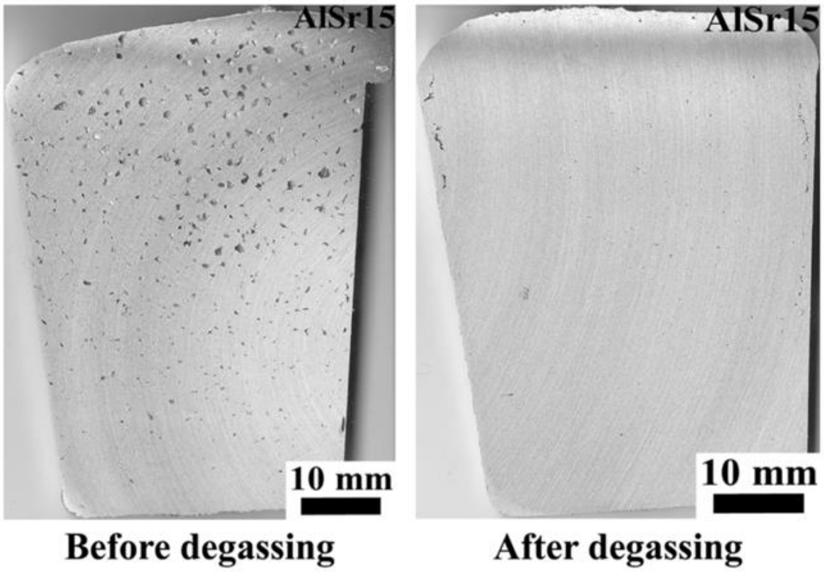

Figure 3-8: Comparison between cross-section of AlSr15 samples cast using sand moulds, before degassing versus after 10 minutes of degassing with high purity Ar [29].

3.2.2.2 Shrinkage Porosities

Shrinkage porosities are characterized by their rugged, crack-like surface morphology. Figure 3-9 shows shrinkage porosities within a cast alloy, highlighted by the blue arrows. They are well studied and concluded to have a significantly detrimental effect on mechanical properties due to their ability of inducing crack initiation and rapid propagation by connecting with neighbouring cracks [30,31,32]. Shrinkage porosities form during the last stages of solidification, when there is a lack of liquid feeding the dendritic network. Eventually, the flow of liquid stops and there is a pool of liquid amongst a shell of solid, that shrinks. Further solidification of the last liquid causes shrinkage and increases stress on the network, eventually causing hot tearing (elaborated in Section 3.3.1).

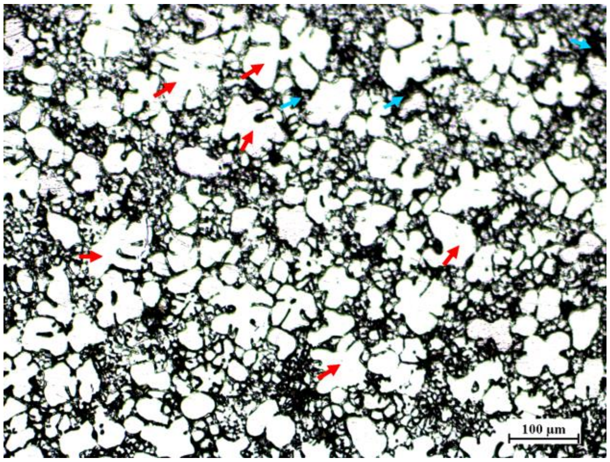

Figure 3-9: A typical microstructure image of an Al-4Zn-1Mg-1.2Fe-0.01Ti alloy casting. Some of the PSGs are highlighted with the red arrows, and the shrinkage porosities are highlighted by the blue arrows.

3.2.2.3 Defect Bands

The defect band is a contour band in the microstructure that occurs inside a casting and typically, takes the shape of the casting surface; it is generally made up of a combination of solute segregation, gas porosities, and shrinkage porosities. Due to the nature of the defect, it cannot be mitigated with heat treatment [33]. Dahle and St. John [34] proposed a theory on the rheological behaviour of the mushy zone and its effects on the formation of defect bands. They proposed that during HPDC, a fraction of the liquid melt entering the die cavity is pre-solidified. Internal stresses will be generated as the metal flows through the die. The highest concentration of stress will be along the walls, where the solidification rate is the highest. The shear stresses will push the dendrites to the centre of the casting, increasing the solid fraction at these locations. Figure 3-10 (a) shows a schematic of the solid fraction profile. Figure 3-10 (b) shows the yield stress profile for the same casting. The yield stress is highest along the walls due to the rapid solidification mode and the lowest at the locations of lowest solid fraction. These areas then become the most susceptible to shearing during solidification, thus forming defect bands. Figure 3-10 (c) shows the schematic of the final microstructure based on the theory.

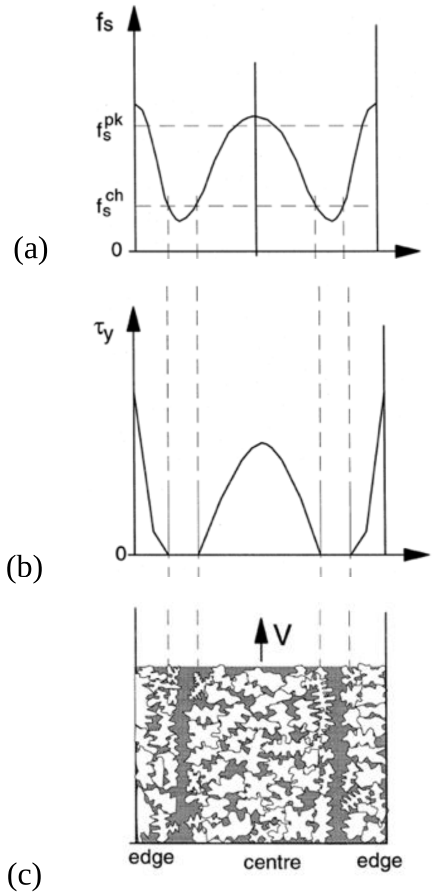

Figure 3-10: Schematics showing the solidification process that leads to the formation of defect bands. (a) The fraction solid profile as a result of flow when the liquid melt is being poured into the casting, where, f_s^{pk} represents a transition point and f_s^{ch} represents the dendrite coherency point, (b) the yield stress profile within the casting cross-section and (c) final solidified microstructure showing the defect band [34].

3.2.2.4 Pre-solidified Grains (PSG)

PSGs are grains that solidified outside of the die cavity, normally in the shot sleeve. They are characterized by being significantly larger than the rest of the microstructure [35]. Figure 3-9 shows a microstructure image of a casting containing a large amount of PSGs. In HPDC, crystals nucleate and solidify as soon as the liquid metal hits the shot sleeve due to the high heat transfer rate. These PSGs are then pushed into the die cavity along with the liquid metal, where they can either continue to grow due to the fast cooling rates, fragment into smaller grains, or remelted [35].

Schematics of the microstructural evolution of PSGs in various areas of a casting can be seen in Figure 3-11.

PSGs can also be created by improper management of HPDC parameters. Wu et al conducted experiments by varying parameters such as the slow injection speed, fast injection speed, and holding time [36]. They concluded that a large amount of PSGs are produced with a lower slow injection speed and a longer holding time due to the loss of superheat from the liquid melt. Additionally, a higher fast injection speed led to significantly more fragmentation and produced an increased amount of PSGs with a spherical morphology due to a higher impingement.

Researchers also found that the amount of PSGs had a significant influence on the properties of the castings. The research conducted by Li et al [35] suggests that the existence of PSGs could lead to the formation of large, interconnected shrinkage porosities during solidification. They can also be seen in Figure 3-9, highlighted by the blue arrows. These shrinkage porosities are mostly formed in the middle of the casting with a lower cooling rate. This allows the PSGs to grow at a faster pace, causing a greater amount of shrinkage porosities at the grain impingement locations. During uniaxial tensile tests, these porosities are thought to be the primary source for crack initiation. The crack would propagate in an intergranular-fracture by connecting to the neighbouring porosities at the grain boundaries of the PSGs.

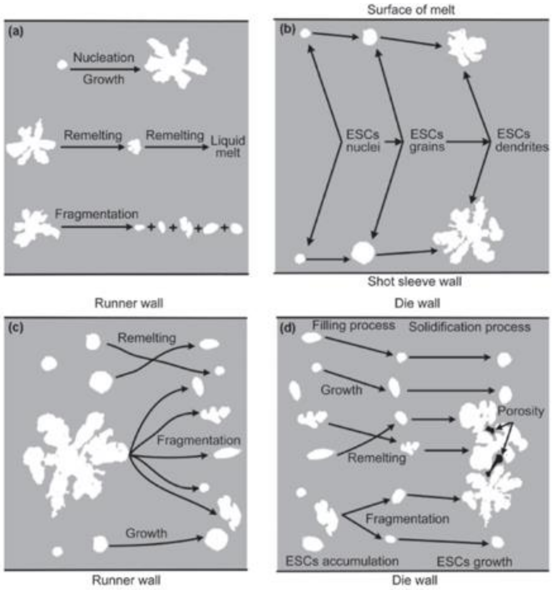

Figure 3-11: Schematics showing the microstructure evolution of PSGs; (a) the microstructure of the PSGs during nucleation, growth, remelting and fragmentation, (b) evolution in the shot sleeve, (c) in the runner wall and (d) in the die cavity [36].

3.3 Solidification of the Al-Zn-Mg-(Fe)-(Ti) system

This section will discuss some of the general solidification characteristics of the Al-Zn-Mg alloy. In a typical Al-Zn-Mg alloy system, the primary Al phase solidifies and evolves as a complex dendritic network during solidification. Zn and Mg based intermetallic phases are formed during solidification, but they do not contribute to the solidification behaviour of the primary Al phase. Mazahery [37] and Ghiaasiaan [38] have both conducted experiments on the solidification Al-Zn-Mg system in permanent mould and controlled directional solidification (CDS) casting methods, respectively. Since the Al-Zn-Mg-Fe-Ti alloy is newly developed, this thesis serves as the first contribution to the literature for this alloy.

Mazahery studied the effect of Ti addition on the Al-3Zn-1Mg alloy using permanent mould casting. 0.05wt% of Ti was added to the alloy and the grain size comparison can be seen in Figure 3-12. It is evident that Ti is an excellent grain refiner for this system, the grains without Ti addition (Figure 3-12(a)) are approximately 400μm in size, whereas the grains with Ti addition (Figure 3-12(b)) are approximately 80μm. Furthermore, refined grain structures improve the hot tearing susceptibility of the alloy by creating an improved connectivity of the liquid phase during the final stages of solidification [39].

Ghiaasiaan presented the microstructure images of the Al-3.5Zn-0.8Mg alloy, cast with CDS technology, followed by an annealing treatment, isothermal holding at 413 °C for 2h and cooling to room temperature at 20 °C/h. The microstructure, as presented in Figure 3-13, revealed mainly primary Al grains with very little Mg-Zn eutectics at the grain boundaries. The morphology of the grains is equiaxed, similar to the grains found by Mazahery [37]. The phases within the primary Al grains are η-$MgZn_2$ precipitates.

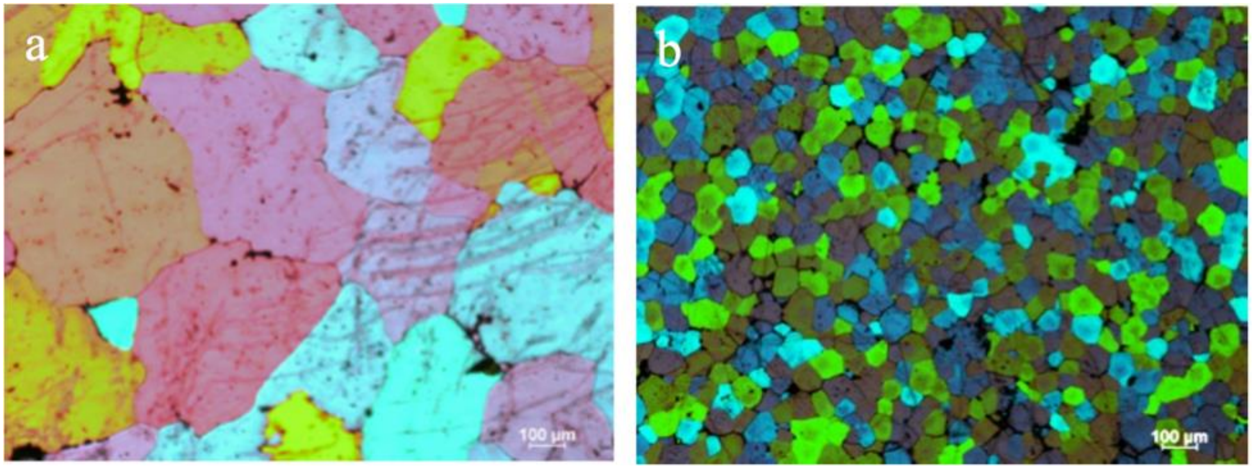

Figure 3-12: The effect of adding 0.05wt% of Ti to the Al-3Zn-1Mg alloy to the grain size and morphology, cast using a permanent mold, (a) without Ti addition, (b) with Ti addition [37].

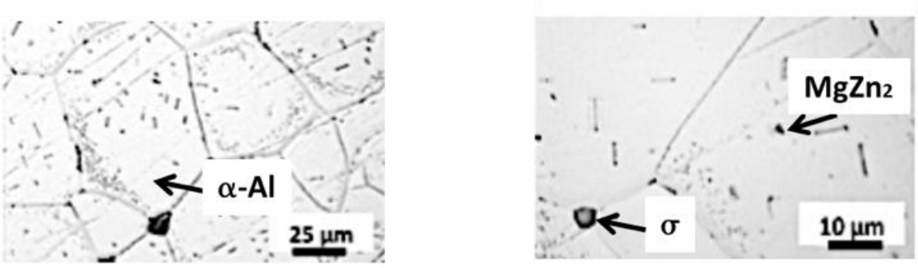

(a) (b)

Figure 3-13: Microstructure images showing the structure and grain morphology of the Al-3.5Zn-0.8Mg alloy cast using CDS processes and annealed with labelled phases (a) lower magnification (b) higher magnification [38].

3.3.1 Hot Tearing

Hot tearing, as seen in Figure 3-14, is a common casting defect. It is defined as an irreparable crack that forms in a semisolid casting as a result of excess strain that is created during solidification [5,40]. They form as a combination of mechanical and microstructural factors [41]. Figure 3-15 is a schematic that shows the formation of hot tearing in terms of the fraction of solid. In the initial stages of nucleation, there is free flow of liquid in between the solid crystals. The dendritic coherency point (DCP) is established when there is a coherent dendritic network [42]. As the crystals grow further, the mushy zone is reached. Liquid feeds the growth of the dendrites and compensates for the volumetric shrinkage that occurs during solidification. When there is a lack of liquid, or the feeding channels are blocked off, the alloy is susceptible to forming shrinkage porosities. Hot tearing occurs in the late stages (fraction of solid, $f_s > 0.80$) of solidification. On a microscopic level, solidification shrinkage creates internal strains and stresses on the solid network, increasing the tendency of hot tearing [43,44]. There are two well-known theories that describe the basics of hot tearing formation: the strain theory, and the shrinkage-brittleness theory.

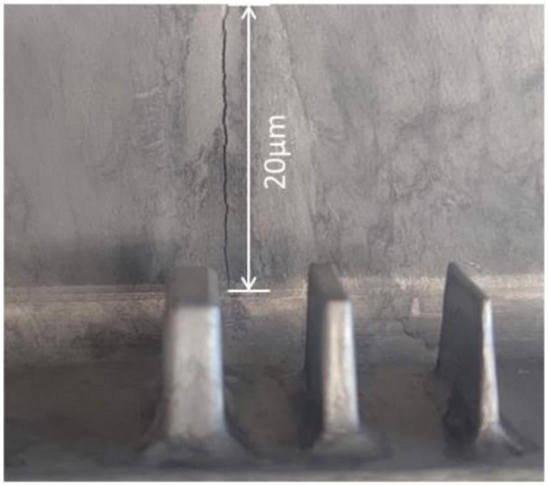

Figure 3-14: Hot tearing cracks that occur in HPDC castings.

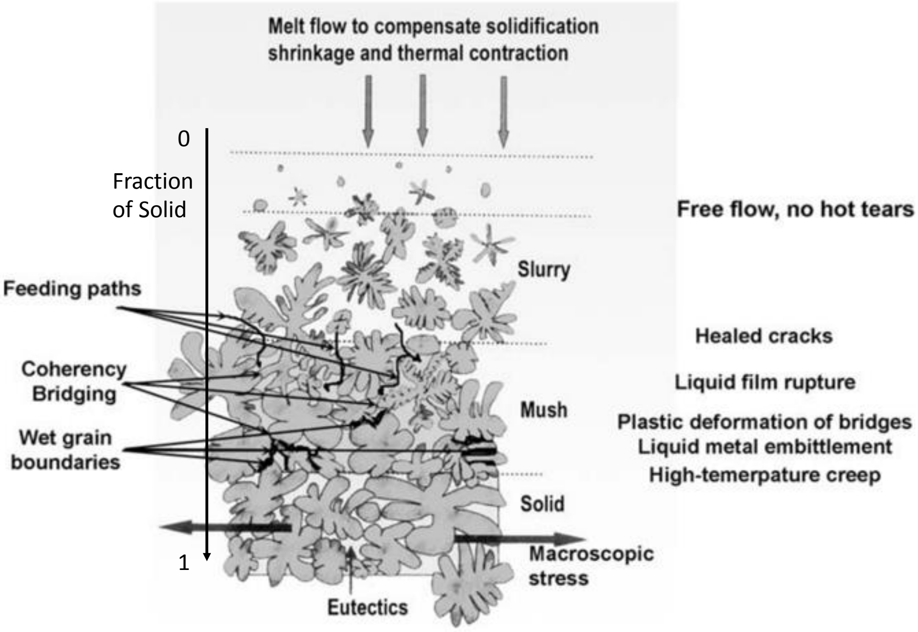

Figure 3-15: Schematic showing the amount of grain nucleation and growth for a range of solid fraction [40].

The strain theory was first proposed by Pellini [45], it suggests that hot tearing only occurs when there is a liquid film that exists in the semisolid metal between the grain boundaries of the dendrites. As the metal solidifies, localized strains are generated and transmitted along the solidified grains of the casting and propagated through the liquid film [46]. The rate of extension is the greatest factor in determining the existence and severity of the hot tears. Some of the factors that contribute to high rates of extension include: contraction in long regions, contraction in fast cooling regions, and extension in narrow hot-spot regions

The shrinkage-brittleness theory was first proposed by Pumphreys et al [47]. They proposed that hot tearing occurs in the mushy zone, a region that consists of both liquid and solid phases at the coherency temperature. As temperature drops, a continuous network of dendritic solid structures is formed inside the mushy zone. As the dendritic network continues to grow, the dendritic arms impede upon each other, cutting off the flow path of the liquid and preventing feeding. During the last stages of solidification, these areas experience large strains due to shrinkage. When a critical strain is reached, a crack propagates through the metal [46]. This theory was augmented by Hunt and Durrans [48] that hot tearing is a two-step phenomenon that involves nucleation and propagation. They suggested that the hot spots for hot tearing nucleation are inhomogeneities in the material such as inclusions and grain boundaries.

A few key points about hot tearing were noticed by many researchers through experimentation:

- Alloys that are prone to hot tearing tend to have little eutectic content and wide temperature ranges during solidification.
- Alloys with fine grain structures have lower hot tearing susceptibility. This relates to the Hunt and Durrans [48] theory that suggests grain boundaries as a possible initiation spot.
- Controlled casting conditions with minimal thermal and stress gradients are important for decreasing hot tearing tendency [40].

3.3.2 Iron Additions

Traditional Al-Zn-Mg alloys typically have poor castability due to the dendritic nature of the primary aluminum grains [5]. Studies were conducted on the topic of minimizing hot tearing and shrinkage defects, but they are not generally used for HPDC purposes. The iron content in castable alloys are generally kept to a minimum, as they may produce harmful plate-like secondary phases such as θ-$Al_{13}Fe_4$ and β-Al_5FeSi. Puncreobutr et. al [49] concluded through in-situ solidification that β-intermetallics induces porosity formation and growth. β-intermetallics block the interdendritic channels, blocking liquid feeding and isolates pockets of liquid which contracts without compensation at the final stages of solidification, leading to the formation of shrinkage porosity. The surface of the β-intermetallics and the evolving gas both have low interfacial energies, thus, increasing nucleation of gas porosities. These intermetallic phases also decrease the hydrogen supersaturation, further increasing the amount of gas porosities. Additionally, the plate-like morphology of these phases is detrimental to mechanical properties by decreasing the isotropy of the material, which can lead to brittle fractures. Notably, the formation of β-Al_5FeSi intermetallic phases are alleviated at low levels of Si impurity in the melt (<0.05 wt%).

For conventional casting alloys, iron contamination plays a detrimental part in the production of a successful casting. However, in the Al-Zn-Mg-Fe system, specific non-equilibrium meta-stable Al-Fe intermetallic phases such as the Al_6Fe and Al_mFe (m=4 to 4.4), were observed to decrease the hot tearing susceptibility of the alloy. Table 3-3 shows the types of Al-Fe intermetallic phases that may form during solidification as determined by Zhang et.al. [50,51]. Further details about this theory will be provided in Section 4.1.2.

Table 3-3: The composition and morphology of Al-Fe intermetallic phases that form during solidification [50,51].

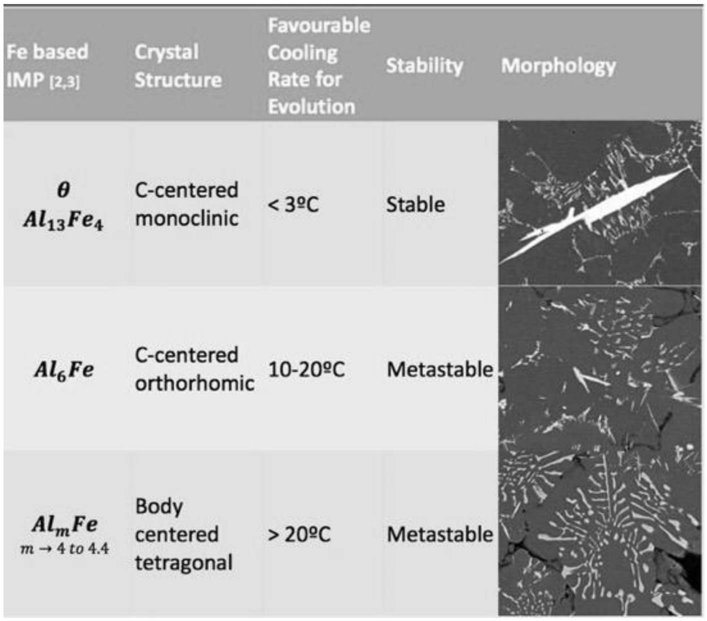

Fe based IMP [2,3]	Crystal Structure	Favourable Cooling Rate for Evolution	Stability	Morphology
θ $Al_{13}Fe_4$	C-centered monoclinic	< 3ºC	Stable	
Al_6Fe	C-centered orthorhomic	10-20ºC	Metastable	
Al_mFe $m \rightarrow 4$ to 4.4	Body centered tetragonal	> 20ºC	Metastable	

3.4 Heat Treatments of the Al-Zn-Mg system

A typical heat treatment process of a 7xxx series aluminum alloy consists of three stages: solution heat treatment, quenching, and aging. The solution heat treatment involves heating the alloy in high temperatures. Its goal is to homogenize the alloy, allowing for solute redistribution to occur. Some intermetallic phases experience a change in morphology or are completely dissolved. This stage also relieves the alloy of any built-up internal stresses from casting. After homogenization is reached, the alloy is quickly brought back to ambient temperature in the quenching stage. A variety of quenching mediums can be used, and the cooling rate is crucial in determining the amount of solute segregation that happens. After quenching, the alloy can be heated again in a low temperature heat treatment (artificial aging) or left to incubate at ambient temperature (natural aging). 7xxx series alloys are age-hardenable, which means their strength increases during the aging treatment due to the nucleation and growth of aging precipitates in the homogenized primary Al grains. Artificial aging allows for increased kinetics and more precipitation phases to evolve in the ageing process compared to natural aging.

Table 3-4 summarizes some of the common heat treatment tempers for aluminum alloys. Detailed explanations of these three stages are provided in the sections below.

Table 3-4: Aluminum alloy heat treatment tempers [52].

Temper	Explanation
F	As-cast
T4	Solution heat treatment followed by aging in room temperature (natural aging) to a stable condition
T5	Cold working at elevated temperatures, followed by aging at elevated temperatures (artificial aging)
T6	Solution heat treatment followed by artificial aging to maximize the strength
T7	Solution heat treatment followed by an overaging treatment to increase toughness and corrosion resistance

3.4.1 Solution Heat Treatment

Solution heat treatment occurs at high temperatures with a long soaking time. Its main purpose is to homogenize the concentration of soluble alloying elements by creating a solid solution. The heat treatment temperature is determined by the composition of the alloy; however, it is typically 10°C lower than the initial melting temperature in order to prevent incipient melting [52]. Incipient melting refers to the localized melting of certain eutectic/secondary phases within an alloy. It leads to a degradation of mechanical properties such as tensile strength and ductility. The soaking time of the alloy depends on its composition (some alloying elements have limited diffusion in aluminum), the size/morpohology of primary Al grains and the thickness of the castings. Thick castings require longer soaking times to homogenize. High temperature oxidation may occur during solution heat treatment at long soaking times. This is due to the increased diffusion and coagulation of entrapped hydrogen, which can occur in the form of surface blisters. It can be mitigated with a decreased solution temperature and soaking time.

3.4.2 Quenching

After solution heat treatment, the casting is rapidly cooled to ambient temperature in order to retain the supersaturated solid solutions (SSSS). The rate of quenching determines the mechanical properties. Fast quench rates result in higher strengths and residual stresses, whereas lower quench rates are used to relieve residual stresses. Typically, castings with thick dimensions and require high strengths need to be quenched rapidly, which are achieved with immersion in cold and agitated water. Slower cooling rates can be achieved with hot water, oil, forced air, or still air quench, in that order. They are generally used to reduce residual stresses and distortions. Residual stresses increase for castings with large thicknesses due to different thermal expansions between the warm centre and the already-cool outer shell [52].

Fink and Willey made the first systematic attempt on correlating quenching rate and properties for 0.064" aluminum sheets in 1948 [53]. They concluded that in order for the metal to retain its maximum strength and corrosion resistance, quench rates needed to exceed 450°C/sec [53,54]. Further studies were conducted by Evancho and Staley (1974), who proposed the "Quench Factor" (τ), a method of predicting mechanical properties based on the integration of the area between the

Time-Temperature-Property (TTP) curve and quench path. The quench factor can be calculated using Equation 3-1:

Equation 3-1 $$\boldsymbol{\zeta = 1 - \exp(k\tau)}$$

where ζ is the fraction of phases transformed and k is a constant that relates to the transformation fraction of a TTP curve. Other mechanical properties, such as corrosion behaviour and yield strength, can also be predicted with quenching.

3.4.3 Aging

Subsequent hardening of the castings can be achieved through natural aging or artificial aging. The purpose of aging is to increase the strength and hardness of a casting through the evolution of aging precipitates in the primary Al grains. Natural aging occurs at room temperature immediately after quenching, whereas artificial aging occurs at low heat treatment temperatures (typically 70-200°C). The rate of hardening for both forms of aging depends on the alloy composition and quench rate, specifically the amount of SSSS and Vacancy Rich Clusters (VRC) retained in the primary Al grains. Aging effects are also temperature dependent; therefore, the rate of hardening produced by artificial aging is always higher than natural aging. Similarly, aging can be delayed or suppressed by subjecting the casting to very low temperatures (typically -18°C or lower) [52]. Figure 3-16 shows the rate of change of mechanical properties for alloys 2014 and 2024 at different aging temperatures.

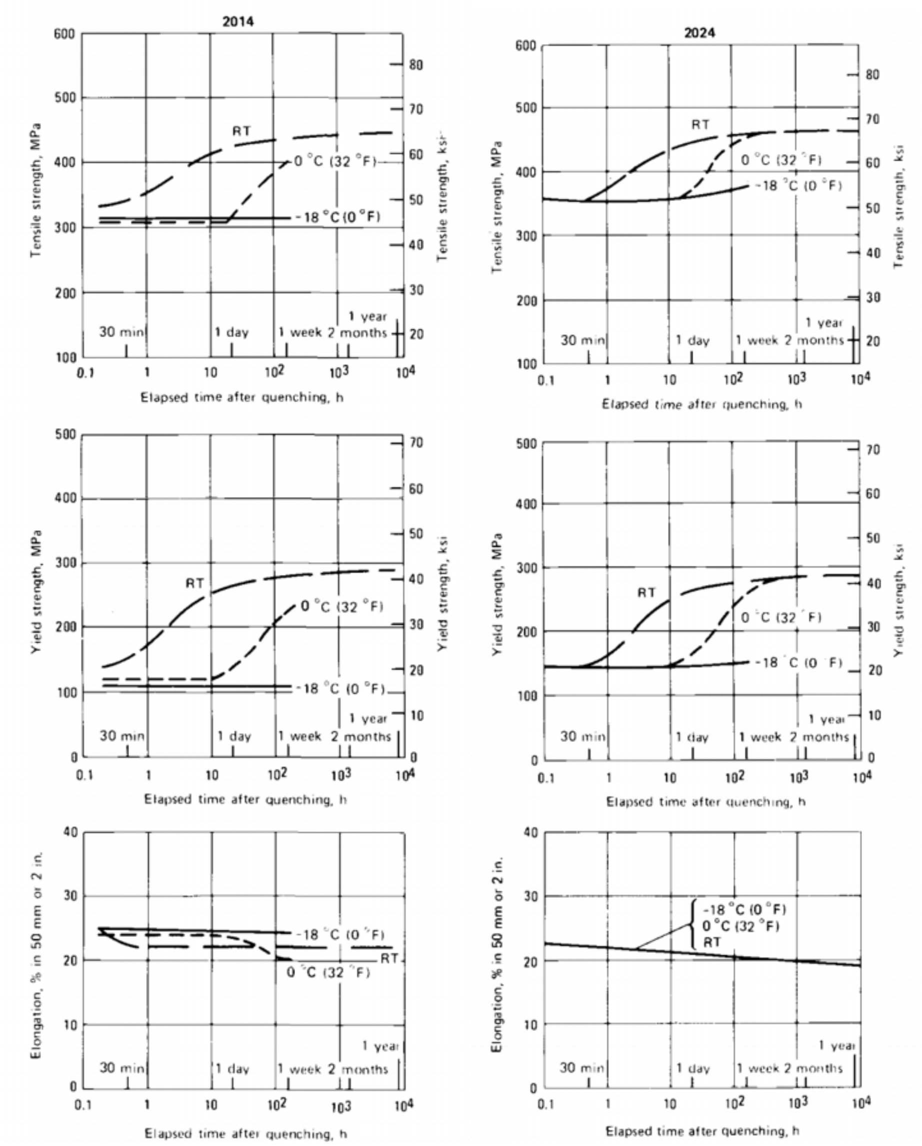

(a) (b)

Figure 3-16: Comparison of the rate of change of mechanical properties (tensile strength, yield strength, and elongation) vs. aging at room temperature, 0°C and -18°C of (a) alloy 2014 and (b) alloy 2024 [52].

3.4.3.1 Aging Mechanisms

Aging can be split into three sections depending on incubation time: underage, peak age, and overage. Figure 3-17 shows a schematic of the overall aging process in terms of strength and incubation time. An increase in strength can be seen in the underaged and peak age conditions. In the overaged condition, strength decreases to compensate for an increase in corrosion resistance. The mechanisms that are involved for a 7xxx series alloy can be summarized as follows [55]:

$$SSSS \rightarrow\ GP\ zones\ (GP - I\ \&\ GP - II) \rightarrow \eta' \rightarrow\ \eta - MgZn_2$$

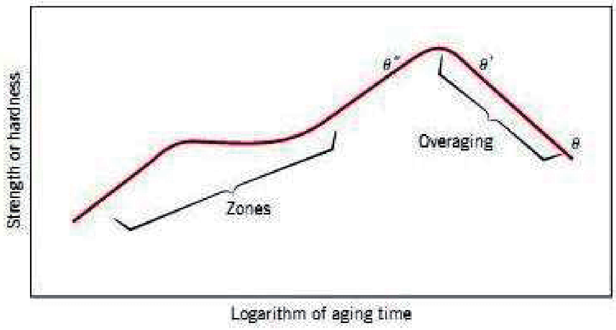

Figure 3-17: Schematic of the overall aging process showing strength vs. incubation time [56].

In the underaged condition, the SSSS retained from solution heat treatment forms Guinier-Preston (GP) zones in the aging process. GP-zones are early stage aging precipitates and are responsible for increasing the strength of the alloy during aging. The GP-zones in 7xxx series, copper-free alloys are Zn and Mg based. GP-zones were first discovered by the researchers Guinier [57] and Preston [58] in 1943. In the Al-Zn-Mg alloys, there are two types of GP-zones with different crystalline structures and formation temperatures: GP-I and GP-II. GP-I form between room temperature, up to 140°C. They are fully coherent with the aluminum matrix with Zn as the internal structure and Mg or Al on the matrix lattice [59]. They can be identified as having a spherical morphology, typically 3nm in size [60]. GP-II were found to form in aging temperatures above 70°C, only after extended solution treatment times at 450°C or higher, signifying their strong dependence on formation of SSSS [61,56]. They are approximately 3-6nm wide and have a plate-like or parallelepiped morphology [60]. Their structure is believed to have alternating layers of Zn and Mg. Figure 3-18 shows bright field TEM images of GP-I and GP-II zones, showing their respective morphologies.

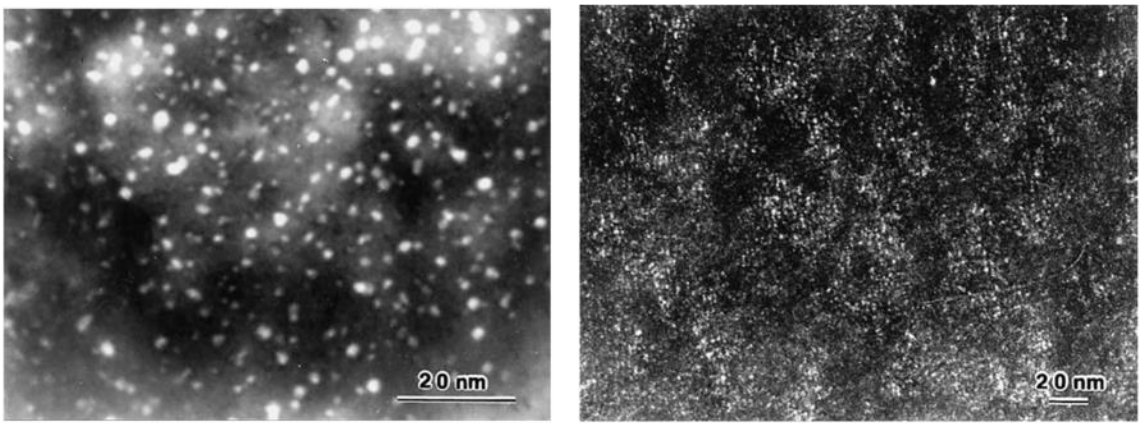

(a) (b)

Figure 3-18: TEM images showing the morphology of GP-zones (a) bright field image of GP-I zones (b) dark field image of GP-II zones [60]

3.5 Strengthening Mechanisms in Al 7xxx alloys

Increasing strength is important since it increase the resistance to plastic deformation. The strength of a metal depends on how easily dislocations can propagate through it. Strengthening mechanisms introduce obstacles to dislocation movement. Equation 3-2 presents a broad summary of all of the types of strengthening involved: intrinsic strength, grain boundary strengthening, solid solution strengthening, and precipitation strengthening. The intrinsic strength represents the strength of the metal matrix. In the as-cast state, particularly employing HPDC, the grain structure will be very fine; therefore, grain boundary strengthening will be a large contributing factor to the alloy's strength.

7xxx series alloys are heat treatable and age-hardenable. The most widely studied form of strengthening is through solution heat treatment, wherein, the alloys are strengthened through solid solution strengthening. The zinc and magnesium additions in 7xxx series alloys allow them to naturally age, thus increasing strength by precipitation strengthening.

Equation 3-2: $$\boldsymbol{YS = \sigma_o + \sigma_{gs} + \sigma_{ss} + \sigma_{ppt}}$$

3.5.1 Intrinsic Strength (σ_0)

The intrinsic strength is commonly known as the friction stress, it is determined by the strength of the primary aluminum matrix. It is only dependent on the strength of the atomic bonding without the effects of dislocations, cracks, or crystallographic imperfections. Studies from Ghiaasiaan concluded for the Al-Zn-Mg-Ti (no Fe addition), the intrinsic strength of the Al matrix is 14.5 MPa [38].

3.5.2 Grain Boundary Strengthening (σ_{gs})

Grain boundary strengthening relates the dependence of strength and the grain size of the metal. Studies have found that grain boundaries are effective in impeding the movement of dislocations by acting as pinning sites. Additionally, there is a large orientation mismatch between a grain and its grain boundary which makes shear transfer impossible, resulting in the formation of dislocation pile-ups and local stress concentrations [62,63]. Dislocation pile-ups increases the back-up stress, and in turn, increases the critical resolved shear stress [62,64]. Therefore, metals with smaller grains have a larger area of grain boundaries, and in turn, higher strength. This mechanism can be modelled by the Hall-Petch relationship, given by [65,66] Equation 3-3:

Equation 3-3

$$\boldsymbol{\sigma = \sigma_0 + KD^{-1/2}}$$

where σ is the strength, σ_0 is friction stress, including influences from solutes and particles, K is a constant, and D is the grain size. Multiple studies have proven this theory; however, it is not the only mechanism responsible for increasing the strength of the metal.

During deformation, the individual grains of a polycrystalline material will each experience a different strain due to their different crystalline orientations. An accumulation of geometrically necessary dislocations is needed to maintain boundary continuity [63], which also contributes to the strengthening. There are also other factors that need to be considered as well, such as the initial dislocation density and the presence of other obstacles that may impede dislocation motion. The effect of grain boundary strengthening may be affected due to the possibility of grain growth and coarsening particularly after solution heat treatment. In the Al-Zn-Mg-Fe alloys, this is not the case, since titanium was added as a grain refiner. However, Ghiaasiaan [38] determined that, in the Al-Zn-Mg alloys, the effect of grain boundary on the yield strength of the alloys is approximately 3% of the overall yield strength.

3.5.3 Solid Solution Strengthening (σ_{ss})

During the solution heat treatment of 7xxx series alloys, solute (in particular, zinc and magnesium) redistribution occurs as the amount of alloying elements dissolved in the Al matrix increases. They will eventually form a solid solution with the aluminum crystals and distort the lattice shape causing local stress fields and an increase in critical resolved shear stress. As dislocations propagate through the alloy, their motion would be impeded by these stress fields. This would slow down the rate of plastic deformation, leading to an increase in yield strength [67].

There are two types of solid solutions: interstitial and substitutional. Figure 3-19 outlines the difference between the two. Interstitial solid solutions occur for small-sized alloying elements, typically O, C, Li etc. They position themselves along the vacant spaces in between the primary lattice atoms and marginally deform the metallic bonds. Substitutional solid solutions occur when the alloying element atoms are of similar size to the primary atom and can replace their lattice positions [68]. Interstitial solid solutions are more effective at strengthening because they produce non-spherical distortion areas with higher stresses, whereas substitutional creates spherical areas [29].

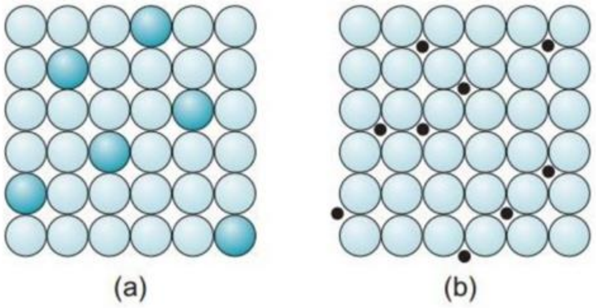

Figure 3-19: The difference between (a) substitutional and (b) interstitial solid solution [26].

Generally speaking, increasing the amount of total alloying elements increases the strength, however, not all elements can be combined into solid solutions. Whether a metal and its alloying elements will successfully make a solid solution depends on several factors. Hume-Rothery [69,70,71] devised a set of rules to determine whether elements will make a successful solid solution; the rules are as follows:

1. Size factor: For substitutional solid solutions, the size of the solvent atom and the solute atom should not differ by more than 15%. For interstitial atoms, the radius of the solute atom should be less than 59% of the solvent atom.
2. Electronegativity: The electronegativity of the host atom and solute atom should be similar. If there is a large difference between the two, they may form chemical compounds.
3. Valency: The solvent atoms should have a higher valency than the solute atoms.

Solid solution strengthening has the greatest effect immediately after quenching stage. The quench rate is also a key factor to consider as well, as it determines the size of the precipitation free zone (PFZ) in each grain. A trade-off exists between solid solution and precipitate strengthening as the supersaturated solid solution (SSSS) forms vacancy rich clusters (VRC) which lead to the Guinier-Preston (GP) zones (Mg, Zn) during the aging process, which can occur as early as immediately after quenching. As the alloy continues to age, the effect of solid solution strengthening will dramatically decrease until a balance is reached between the two mechanisms. For the Al-Zn-Mg system, the contribution from solid solution strengthening is approximately 30%, on the total yield strength of the alloy [38].

3.5.3.1 Precipitation Free Zones (PFZ)

Precipitation free zones (PFZ's) are the areas in between the primary grains, at the boundaries that are devoid of any precipitates. Figure 3-20shows an example of a PFZ, captured using transmission electron microscopy (TEM). The width of the PFZ is strongly dependent on the solution treatment temperature, quenching rate after solution treatment [72], as shown by the schematic in Figure 3-21; wherein, it can be concluded that PFZ width increases with decreasing solution temperature, lower quench rates and increasing aging temperature, alike.

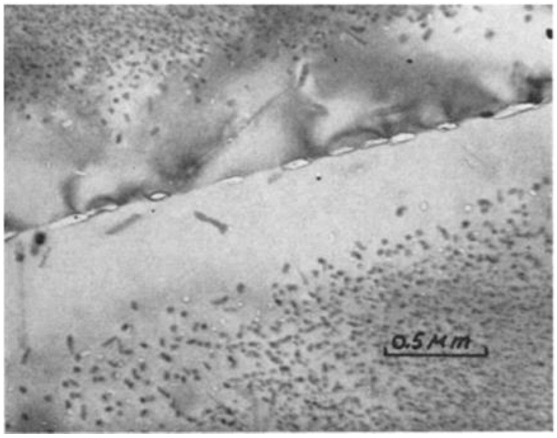

Figure 3-20: PFZs seen at grain boundaries [89]

Vacancy-depleted PFZ's are formed even during homogenized solute concentration in the matrix without solute segregation because the grain boundaries act as a sink to annihilate vacancies; zone size increases with decreasing quench rates because grain boundaries act as vacancy sinks during quenching. From research by Embury [60], a vacancy concentration profile can be modelled by Equation 3-2:

Equation 3-2

$$C^S = Aexp\left(\frac{-E_F}{kT_S}\right)$$

where A is a constant of entropy, E_f is the energy of formation, k is the Boltzmann constant, and T_s is the solution heat treatment temperature. Figure 3-21 shows the curve drawn from the equation. The critical vacancy concentration, C_{crit}^T, is defined as the minimum concentration of vacancies needed to for the nucleation of precipitates. According to Equation 3-2, there will be no precipitation in the matrix until the C_{crit}^T is reached; therefore, PFZ is the region that is low on retained vacancies during quenching after solution treatment.

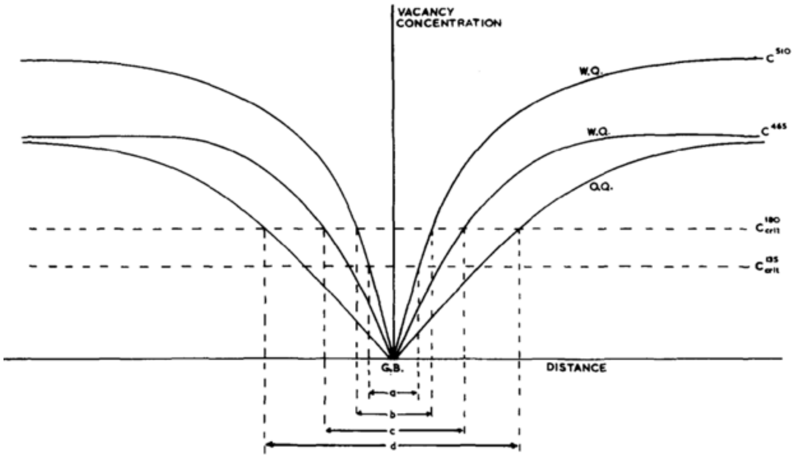

Figure 3-21: A comparison of the Al-5.9Zn-2.9Mg (%wt) alloy (a) Solution temperature: 510°C, water quench, aging temperature at 135°C (b) solution temperature: 510°C, water quench, aging temperature at 180°C, (c) solution temperature: 465°C, water quench, aging at 180°C, and (d) solution temperature 465°C, oil quench, aging at 180°C. [54]

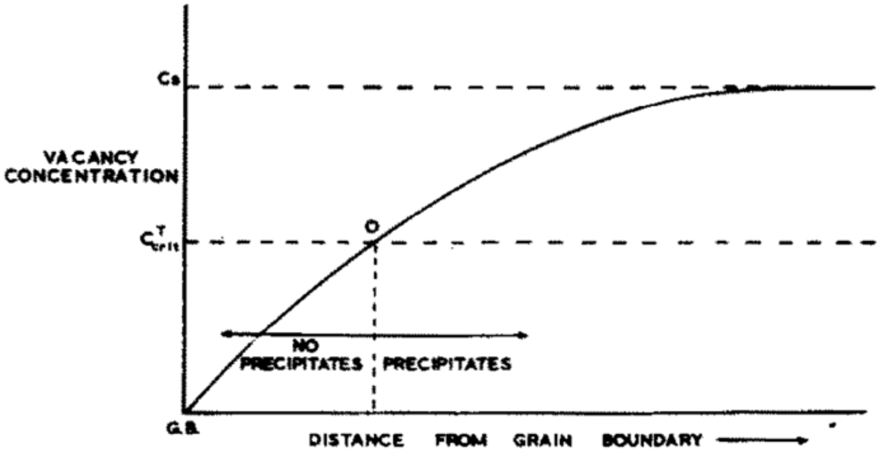

Figure 3-22: The vacancy concentration profile based on Equation 3-2 [68]

3.5.4 Precipitation Strengthening (σ_{ppt})

Precipitation strengthening is the formation of fine-scale precipitates that nucleate throughout the grain and act as pinning sites to impede dislocation movement due to the coherent/semi-coherent interface between the precipitates and matrix. Particle size has a large influence on the type of interaction and amount of strengthening. Figure 3-23 is a schematic showing the variation of strength with particle size. The interactions between dislocations precipitates can be classified as hard-contact and soft-contact [73]. Soft-contact interactions generally occur with small-sized precipitates that are coherent or semi-coherent with the matrix. Dislocation pass these precipitates by shearing them. Coherent/semi-coherent interfaces between the precipitate and matrix coupled with smaller size of precipitates promote a soft contact with mobile dislocations, while, larger precipitates and less coherent/incoherent interfaces lead to a hard contact with mobile dislocations. In hard-contact interactions, the dislocations would need to deform and bow around these precipitates to bypass them [74]. Figure 3-24 shows dislocations moving through precipitates through shearing Figure 3-24(a) and bypassing (b). The critical bending angle (φ) represents the bend of the dislocation as it passes through it. When $\varphi \rightarrow 0$, dislocations move by shearing; when $\varphi > 0$, dislocations move by bypassing the dislocations.

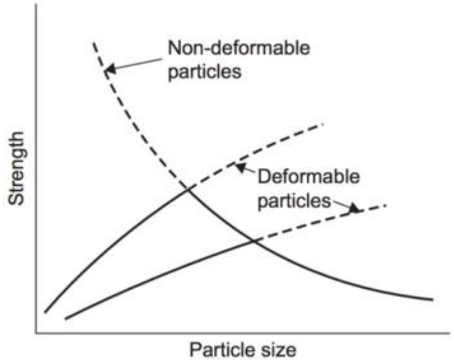

Figure 3-23: Variation of strength with particle size [74].

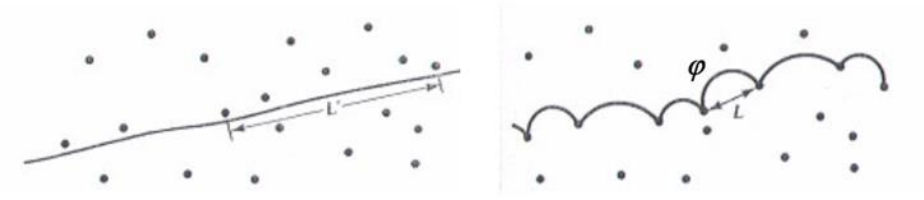

(a) (b)

Figure 3-24: Dislocation moving through precipitates by (a) shearing ($\varphi \approx 0$), (b) bypassing ($\varphi \approx \pi$) [75].

The Orowan looping mechanism is used to explain the bypass phenomenon for dislocations. As the degree of bowing increases, tension is created in the dislocations (Figure 3-25). Yielding occurs when the bowed dislocation becomes semi-circular in shape. After yielding, the dislocation leaves an Orowan loop around the particles, which restricts the dislocation motion further, thus increasing strengthening. The stress created by Orowan loops can be calculated using Equation 3-4:

Equation 3-4

$$\boldsymbol{\tau_y = \frac{\mu b}{L}}$$

where $\tau_y =$ shear stress

$\mu =$ Constant, material dependent

$b =$ Burger's vector of dislocation

$L =$ Distance between two precipitates

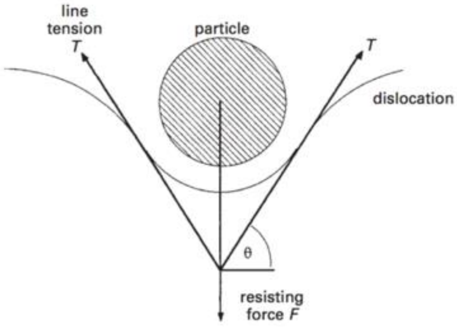

Figure 3-25: The bowing of the dislocation around a precipitate [68]

According to Figure 3-23, there is an optimum particle size for precipitation hardening. For aluminum alloys, it is approximately 2nm, which is the size of η' phases, hence the yield strength is the highest in the peak-age condition. In the Al-Zn-Mg alloy system, the contribution of precipitation strengthening to the yield strength is approximately 70% [38].

3.6 Previous Industrial Casting Trials

Two previous industrial HVHPDC trials were carried out on to compare the castability and mechanical properties of the newly developed Al-7xxx alloy against the state-of-the-art alloy, Silafont 36. To compare castability, all of the alloys were cast using the same dies in their respective casting temperatures and parameters. Figure 3-26 shows the two cast components used during the trials. The shocktower and modified top hat components are used to gauge the castability and compare the uniaxial tensile properties of the alloy compared to Silafont 36, in an industrial component. Areas of the component were sectioned off the machined into tensile bars according to ASTM B557M-15 (refer to Section 4.1).

The composition of the Al-xxx alloy is listed in Table 3-5. It is worthy to note that this composition was modified for medium strength and elongation. The melt temperature of the Al-7xxx alloy is 750°C, with the mold preheated at 200°C. Silafont 36 was cast at 680°C, and the mold was preheated to 150°C. Figure x shows the uniaxial tensile test comparison between the Al-7xxx alloys and Silafont 36 [76].

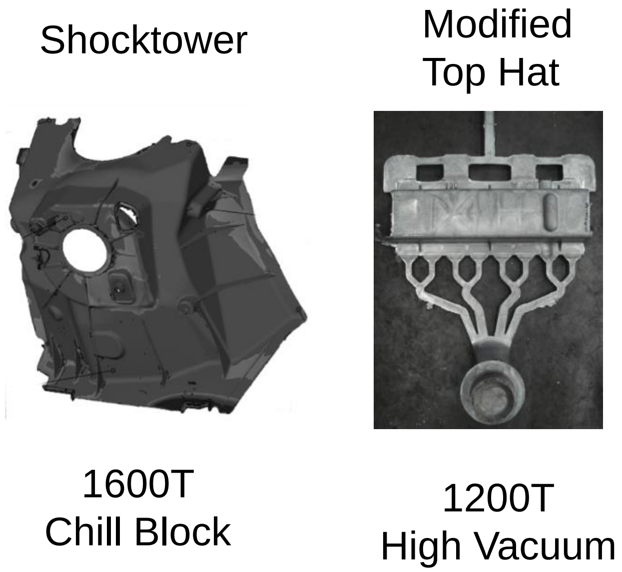

Figure 3-26: The cast components produced during the trial and the respective casting parameters for the 7xxx alloy and the state-of-the-art alloys.

Table 3-5: The targeted compositions of the alloys used in the industrial trials in weight percent (wt%).

Alloy	Al	Zn	Mg	Fe	Ti
	Bal	5	1.5	1	0.01

It is evident that from the data presented in Figure **3-27** and Table 3-6, that the Al-7xxx alloy has superior strength (yield strength and UTS), while having comparable elongation when cast in the same conditions.

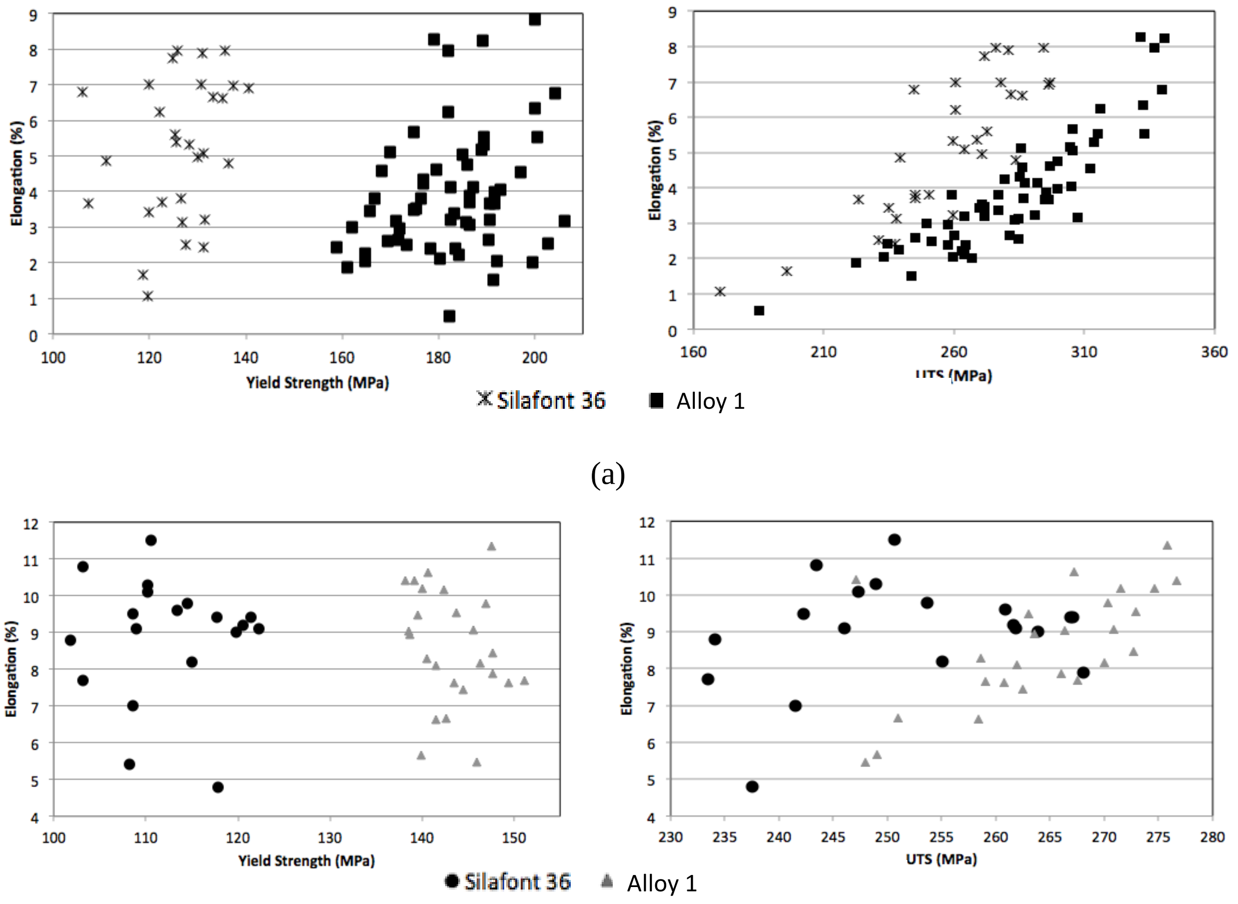

(a)

(b)

Figure 3-27: The uniaxial tensile properties comparison between Silafont 36 and the newly developed Al-7xxx alloys, (a) shocktower, as-cast and (b) sample die, as-cast [76].

Table 3-6: The comparison of average uniaxial tensile properties of Al-7xxx and Silafont 36.

Shocktower - F	UTS (MPa)	YS (MPa)	El (%)
Al-7xxx	262±14	143±4	8±2
Silafont 36	238±51	120±34	9±2

Top Hat	UTS (MPa)	YS (MPa)	El (%)
Al-7xxx	286±31	182±12	4±2
Silafont 36	257±29	126±8	5±2

Chapter 4 PROCEDURE

The procedure, methodology, and data analyses for the laboratory experiments carried out during this study are outlined in this chapter; the following sections are explained in detail.

4.1 Casting Process

The sample die castings (Figure 4-1) were made in a 1200-ton HVHPDC facility at CANMETMaterials. The machine used is a modified version of the cold-chamber HPDC with a pre-heated shot sleeve to minimize early solidification of the liquid melt. Prior to the casting trial, the master alloys were weighed appropriately, and an alloy melt was prepared in a 500 lb crucible electric furnace; 99.98% pure Al, Al-52wt%Mg, Zn-4wt%Al, Al-80wt%Fe and Al-5Ti-1B master alloys were used to make the final alloy composition. The liquid melt was degassed with ultra-high purity (<2ppm O_2) Ar gas through a rotating degasser for 30 minutes. The alloy composition was measured 15 minutes prior to the casting and measured two more times during the casting trial (middle and end). Thermocouples were placed inside the crucible and shot sleeve to monitor and measure the melt temperatures at each shot, the process parameters were as follows:

- Pouring temperature: 750°C
- Die temperature: 200°C
- Preheated shot sleeve: 150°C
- Manual metal pouring with a 10lb ladle
- Manual lubricant spray
- Plunger diameter: 1.25 in

- Cooling channel in Die: water
- The ingate velocity, casting pressure, hold time, slow injection and fast injection speeds were varied and controlled during the trial.

After the castings were ejected, they were air cooled to room temperature on a steel drying rack. Figure 4-1 is a full shot of the sample die casting with all of the components labelled. Since the castings were done with manual pouring, there is a lot of variability between the pouring speed and amount of metal in each shot. In order to minimize these factors, the corrosion plate casting (Figure 4-2) was used for the evaluation of properties and optimization of the T4 solution heat treatment process. Preliminary uniaxial tensile tests were conducted to determine the effect of orientation of the tensile test bars that were machined out of the flat corrosion plate sample; it was concluded that the directionality of the tensile bar (i.e.: obtained from a horizontal or vertical section) showed no significant variations in the uniaxial tensile properties. A total of 11 rectangular strips were sectioned from the plate castings, and the edges were filed smooth. A computer code for the computerized numerical control (CNC) machine was created with the dimensions specified by the ASTM B557M-15 sub-size specimen (Figure 4-3) and used to mill the tensile bars [77].

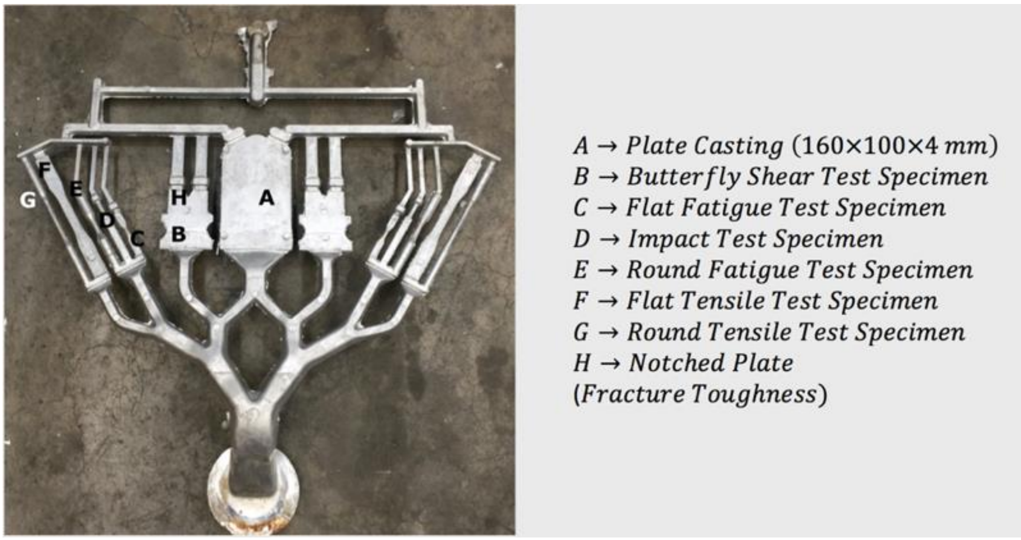

Figure 4-1: Sample die casting with labelled components.

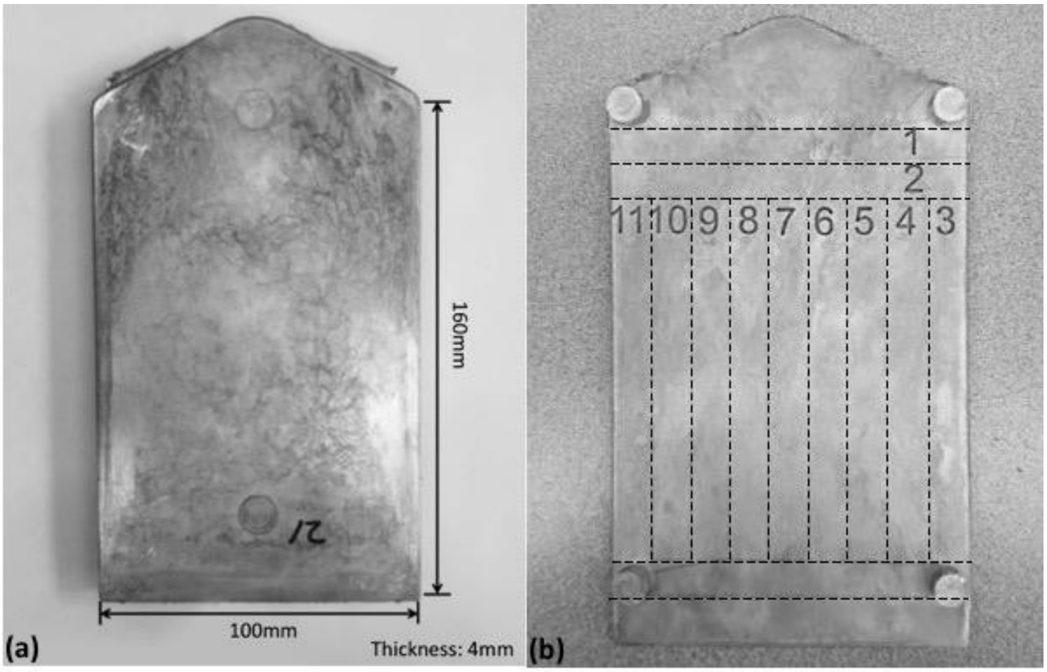

Figure 4-2: The plate casting, showing the tensile bar locations before milling. (a) the front view with dimensions (b) the back view.

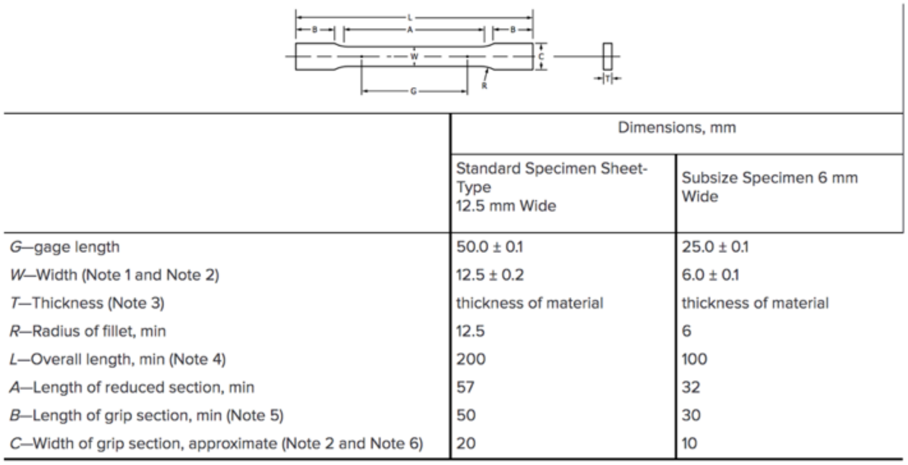

	Dimensions, mm	
	Standard Specimen Sheet-Type 12.5 mm Wide	Subsize Specimen 6 mm Wide
G—gage length	50.0 ± 0.1	25.0 ± 0.1
W—Width (Note 1 and Note 2)	12.5 ± 0.2	6.0 ± 0.1
T—Thickness (Note 3)	thickness of material	thickness of material
R—Radius of fillet, min	12.5	6
L—Overall length, min (Note 4)	200	100
A—Length of reduced section, min	57	32
B—Length of grip section, min (Note 5)	50	30
C—Width of grip section, approximate (Note 2 and Note 6)	20	10

Figure 4-3: The dimensions of the tensile bar (ASTM B557M-15) [77].

4.2 Heat Treatment

The purpose of solution heat treatment is twofold; to improve the alloy's mechanical properties and to understand the mechanisms leading to strengthening. In order to do so, two sets of solution heat treatments were conducted to cover a large variety of solution times. The furnace used during all of the heat treatments (Figure 4-4) is an industrial sized furnace from Pottery Supply House with a large internal fan. The fan was turned on during the entire process to ensure the temperature was even throughout the entire furnace. The initial heat treatment, which can be seen in Figure 4-5, was to determine the highest potential of the alloy's mechanical properties. It consists of a 24-hour, two-step heat treatment at 450°C and 475°C, which helps with the dissolution of the $Mg(Al,Zn)_2$ phase. The tensile bars were inserted into the furnace at room temperature, and temperature increased at 60°C/h until 450°C and held for 11h, then increased again to 475°C at 5°/h and held until a total of 24 hours was reached. The samples were then quenched with room temperature water and stored for natural aging.

(a) (b)

Figure 4-4: The industrial-sized furnace used for heat treatments (a) the inside of the furnace (b) the internal fan.

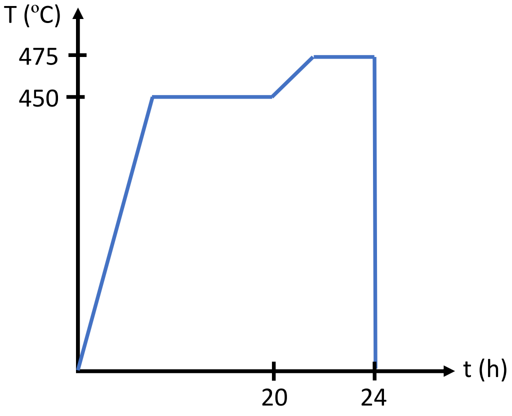

Figure 4-5: Schematic showing the 24-hour solution heat treatment process.

The second set of heat treatments was the first attempt at decreasing the incubation time. The tensile bars were randomly divided into groups of 5 and steel wire was wrapped tightly around the grip sections of each group bundle in order to hold them in place. Figure 4-7 shows the bound tensile bars. The furnace was turned on and programmed to 475°C the day before the heat treatment and left overnight for the temperature to stabilize. The samples are then hot inserted into the furnace and air quenched using an industrial-sized fan. The tip of an exposed K-type thermocouple was inserted into the gauge section of a dummy bundle group and inserted into the furnace to measure the temperature throughout the solution heat treatment process. The temperature measurements were taken with the National Instruments NI SCXI-1000 chassis with a SCXI-1303 data acquisition module hardware, at a rate of 20 samples per second. Figure 4-6 shows the heating and cooling curves of the samples during solution heat treatment. From the derivative shown, the initial heating rate was approximately 3.2°C/s, whereas, the initial cooling rate was approximately 4°C/s.

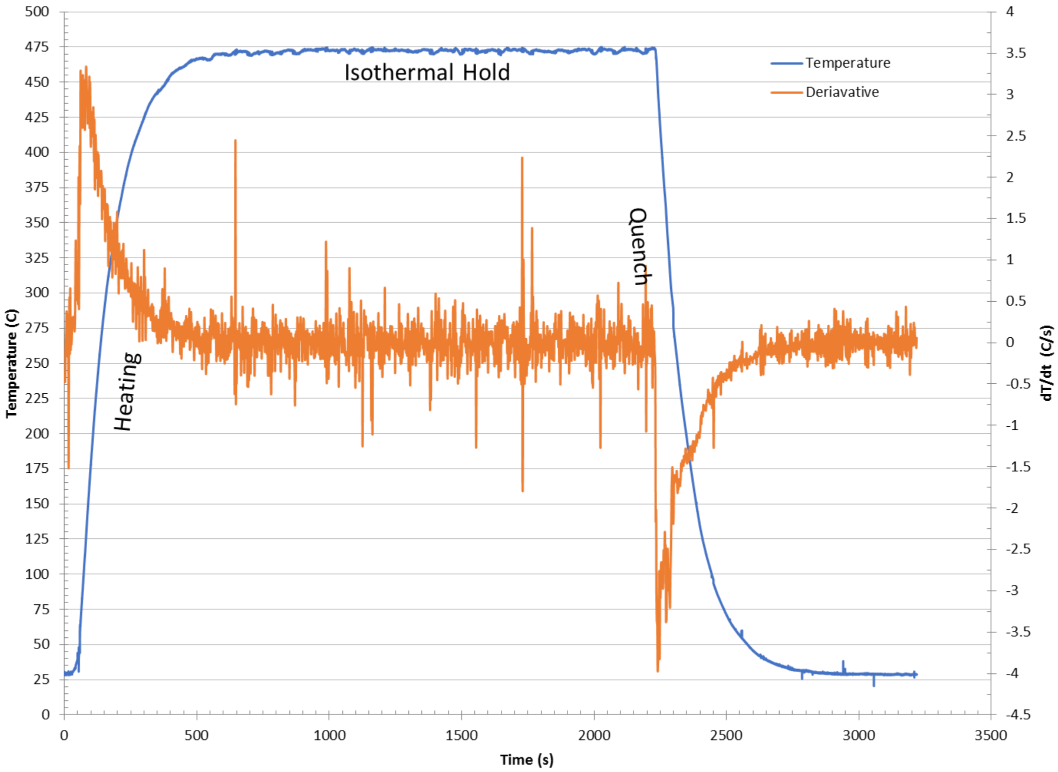

Figure 4-6: Graphs showing the heating and cooling curves of the tensile bars during solution heat treatment.

Forced air quench was selected to be the quenching method in order to mimic the industrial setting. Industrial heat treatment trials concluded that although cold water quenching resulted in higher strengths, the castings were often distorted due to large residual stresses. Distortions were mitigated by forced air quench. The solution heat treatment times tested for this project are as follows: 0.25h, 0.5, 0.75h, 1h, 2, 3h, 4h, 5h, 6h, 7h, 8h, 9h, and 10h.

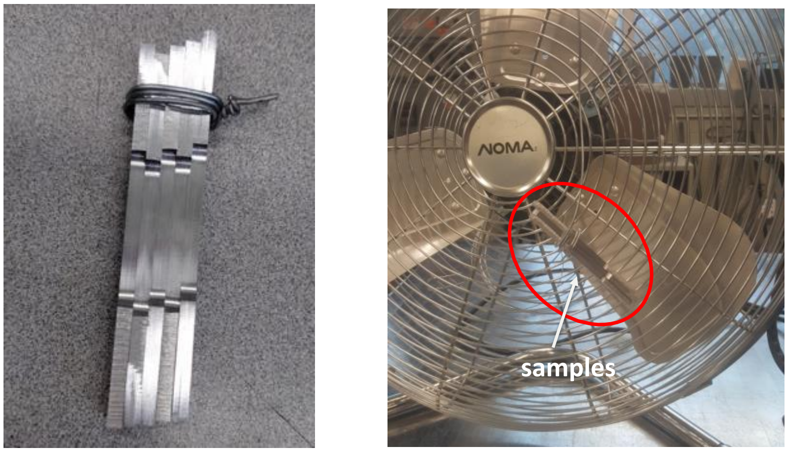

(a) (b)

Figure 4-7: Setup for heat treatment. (a)The bound tensile bars and (b)_ quenching with fan.

4.3 Thermal Analyses Setup

A two-thermocouple solidification experiment [78] was performed on the alloy to determine the phase analyses during slow solidification in still ambient air. A 300g sample of the metal was placed in a crucible and melted at 750°C. Once taken out of the furnace, the crucible was placed on an insulating brick and covered with an insulated material so as to minimize heat transfer from these surfaces. A thermocouple was placed in the centre and edge of the crucible, respectively. The thermocouples used were of 1.016 mm diameter and the tips were ungrounded and sheathed with stainless steel. There was a stainless steel (SS316 grade) tube of 1.6 mm diameter used to enclose the thermocouples. The data acquisition was carried out using the Labview SCXI-1303 module mounted in a National Instrument SCXI-100 chassis; at the rate of 100 data per second. Figure 4-8 shows the experiment setup for the solidification experiment.

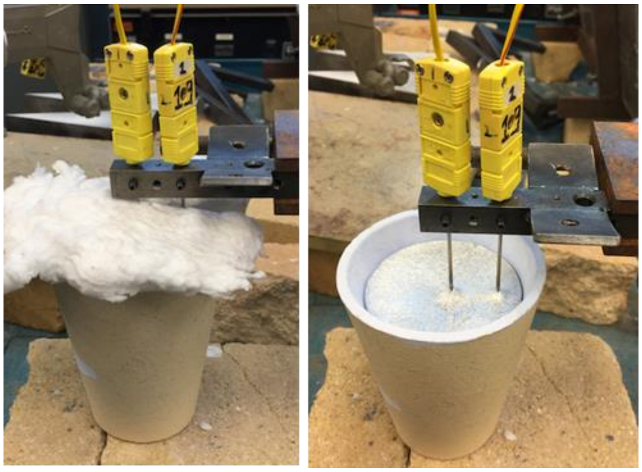

Figure 4-8: Experiment setup to determine the transient thermal curve during solidification, using two thermocouples.

4.4 Bulk Hardness

Immediately after quenching, the bulk hardness or macro-hardness of the samples was measured using the Wilson Rockwell hardness tester with a 1/16” ball indenter and 100-kg force and the Rockwell B scale. Figure 4-9 shows the setup of the hardness tester. One test was performed on the grip section of every tensile bar in one incubation time group and an average value was calculated. A hardness curve was plotted for every incubation time. The tests were performed in approximately 24-hour intervals, starting immediately after quenching. A distance of at least 5mm was kept in between tests in order to prevent the localized nucleation of aging precipitates from the increased stress that would increase the local hardness. Hardness tests were performed in accordance to the ASTM A833-17 test method [79]. Hardness data was acquired until there was no change in the average hardness value for two consecutive days, and then the uniaxial tensile tests were performed on those samples.

Figure 4-9: The bulk hardness tester used during this project.

4.5 Uniaxial Tensile Test

Uniaxial tensile tests were performed on both the as-cast and T4-solutionized samples. Prior to the test, a visual inspection was carried out on the solutionized samples to check for any blistering that may have incurred during the heat treatment, especially in the gauge section. Uniaxial tensile tests were performed using the MTS Insight 50kN uniaxial tensile machine. The entire set-up can be seen in Figure 4-10. The strain rate was set to 1mm/min. The width and thickness of the gauge section of each tensile bar was measured using a caliper prior to the test and input into the software, TestWorks 4[‡]. An external extensometer was placed perpendicular on the gauge section and measured the displacement during the test. After the tensile tests were performed, fracture surfaces were sectioned and analyzed in the SEM for fractography analysis.

[‡] Testwork4 MTS Systems Corporation


(a) (b)

Figure 4-10: The tensile machine used for uniaxial tensile tests (a) the set-up (b) close-up image showing the on-line digital extensometer.

4.6 <u>Microstructure</u>

A part of the grip section of the tensile bars (from the flat tensile bar casting and the plate casting) were sectioned using a rotating table saw to reveal the cross-section. To prepare for microstructure analysis, the samples were hot mounted in Bakelite, then ground and polished to 0.05μm colloidal silica suspension. The samples were etched using 0.5% HF for secondary phases, and Keller's reagent for grain size analysis for optical microscopy. For scanning electron microscopy (SEM), the samples were left unetched. Immediately after polishing, the samples were coated with carbon to reduce charging and nickel paste was applied to the surface for electrical conductivity.

Optical microscopy using a light microscope, Nikon Eclipse LV100, was used for some of the low-magnification grain analyses and microstructural images of samples in the as-cast state. Secondary electron and backscatter images of the alloy were taken in the as-cast condition and at every heat treatment time using the scanning electron microscope. The microscopes used were the JEOL 6610LV and the TPSGAN VP. Multiple images were taken at different location of the samples for phase fraction and grain size analyses. The point & ID feature in electron-dispersive X-ray spectroscopy (EDX) was used for phase identification purposes.

Additionally, EDX line scans were performed on the as-cast and heat-treated samples from 0.25-2h with low excitation voltages (5 and 10 KeV) to obtain the concentration profiles of individual elements within the sample. Low voltages were selected in order to reduce the interaction volume of the electrons and obtain a surface analysis. A line was drawn across a section that contained multiple grains and left for 10 scans across a 1024-point spread.

4.6.1 EDX Interaction Volume

Monte Carlo simulations for the interaction volume produced by electrons with 5keV and 10keV energy were completed using Casino V2.5.1.0[§]. 1x10^4 electrons were used as the sample size for both simulations to obtain more accurate results. Figure 4-11 presents the results. From the figures, it can be seen that the maximum penetration depths are approximately 2.189μm and 10μm, respectively. The average grain size of this alloy was 11.7±1.3μm, so the penetration depth is almost equivalent to the size of one entire grain. This proves to be a source of error for the EDX line scans completed using 10keV energies.

**Casino V2.5.1.0

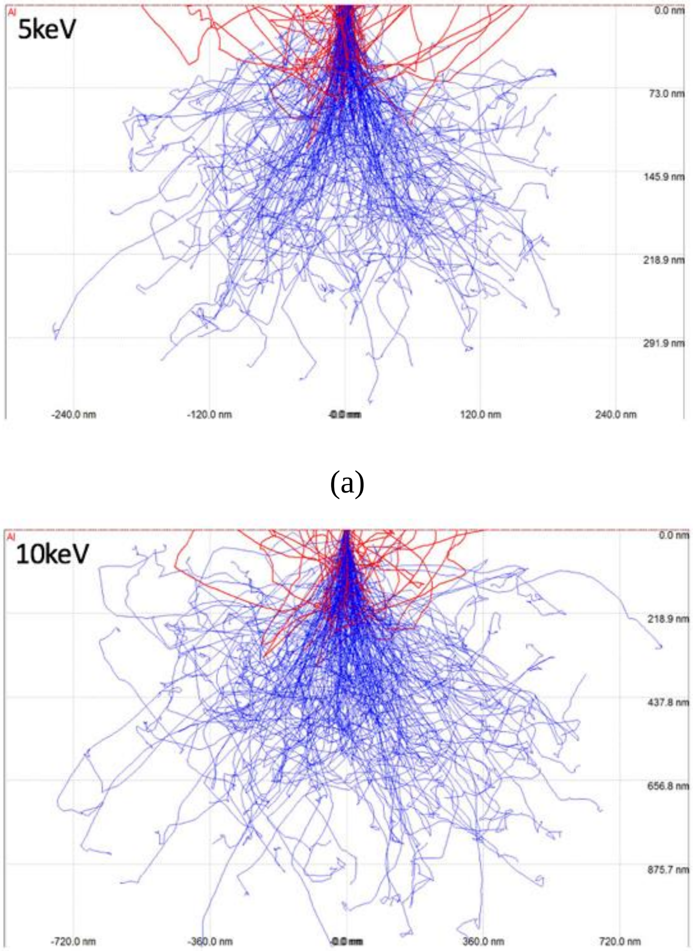

(a)

(b)

Figure 4-11: Monte Carlo simulations for the electron interaction volumes with energies of (a) 5keV and (b) 10 keV.

4.7 Microstructural Analysis

The microstructural analysis portion of the alloy uses the image processing software, ImageJ as well as the optical and SEM images. The following analyses were completed:

- 4.7.1 Phase Fraction Analysis
- 4.7.2 Average Grain Size
- 4.7.3 Grain Size Distribution

4.7.1 Phase Fraction Analysis

To calculate the phase fraction of the alloy, SEM backscatter images were selected due to the greyscale contrast of the phases (from elemental contrast). The original microstructure image (Figure **4-12**(a)) was loaded onto the software and the scale was set by measuring the magnification marker. Then, using the threshold tool (Figure **4-12** (b)), the threshold of the image was changed until only one of the phases was selected. The sum of the area of all of the particles was calculated using the analyze particle tool. The process is repeated until every phase had been accounted for. Figure **4-12**(c) shows the Al_6Fe/Al_mFe particles analyzed by the process. The entire process was completed in accordance to the ASTM standard E1245-03 [80].

One drawback with this technique is that the different Al-Fe intermetallic phases could not be separated by contrast due to their very similar compositions. In order to combat this, the $Al_{13}Fe_4$ phase particles were manually selected based on the difference in morphology. After its phase fraction was counted, these phases were subtracted from the image using the subtraction tool. It was difficult to separate the Al_mFe and Al_6Fe due to their very similar morphology and greyscale contrast. Instead, these two phases were counted together in the phase fraction calculation. Figure 4-12 shows screenshots of the entire process. A total of 6 images from different parts of the cross-section were analyzed for each heat treatment time (including as-cast) and an average phase fraction percentage was recorded.

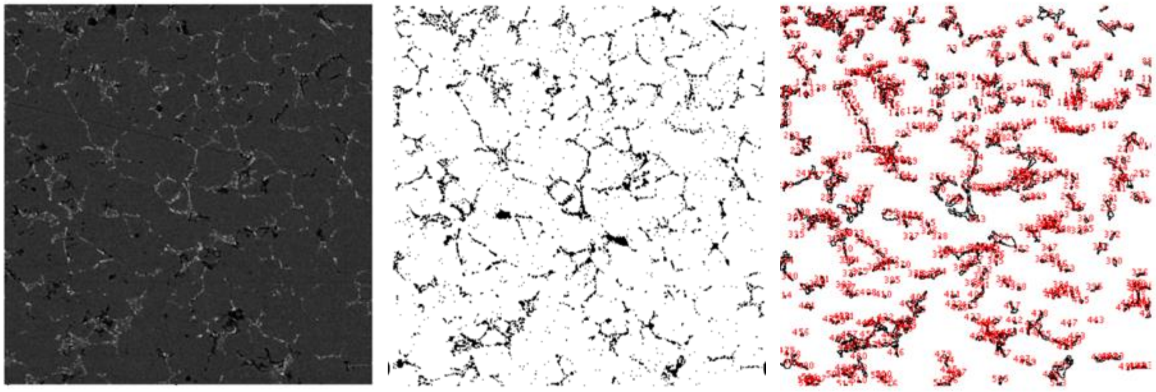
(a) (b) (c)

Figure 4-12: Quantitative image analyses using the ImageJ software showing (a) the original microstructure image, (b) threshold adjusted to select the Al_mFe/Al_6Fe phases, and (c) analysis of the phase fraction area of the particles.

4.7.2 Average Grain Size

The average grain size and grain size distribution of the alloy were both calculated using SEM images. To calculate the average grain size, an image was loaded onto ImageJ and the scale calibrated. The lineal intercept method outlined in ASTM E112-13 was used [69]. The images used were 500X and 1000X magnification. Images of the as-cast and T4-solutionized samples (solution time: 2, 5, and 10 hour) were both used to determine whether recrystallization occurred during solution heat treatment.

A sufficiently long line was drawn on top of the image and the number of grains intersecting or intercepting the line was counted. A minimum of 20 lines were drawn for each image with 4 different orientation of lines (0°, 45°, 90° and 135°), shown in Figure 4-13. An intercept was defined as "a segment of test line overlaying one grain". When counting intercepts, the segment that penetrates part of a grain would be counted as a half-intercept. An intersection is defined as "a point where a test line is cut by a grain boundary" [69]. Half-intersections cannot be counted unless the line drawn touches a grain boundary exactly or tangentially.

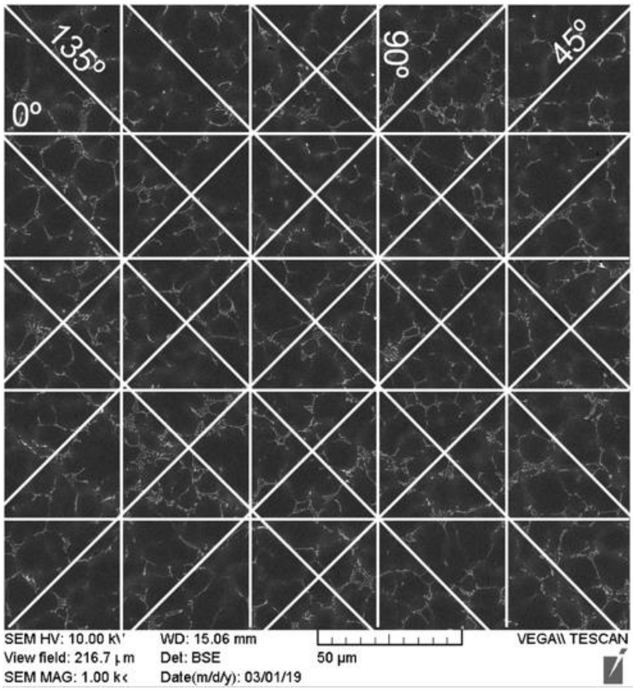

Figure 4-13: The lineal intercept method of determining average grain size with 4 orientations of lines: 0°, 45°, 90° and 135° and a total of 22 lines.

4.7.3 Grain Size Distribution

The grain size distribution was calculated to determine the amount and size of PSGs vs. normal grains in the microstructure. The software, ImageJ, along with 5 SEM images taken at 1000X was used for this calculation. The threshold of the images was adjusted to show the grain boundaries. The grain boundaries were traced to increase contrast, whereas the intermetallic phases, porosity, and coring effects in and around the grains were removed (Figure 4-14 (a)). Note, the white particles in Figure 4-14 (a) showed the locations of the grain boundaries and intermetallic phases. Then, "measure particles" tool was used to determine the area of the grains, Figure 4-14 (b) shows the outlines of the grains after measuring. An average of the grain size distribution from these images were taken and plotted.

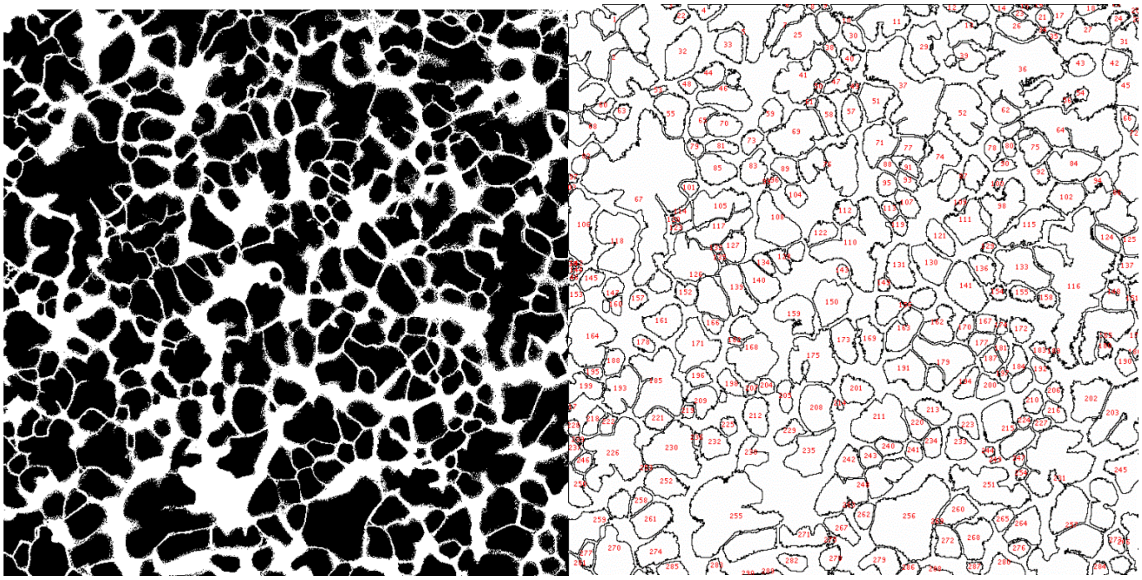

(a) (b)

Figure 4-14: Images taken from ImageJ showing (a) the grain size after threshold adjustment (b) grain area calculation after analysis.

Chapter 5 RESULTS AND DISCUSSIONS

This chapter presents the various results and analyses from the experiments in the project.

- 5.1 Rationale of the Alloy Development
- 5.2 Casting Quality
- 5.3 Microstructure
- 5.4 Uniaxial Tensile Properties
- 5.5 Bulk Hardness Curves
- 5.6 Homogenization Model

Before the details of the results are presented, a rationale is presented on the development of the Al-4Zn-1Mg-1.2Fe-0.01Ti alloy, used in this study.

5.1 Rationale of Alloy Development

The alloy in this study was developed to enable high integrity castings manufactured using the HVHPDC process for structural automotive application. The composition (in wt%) of the Al-Zn-Mg-Fe alloy with standard deviations is listed in Table 5-1, as measured by spark optical emission spectroscopy (Spark OES).

Table 5-1: Composition (wt%) of the 7xxx series alloy selected for this project as measured by Spark OES.

	Mg	Zn	Fe	Ti	Al
Targeted	1	4	1.2	0.1	Bal.
Achieved	1.00±0.02	4.03±0.05	1.20±0.08	0.09±0.01	Bal.

The Al-Zn-Mg system was chosen so as to have an alloy with the levels of the primary alloying elements, less than their respective maximum solubility in equilibrium conditions; so as to maximize the solute dissolution in the primary Al matrix. However, an alloy within the Al-Zn-Mg system would not lend itself to near net shaped casting because of the high susceptibility to hot tearing. The progressive evolution of fraction solid as a function of temperature, during solidification, for the alloy, with and without Fe addition to the same, was simulated using Pandat*, with the Scheil-Gulliver solidification paradigm, and shown in Figure 5-1.

The Scheil-Gulliver paradigm is a model for one form of non-equilibrium solidification. It has three main assumptions [81,82]:

1. There is no diffusion in the solid phase.
2. There is complete diffusion in the liquid phase.
3. Equilibrium is reached at the solid-liquid interface, therefore, the compositions obtained by the phase diagram are applicable.

Although the Scheil-Gulliver paradigm models non-equilibrium solidification, it does not represent the solidification in this project. The solidification rate in this project occurs within one minute, therefore there is little to no diffusion in the liquid phase. However, the Scheil-Gulliver paradigm is a good indicator of the solidification path.

It would be readily observed that addition of iron reduced the liquidus temperature, fraction solid evolved at any given temperature and the range of temperature for solidification from 119 °C (647.99°C to 529.04°C) without Fe addition to 87 °C (642.97°C to 555.77°C) with Fe addition. These thermodynamic changes enable significant reduction in the sensitivity to hot tearing for the alloy.

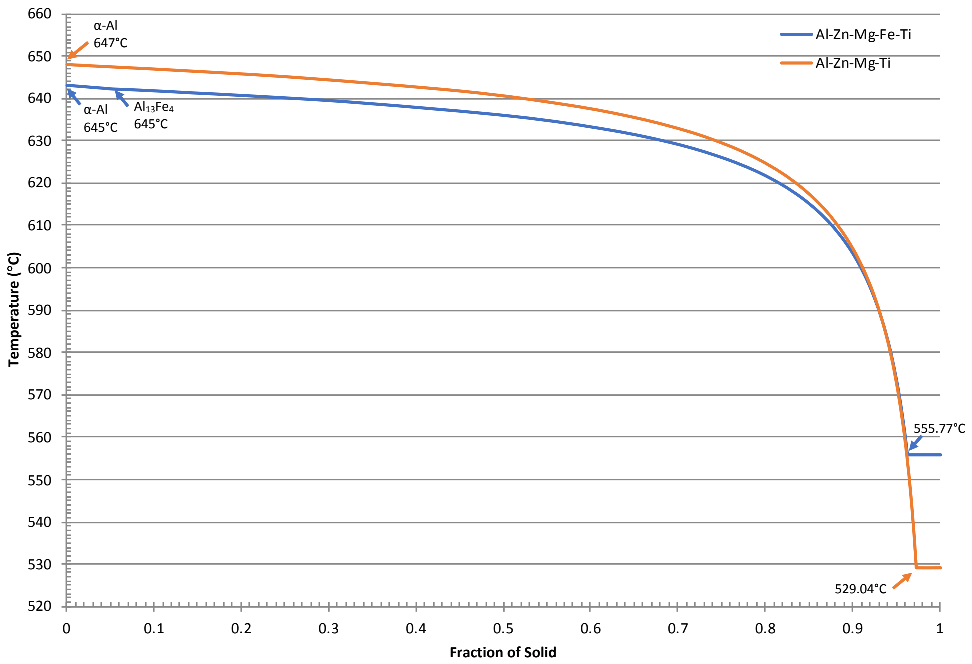

Figure 5-1: The variation of fraction solid as a function of temperature, as obtained by thermodynamic simulation using the Scheil-Gulliver paradigm for solidification in Pandat; the compositions of the alloys herein are shown in Table 5-1.

Titanium was added to the alloy in the form of Al-5Ti-1B master alloy. It exists in the metal as TiB_2 and Al_3Ti. The main purpose of adding titanium as a minor alloying element is to alter the morphology of the grains from dendritic/rosette-shaped to uniform equiaxed grains throughout the casting. In addition, these grains improve the strength of the metal and decreases hot tearing tendencies [65, 66]. Al_3Ti evolves as a primary phase in a peritectic reaction with liquid Al, and it has been shown to be an effective nucleating agent for α-Al grains. Only a small amount of Ti (typically 0.1wt% or less) is necessary to achieve this effect [83], large Al_3Ti phases can have a detrimental effect on properties. During solution heat treatment, titanium also helps to pin the grain boundaries to prevent grain growth and coalpsgence. Figure 5-2 shows the effect of Ti on the grain size and morphology of the primary Al grains in a typical Al 7xxx alloy.

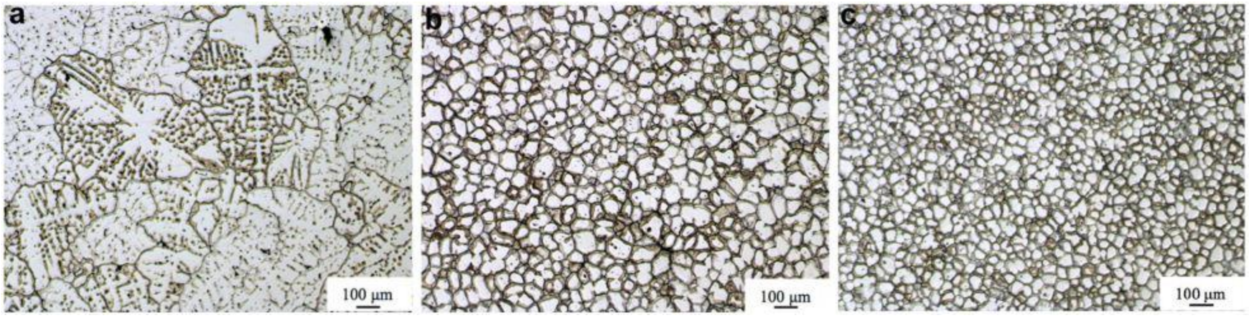

Figure 5-2: The effects of Ti addition on the grain size and morphology of the AA7050 alloy with (a) no Ti addition (b) 0.06wt% Ti and (c) 0.24wt% Ti [83].

Figure 5-3 presents the isopleths of the phase diagram for the Al-Zn-Mg-Fe-Ti with increasing Fe concentration as a function of temperature; Figure 5-3 (a) shows all of the equilibrium phases that may evolve during solidification and Figure 5-3 (b) presents the equilibrium phases that evolve from the Liquid, only. The composition of this alloy was chosen in particular due to its hypoeutectic iron content, which is confirmed by the phase diagram. The solidification temperatures and reactions for each phase in this system are presented in Table 5-2.

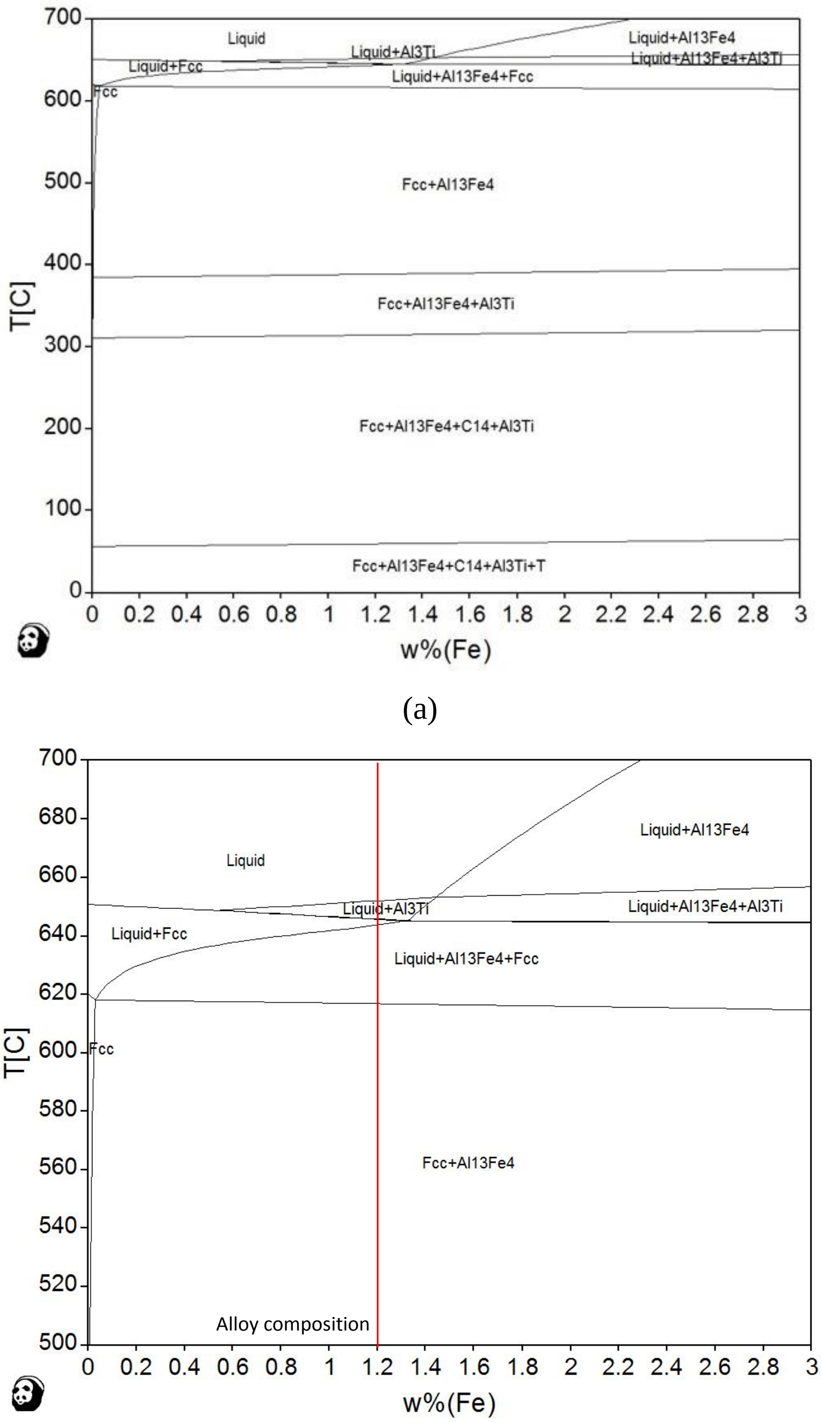

(a)

(b)

Figure 5-3: The simulated Al-Fe phase diagram of the alloy, obtained from Pandat (a) showing all of the secondary phases (b) The red dotted line shows the percentage wt% of Fe at the eutectic point.

Table 5-2: Prediction of solidification from simulations using Scheil-Gulliver paradigm

Temperature (°C)	Phases
651.9	$Liquid + Al_3Ti$
645.4	$Liquid + Al_3Ti + \alpha(Al)$
643.3	$Liquid + \alpha(Al) + Al_{13}Fe_4$
556	$\alpha(Al) + Al_{13}Fe_4$

5.1.1 *Thermal Analyses*

The two thermocouple technique [78] was used to measure the transient thermal profile (temperature versus time) during the cooling and solidification of the alloy melt shown in Table 5-1; the results are shown graphically in Figure 5-4; along with the evolution temperatures of the three major phases.

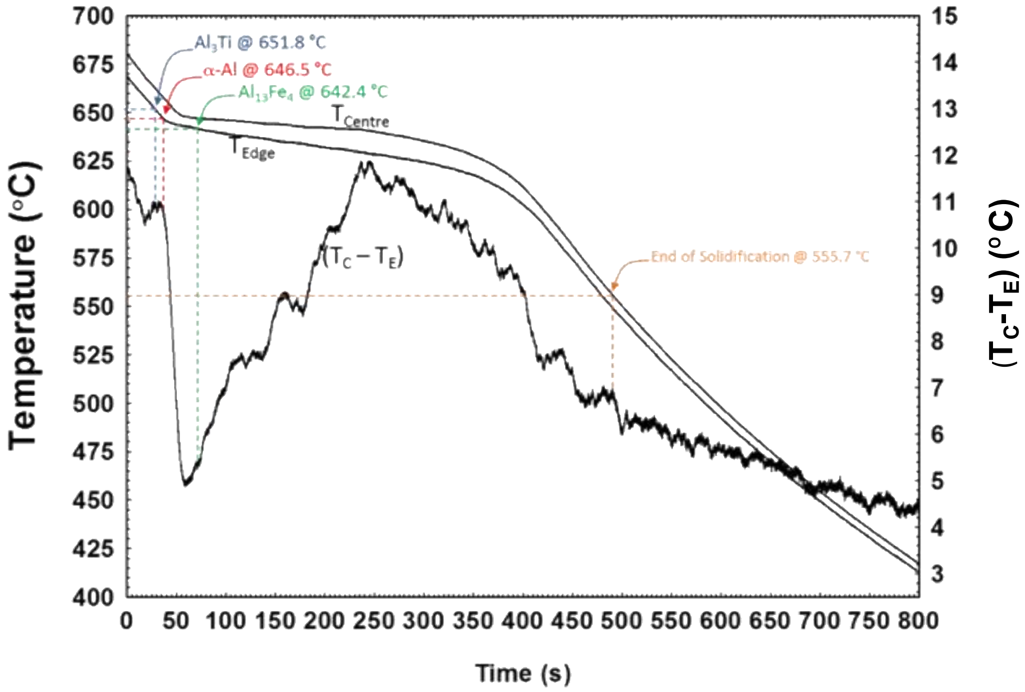

Figure 5-4: Thermal analyses using two thermocouples showing the evolution temperatures of the major phases during solidification.

Notably, the rate of solidification of the two-thermocouple experiment to evaluate the thermal analyses was quite similar to that necessary to satisfy the Scheil-Gulliver solidification paradigm. The evolution temperatures of the three major phases, shown in Figure 5-4 closely matches the ones predicted by simulation in Table 5-2.

5.1.2 Iron Additions

Typically, iron in aluminum alloys is considered to be a contaminant. Section 3.3.2 explained the detrimental effects of the plate-like Al-Fe intermetallic phases on hot tearing, pore formation, and mechanical properties. Despite these inherent disadvantages, iron was still added to this new Al-Zn-Mg alloy. It was initially noticed during experiments and literature review that the morphology of the Al-Fe intermetallics can be changed by varying the cooling rates during solidification. The detrimental plate-like $Al_{13}Fe_4$ is a thermodynamically-stable equilibrium phase, that precipitates during slow cooling rates (< 3°C/s). At high cooling rates, it was discovered by Zhang et al that the morphology of the Al-Fe phases evolves as either a skeletal-like structure in Al_6Fe, or feather-like structure in Al_mFe (m=4-4.4) [50,51]. These skeletal- and feather-like structures are experimentally proven to decrease the tendency of hot tearing by offering increased permeability to the liquid metal feeding the shrinkages in the final stages of solidification. Figure 5-5 presents the difference between the plate-like morphology of the $Al_{13}Fe_4$ intermetallic phase and the more permeable morphologies of the Al_6Fe and Al_mFe phases in a casting from the HVHPDC process, using the alloy in this study.

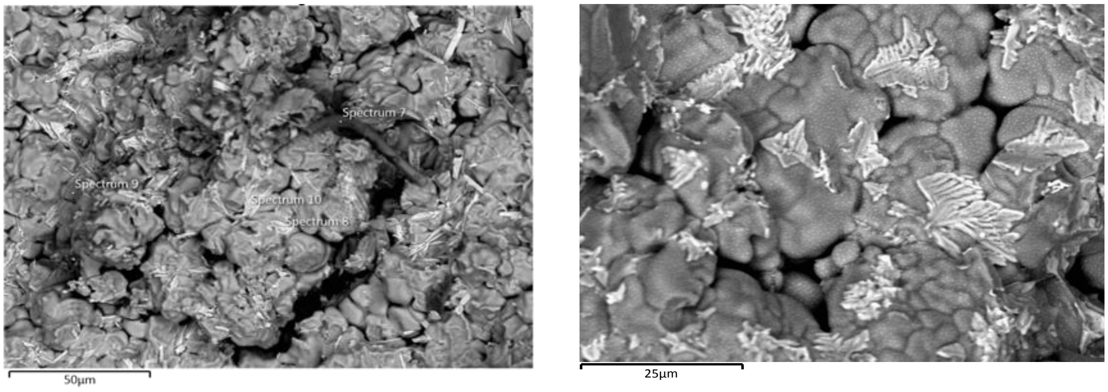

(a) (b)

Figure 5-5: Typical morphology of the Al-Fe intermetallic phases during solidification in a HVHPDC process; (a) $Al_{13}Fe_4$ with plate-like morphology, blocking the intergranular channels during phase evolution and (b) Al_6Fe and Al_mFe phases that evolve at higher cooling rates and present a permeable morphology in the intergranular regions.

Figure 5-6 shows the typical microstructures obtained from the castings of the alloy in this study using the HVHPDC process: resembling a typical polyphase alloy. The Al_mFe and Al_6Fe phases solidify around the grain boundaries of α-Al and prevent the coagulation of shrinkage porosities, thus, decreases hot tearing susceptibility. Due to the high melting temperature of Al-Fe phases, they also have the potential to be used for high-temperature applications.

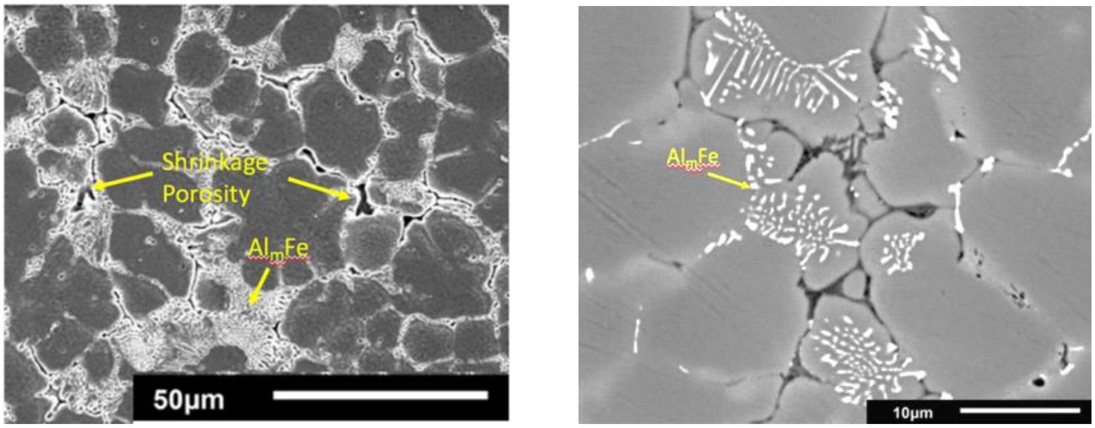

(a) (b)

Figure 5-6: A typical microstructure showing the location of Al_mFe (white) phases around the grain boundaries and the encapsulated shrinkage porosities (a) low-magnification (b) high-magnification.

5.2 Casting Quality

Typically, some castings from the HVHPDC trial were deemed defective due to one or more of incomplete filling, low mechanical properties, and hot tearing issues. In order to determine the causes for the rejections, one flat tensile bar casting from each shot was taken and a uniaxial tensile test was performed on them in the as-cast state. The shot profiles of every shot were also compared. The tensile results were compiled, and two groups were selected in particular for the comparison, the high-elongation group (El ≥11%) and the low-elongation group (El<3%). The shot profiles with elongation percentages are listed for both groups in Figure 5-7 (metal pressure vs. plunger stroke) and Figure 5-8 (plunger velocity vs. time), and the cross-section microstructures images can be seen in Figure 5-9.

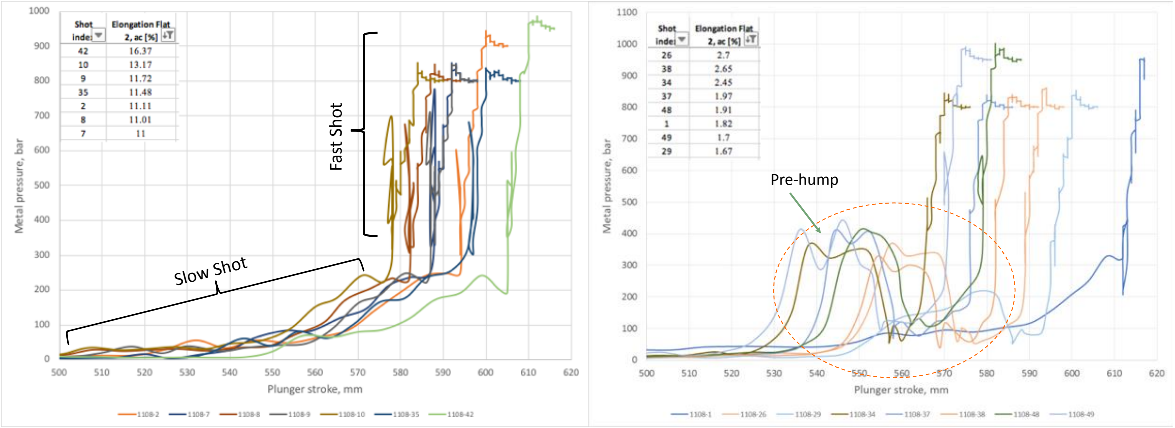

Shot index	Elongation Flat 2, ac [%]
42	16.37
10	13.17
9	11.72
35	11.48
2	11.11
8	11.01
7	11

Shot index	Elongation Flat 2, ac [%]
26	2.7
38	2.65
34	2.45
37	1.97
48	1.91
1	1.82
49	1.7
29	1.67

(a) (b)

Figure 5-7: Shot profiles (metal pressure vs. plunger stroke) of the sample die castings (a) elongation ≥11% (b) elongation <3% with pre-hump

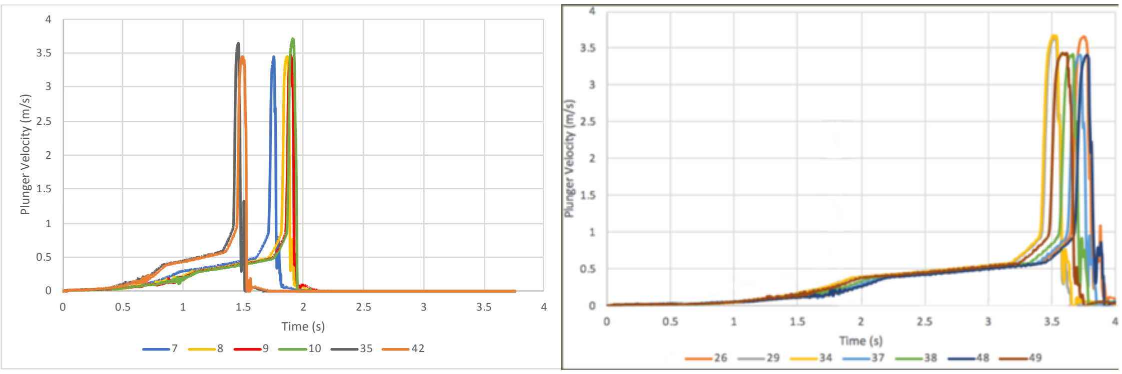

(a) (b)

Figure 5-8: Plunger velocity vs. time profiles from the HVHPDC trials (a) elongation ≥11% (b) elongation <3%

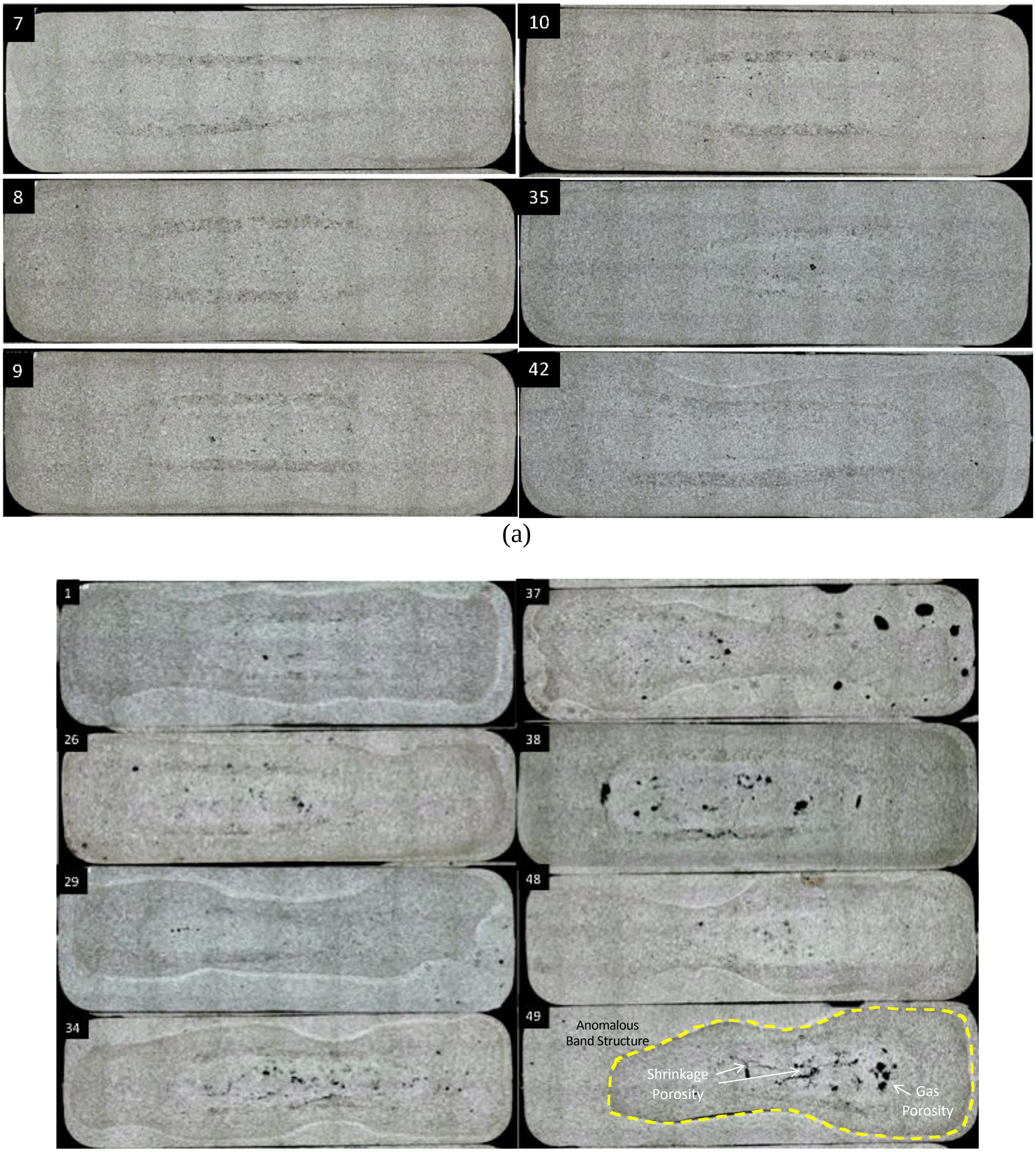

(a)

(b)

Figure 5-9: Typical microstructure of the cross section of a flat tensile test bar casting gauge section from the HVHPDC trials (a) elongation ≥11% (b) <3%.

All of the images in the high-elongation group (Figure 5-7 (a)) had uniform microstructures with minimal porosities. The shot profiles also had no anomalies. The slow shot time was between 1.5 s and 2 s for all the shots in this group of castings. The microstructural images of all of the shots from the low-elongation group (Figure 5-7 (b)) revealed an anomalous shrinkage band structure in the cross-section in addition to a significant increase in shrinkage and gas porosities; as indicated in the microstructure of the casting #49 in Figure 5-9 (b). Furthermore, a closer analyses of the respective shot profiles of the castings that were deemed defective, as shown in Figure 5-7 (b), revealed a notable and anomalous 'hump' feature in the slow shot regime, and there was also a significantly longer slow shot time (Figure 5-8-(b)), approximately 3.5-4 seconds for all of the shots. Shot #1 in Figure 5-8-(b) is the first shot of the trial that was used for general warm up and testing of the machine and could be discarded from any further analysis. Notably, all the shots with a 'hump' in the slow shot regime of the profile showed highly irregular shrinkage bands in the casting microstructure and significantly higher porosity (shrinkage and gas); the irregular microstructure feature will be termed as the 'hump anomalous' in the subsequent sections of this manuscript.

It could be hypothesized that the hump in the slow shot was due to a large amount of pre-solidified metal phases in the shot sleeve, prior to entering the gate section. The temperature of the liquid melt that is in contact with the shot sleeve will be lower due to heat transfer, thus creating a temperature gradient. Solidification likely happens during this stage. Figure 5-10 shows magnified microstructural images of the hump anomalous. It can be seen that there are fine dendritic grains, situated in between equiaxed growth, growing in the direction towards the centre of the casting. Dendritic growth of α-Al occurs only during largely undercooled metals; therefore, it is suspected that the area connecting the hump anomalous originates from the pre-solidified crystals in the shot sleeve. Furthermore, the fracture surface (Figure 5-11) shows the hump anomalous as well as lots of small externally solidified spherical particles that are approximately 100μm in size. The area within the hump anomalous can be seen to have a smooth cleavage, indicating a brittle failure. The area around the hump (around the perimeter of the tensile sample) was seen to have lots of dimpling, caused by extensive plastic deformation, which is indicative of a ductile fracture. The microstructural mismatch between the outer layer, the hump anomalous and the externally solidified spherical particles are the causes for the pre-mature failure and low elongation.

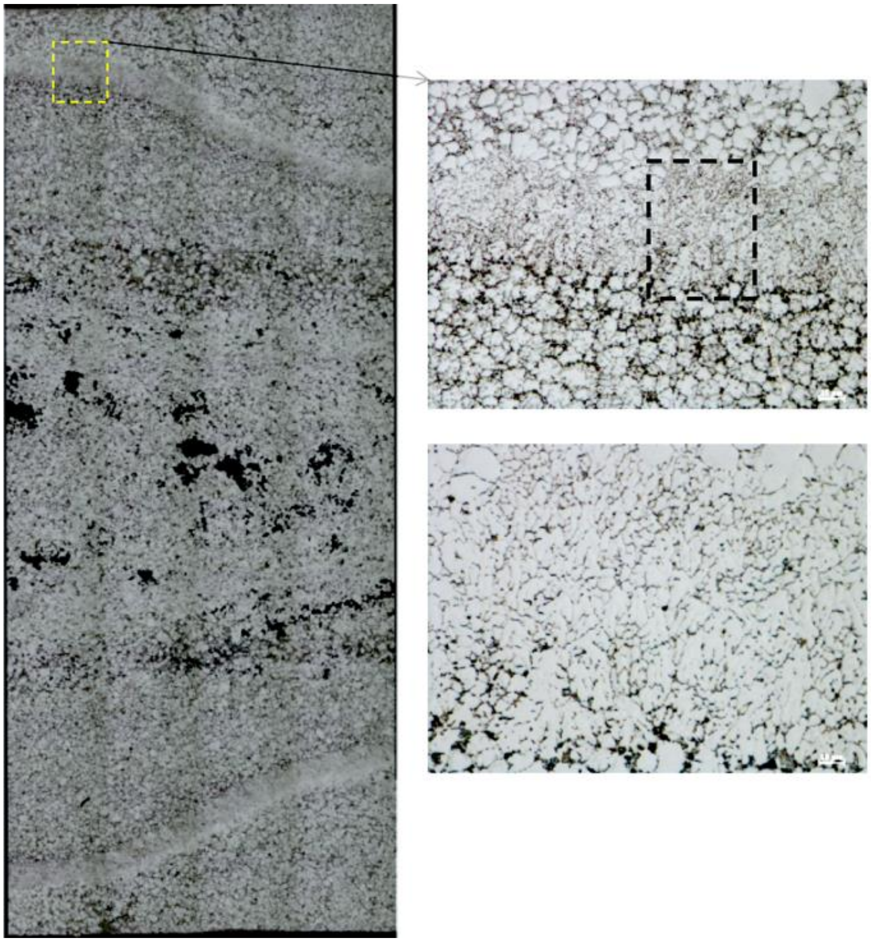

Figure 5-10: Magnified microstructure images of the hump anomalous. A layer of fine dendritic grains is situated between two layers equiaxed grains. The seaweed morphology dendrites can be seen in the image on the bottom right.

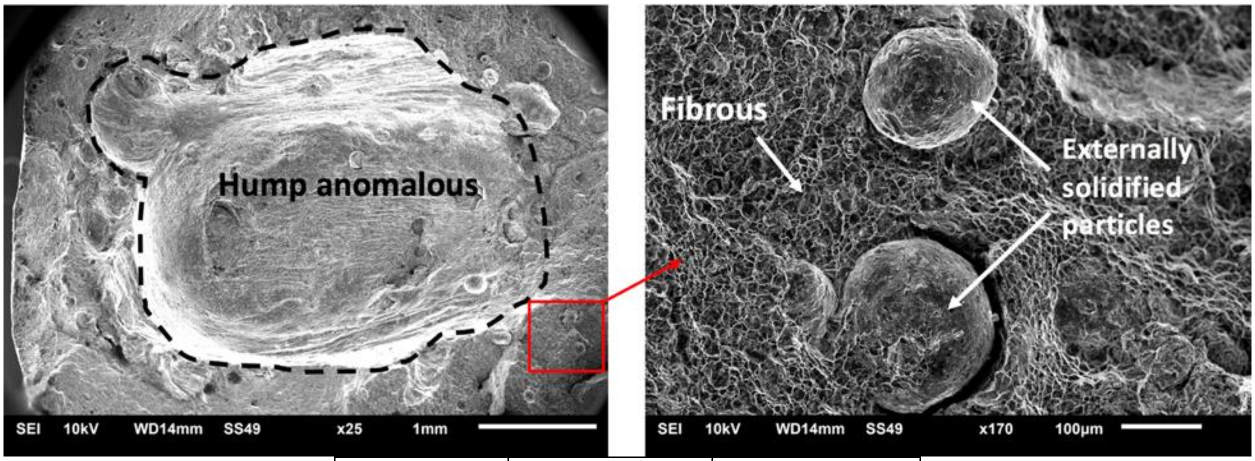

UTS (MPa)	YS (MPa)	El (%)
135.1	110.4	1.67

Figure 5-11: The typical fracture surface of a tensile sample in the low-elongation group and the corresponding tensile properties. The hump anomalous and externally solidified particles are labelled.

A combination of multiple factors could have caused these defective castings, such as inaccurate pouring temperature, undue delay times, manual (inconsistent) pouring, gate design and manual operation of the process. The pouring temperature was consistently measured by one thermocouple situated in the middle of the crucible during the entire casting process. This temperature does not accurately represent the temperature measured at the top of the crucible, where the liquid melt is being ladled out for the pour. Additionally, the top of the crucible was left exposed to the surrounding environment during the entire trial, which leads to a significant temperature difference between the melt at the top and the bottom. Furthermore, the pouring process was entirely manually operated, and there would be a delay of a few seconds between scooping the liquid melt from the crucible and pouring it into the shot sleeve, which would further decrease the temperature. Therefore, it is safe to say that the actual pouring temperature is well below 750°C, most likely around the range of 720°C before pouring.

Manual pouring has another important disadvantage; the amount of liquid melt in every shot is inconsistent. The biscuit size, which is the section that solidifies in the cold-chamber shot sleeve, is a good indicator of the amount of melt poured. Shots with thick biscuits have more metal, which would result in decreased casting and intensification pressures in the process, leading to defective and incomplete filling. Figure 5-12 shows the biscuit thickness of every shot in the trial; the thickness ranged from 2mm to 57mm, which confirms the inconsistency caused by manual pouring. Typically, an automatic robotic pouring system in a commercial environment would be able to maintain the biscuit size within a 10% tolerance off of the optimum thickness.

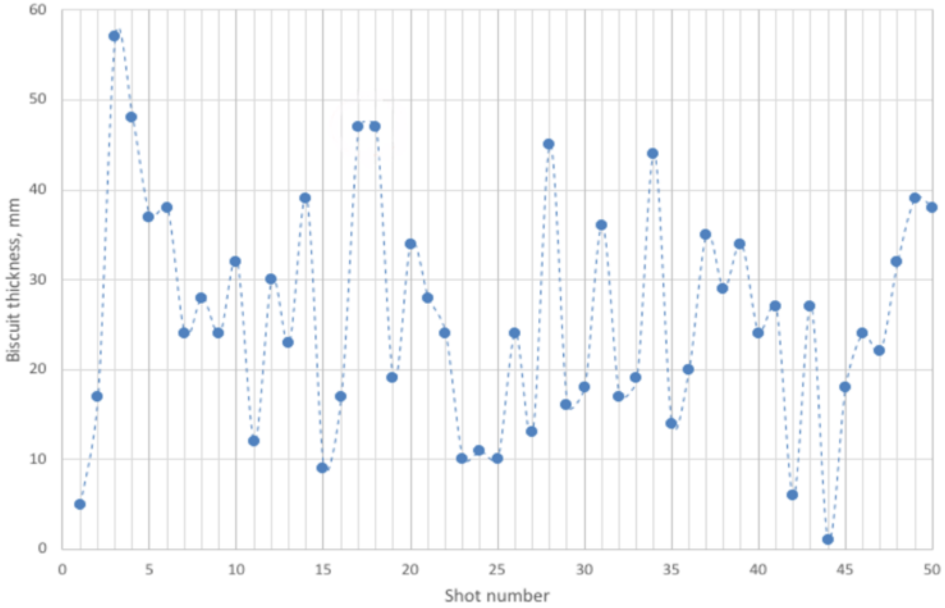

Figure 5-12: Graph showing the biscuit thickness of every shot.

The shot sleeve temperature and the delay time are also very crucial factors to consider, since the liquid melt is already entering the shot sleeve at a reduced temperature. The shot sleeve was preheated to 150°C prior to the trial and consistently monitored throughout. During the trial, the shot sleeve was heated up by the liquid melt to approximately 300°C. Despite the preheat, the significant drop in temperature proves to be a problem because more superheat will be lost during the pouring process. Furthermore, there are two additional delay times that need to be accounted for as well, the time where the metal rests in the shot sleeve before the slow injection initiates and the time between the slow injection and fast injection. Figure 5-13 shows the temperature profile of liquid melt that was solidified in the shot sleeve. It is estimated that in the first second the liquid melt sits the shot sleeve, it experiences a 10 °C decrease in temperature. The Al-Zn-Mg-Fe alloy begins to solidify at 651.9°C, therefore, it is very evident to see why there may be a notable portion of metal that is already solidified before it enters the die cavity. The shot profiles in Figure 5-7 and

Figure 5-8 further strengthens the hypothesize that the hump in the slow shots developed in Figure 5-7 (b) may have been due to the delay time in Figure 5-8 (b).

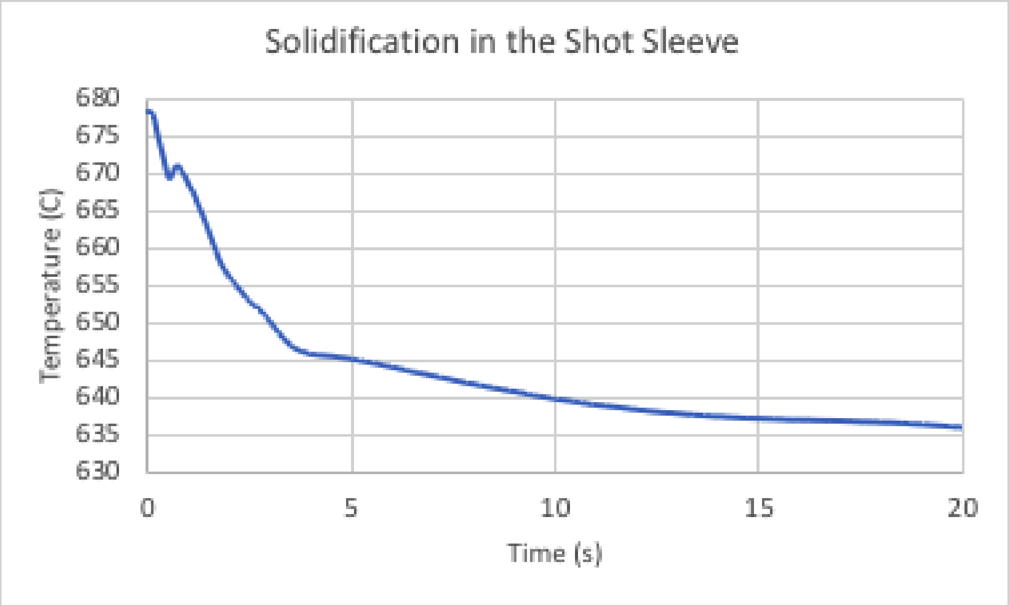

Figure 5-13: Solidification of the Al alloy in the shot sleeve, showing a decrease of 10°C in temperature in the first second.

The aforementioned factors also affect the turbulence and flow of the metal within the die cavity. Figure 5-14 presents the X-ray images of the corrosion plate castings from the same groups. Figure 5-14 (a) (elongation ≥11%) has a thin strip of porosity distributed along the centre of the plate, indicating the direction of flow; the overall porosity level is acceptably low. On the other hand, Figure 5-14 (b) are corrosion plates from the low-elongation group (<3%), where there is a significant amount of porosity, especially in the direction of metal flow, caused by additional turbulence during solidification, from deterring factors such as anomalous solidified crystals and inadequate gate design to accommodate them in flow.

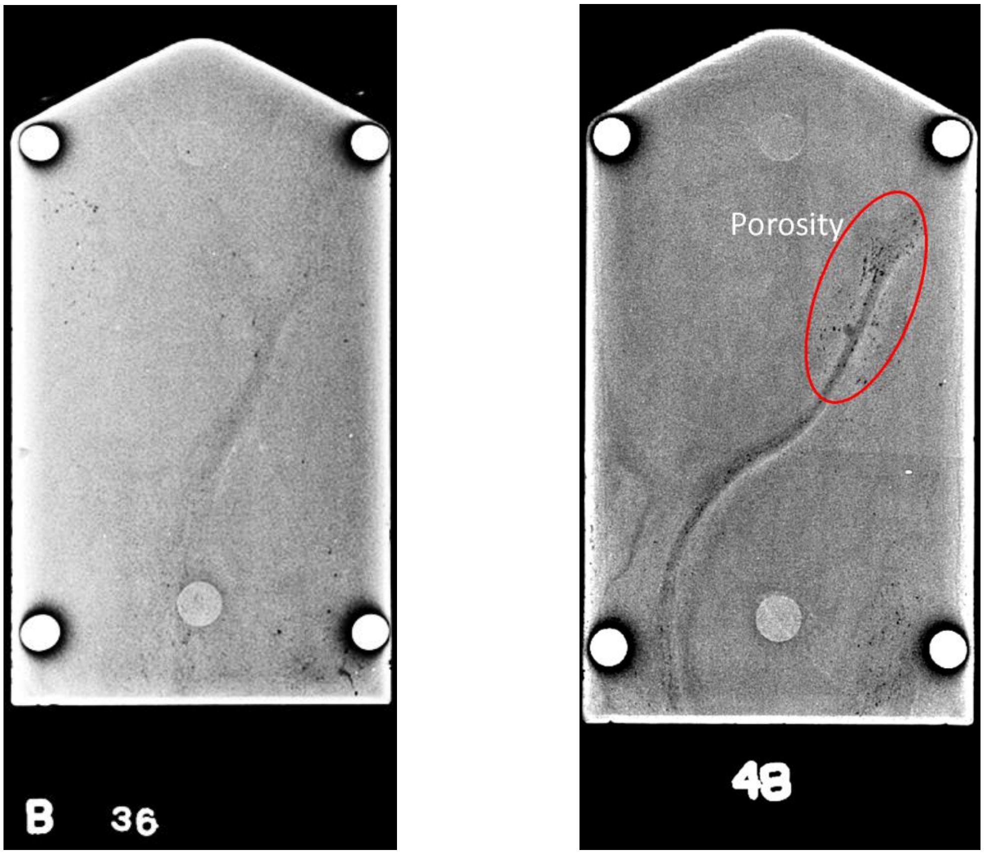

(a) (b)

Figure 5-14: X-ray images showing the flow and porosity distribution within the corrosion plate castings of (a) elongation >11% and (b) elongation <3%

In order decrease the temperature loss, it is imperative to alter the equipment and parameters to optimize the casting process specifically for this alloy. Firstly, the alloy should be cast using a fully automatic HVHPDC process with feedback control system, since it is very sensitive to thermal management of the process. Secondly, the gate thickness should be increased to decrease heat dissipation during filling. Thirdly, the slow shot time should be optimized to a minimum value, as it is seen to produce the best castings.

5.3 __Microstructure__

Figure 5-15 shows typical microstructural images obtained from the cross-section of the plate casting. There are two general morphologies of the α-Al grains, the larger, rosette-shaped grains

(Figure 5-15 (a)) are PSGs from the shot sleeve. The smaller, equiaxed grains (Figure 5-15 (b)) are the ones that are solidified in the die cavity under pressure. Furthermore, it is evident that there are two main phases in the alloy, the primary α-Al grains and the Al-Fe intermetallic phases. The Al-Fe phases can be identified as having a feather-like morphology, typical of the Al_mFe phase. Notably, the 'skin' layer on this alloy, as shown in Figure 5-15, is about 250 μm; typically, the skin in the current state-of-the-art structural HVHPDC alloys such as A365 is about 50 to 100 μm. The skin is critical to the HPDC components because it imparts significant resistance to failure in both the static and dynamic modes of load application and imparts certain additional performance advantages to the component such as resistance to corrosion and wear, as well [84].

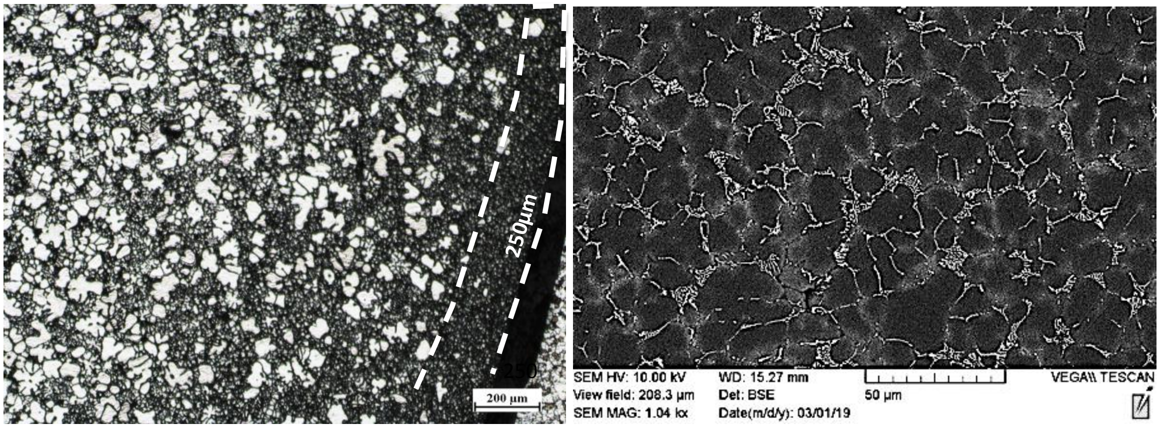

(a) (b)

Figure 5-15: Typical microstructural image from the cross-section of the plate casting (a) Edge section grain analysis, including the measurement of the skin, obtained from optical microscopy, etched with Keller's reagent (b) middle section obtained from SEM, showing the intermetallic phases and the grain structure.

Figure 5-16 presents the differences between the as-cast and T4-solutionized (2 hours) microstructure, respectively, taken in the SEM using the composition backscatter mode. Coring effect in the grains (light border around the grain boundaries) can be seen in the as-cast microstructure. This is due to the extremely fast solidification, causing non-equilibrium solidification. There is a significant reduction of diffusion of solutes in the melt, which leads to a difference in the composition in the solid. As the grain grows outwards in solidification, there is an increase in solute concentration around the boundaries. Since Zn, the most prominent solute in the alloy, has a higher atomic number than Al, it shows up brighter in contrast due to the increased number of backscattered electrons released. Coring was not observed in the T4-solutionized microstructure, presumably due to the grain homogenization that occurs during heat treatment. The same conclusion was found through the EDX line scan plots, which shall be addressed and discussed in Section 5.3.4.

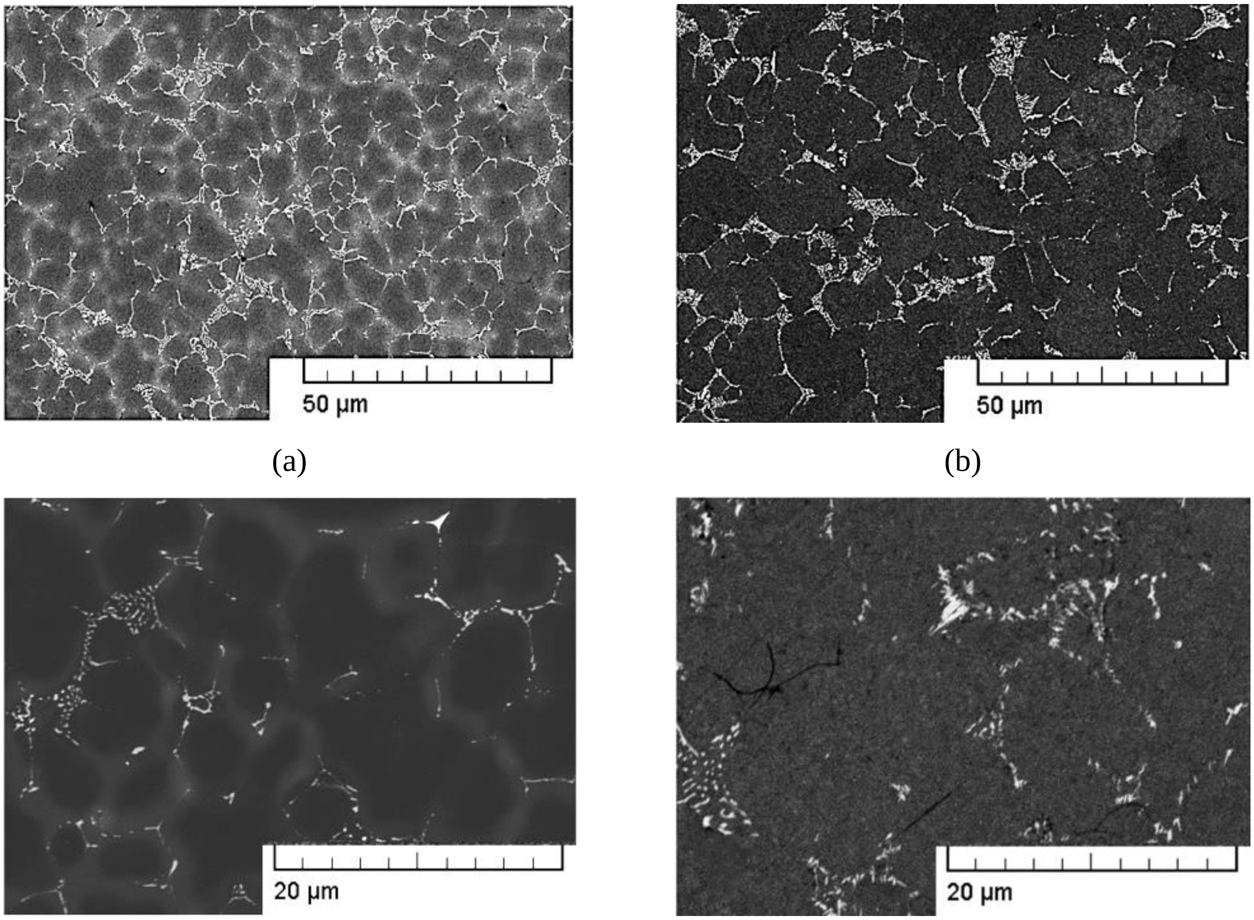

(a) (b)

(c) (d)

Figure 5-16: Cross-section microstructure of (a) and (c) as-cast, (b) and (d) T4-solutionized samples, incubation time: 2 hours.

5.3.1 Phase Identification

Phase identification was done with an EDX detector in the SEM. Table 3-3 presented the types and morphologies of all possible Al-Fe intermetallics phases in the alloy. Table 5-3 shows the minor intermetallic phases, σ-Mg(Zn,Al)$_2$ and Mg_2Si, that can be present in the alloy and their morphologies. It can be seen from the cross-section images in Figure 5-16, that these phases only represent a very small fraction of the microstructure.

σ-Mg(Zn,Al)$_2$ is a metastable phase that precipitates during non-equilibrium solidification conditions. It appears along the grain boundaries of the primary Al grains. Its morphology is rounded, with some branching. The centre of the phase contains small, circular "pockets" of Al-Mg, surrounded by Zn-Mg on the outside. σ-Mg(Zn,Al)$_2$ was not found to decrease the mechanical properties of the alloy, since it would be dissolved during the solution heat treatment.

Silicon contamination is very common in aluminum master alloys. They can also exist in casting equipment such as crucibles and die tools, if they are not properly cleaned. Mg_2Si is an unfavourable phase that forms during solidification when the local composition of the alloy exceeds 0.05wt%. During non-equilibrium solidification, the solid that is last to solidify will have a high amount of solutes due to the limited solute diffusion in the liquid (caused by fast solidification rates). Mg_2Si usually forms in two morphologies, the dendritic-like primary phase (in Table 5-3), and the Chinese script-like eutectic phase, which forms in alloys with high Si-content [71]. Both of these phases are brittle and are detrimental to mechanical properties by act as crack-initiation, or cleavage sites during uniaxial tensile tests.

Table 5-3: The morphologies and descriptions of minor intermetallic phases that are in the Al-Zn-Mg-Fe alloy.

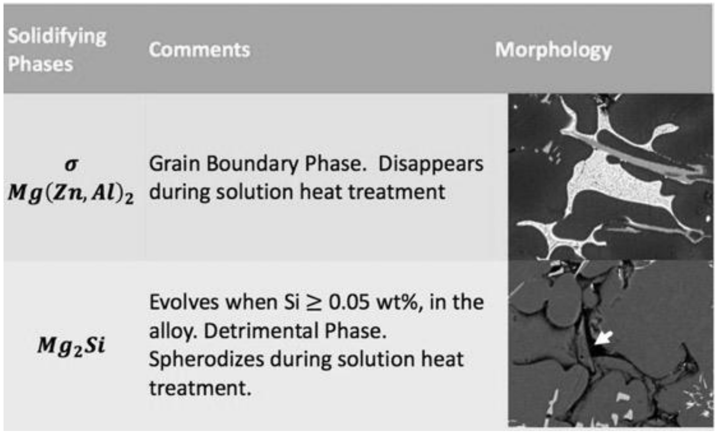

Solidifying Phases	Comments	Morphology
σ $Mg(Zn,Al)_2$	Grain Boundary Phase. Disappears during solution heat treatment	
Mg_2Si	Evolves when Si ≥ 0.05 wt%, in the alloy. Detrimental Phase. Spherodizes during solution heat treatment.	

Phase identification of the secondary phases in the alloy was completed using the SEM with EDX. Figure 5-17 shows the locations and the morphologies of the phases identified, quantified, and listed in Table 5-4.

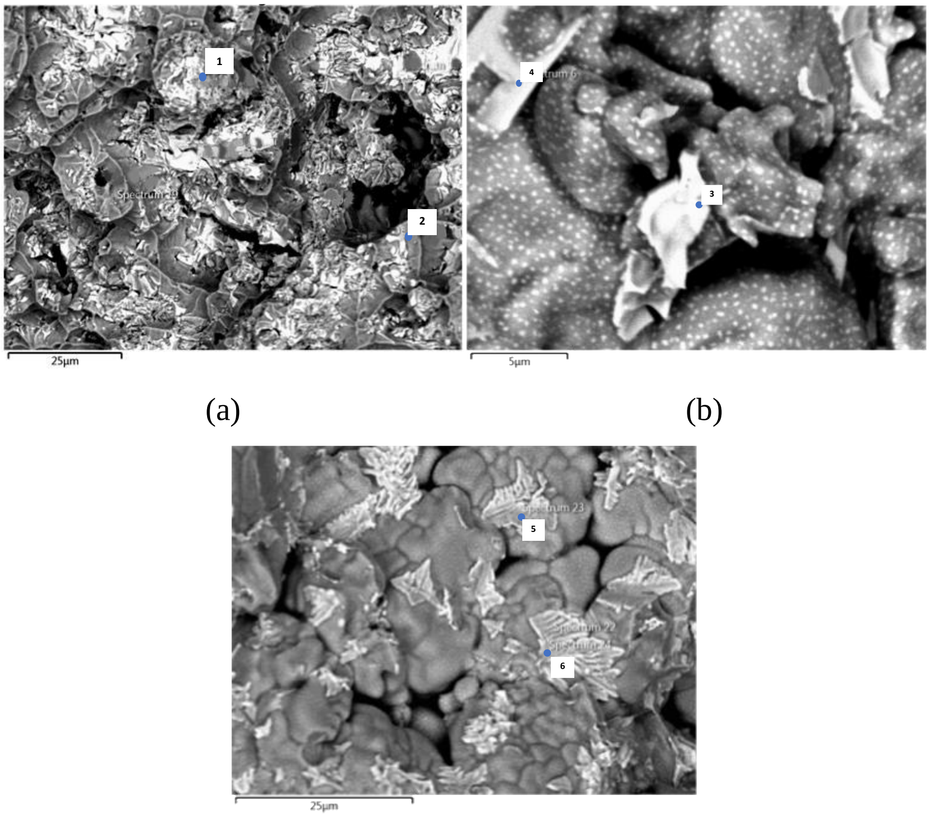

(a) (b)

(c)

Figure 5-17: Locations of secondary phases used in the SEM phase identification, values of chemical compositions are listed in Table 5-4.

Table 5-4: The chemical compositions of secondary phases in the Al-4Zn-1Mg-1.2Fe-0.1Ti alloy.

Locations in Figure 5-17	**Elements wt% (at%)**				**Speculated Phases**
	Al	**Zn**	**Mg**	**Fe**	
1	39.6(51.6)	43.1(23.3)	17.3(25.1)	-	σ-Mg(Al,Zn)$_2$
2	50.6(61.6)	33.3(16.7)	16.1(21.7)	-	σ-Mg(Al,Zn)$_2$
3	60.7(76.2)	-	-	39.3(23.8)	$Al_{13}Fe_4$
4	59.7(75.4)	-	-	40.1(24.6)	$Al_{13}Fe_4$
5	69.8(82.2)	-	-	31.2(17.8)	$A_{lm}Fe$
6	71.6(83.9)	-	-	28.4(16.1)	Al_mFe or Al_6Fe

5.3.2 Phase Fraction Analysis

The phase fraction of each of the secondary phases in the Al-Zn-Mg-Fe-Ti alloy was determined after each of the heat treatment times (Section 4.2) and compared with the simulated results obtained from Pandat using the Scheil-Gulliver paradigm. Table 5-5 and Figure 5-18 show the results of the quantitative phase analyses. Notably, due to the composition of the alloy and the high cooling rates of solidification in the HVHPDC process, the Mg2Si, $Al_{13}Fe_4$, and σ-$Mg(Zn,Al)_2$ phases in the microstructure are quite negligible. Additionally, Mg_2Si was only found in the microstructure of the 5-hour solutionized sample, thus proving the the Si-content in the alloy was fairly acceptable. $Al_{13}Fe_4$ was not found in any of the microstructural images; Al_mFe and Al_6Fe were observed, instead; mainly due to the fast solidification of the alloy during casting. The calculated phase fraction for Al_mFe and Al_6Fe was larger than the simulated $Al_{13}Fe_4$, most likely due to the difference in morphology ($Al_{13}Fe_4$ is more compact, needle-shape, whereas Al_mFe and Al_6Fe is thinner and more fibrous), and the lower Fe content in the stoichiometry of the $Al_{13}Fe_4$ phase.

Table 5-5: The average phase fraction of the secondary phases in the Al-4Zn-1Mg-1.2Fe-0.1Ti alloy, calculated at every solutionizing time, compared to the simulated results obtained from Pandat.

	$Al_{13}Fe_4$ (area %)	σ-$Mg(Al,Zn)_2$ (area %)	Mg_2Si (area %)
Simulation	2.42	-	-

Solution Time (h) (Experiments)	Al_mFe/Al_6Fe (area %)	σ-$Mg(Al,Zn)_2$ (area %)	Mg_2Si (area %)
F	3.32±0.41	0.06±0.03	-
0.25	2.84±0.21	0.21±0.1	-
0.5	2.63±0.32	0.02±0.01	-
0.75	2.90±0.34	0.20±0.04	-
1	2.71±0.39	0.00	-
1.25	2.78±0.18	0.07±0.03	-
1.5	2.96±0.44	0.21±0.11	-
1.75	2.85±0.29	0.13±0.07	-
2	2.80±0.38	0.16±0.09	-
3	2.26±0.15	0.35±0.10	-
4	2.95±0.72	0.18±0.12	-
5	2.73±0.34	0.18±0.12	0.41±0.29
6	2.62±0.67	0.17±0.06	-
7	2.31±0.51	0.33±0.17	-
8	2.79±0.81	0.24±0.02	-
9	2.70±0.89	0.27±0.05	-
10	2.63±0.17	0.47±0.16	-

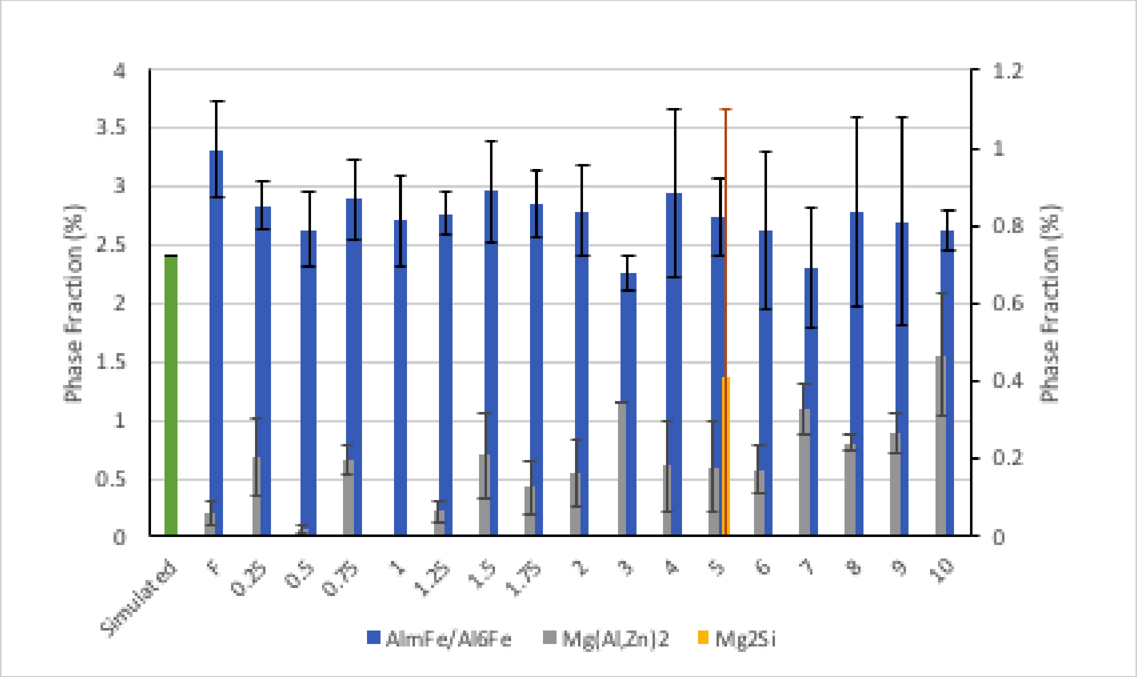

Figure 5-18: The phase fraction of every secondary phase present in the Al-4Zn-1Mg-1.2Fe-0.1Ti alloy, based on Table 5-5.

5.3.3 Grain Size

The average grain size of the alloy was determined in accordance to the ASTM E112-17 (lineal intercept method) using the image processing software, ImageJ[**]. A comparison between the grain size in the as-cast and solutionized T4 tempers was carried out; the values are listed in Table 5-6 and a visual comparison in Figure **5-19**. It is evident that there was no apparent grain growth (ripening) during the solution heat treatment. Despite the presence of PSGs, the average grain sizes were consistent because the number of grains that solidified in the die was orders of magnitude more than the PSGs (solidified in the shot sleeve and during melt injection into the die), as shown in Figure 5-16 (b) and (a), respectively; hence, the influence of PSGs on the mechanical properties was anticipated to be minimal.

[**] Image J: image processing and Analysis in Java, 1.42q Java 1.6.0 (64 bit)

Table 5-6: Average grain size of F and T4 tempers. The solutionizing time selected for the T4 temper are 2 hours (short solution time), 5 hours (medium solution time), and 10 hours (long solution time).

Average Grain Size (μm)	As-cast		T4 2 hours		T4 5 hours		T4 10 hours	
	11.7	(±1.3)	10.9	(±2.0)	12.5	(±1.0)	11.8	(±1.5)

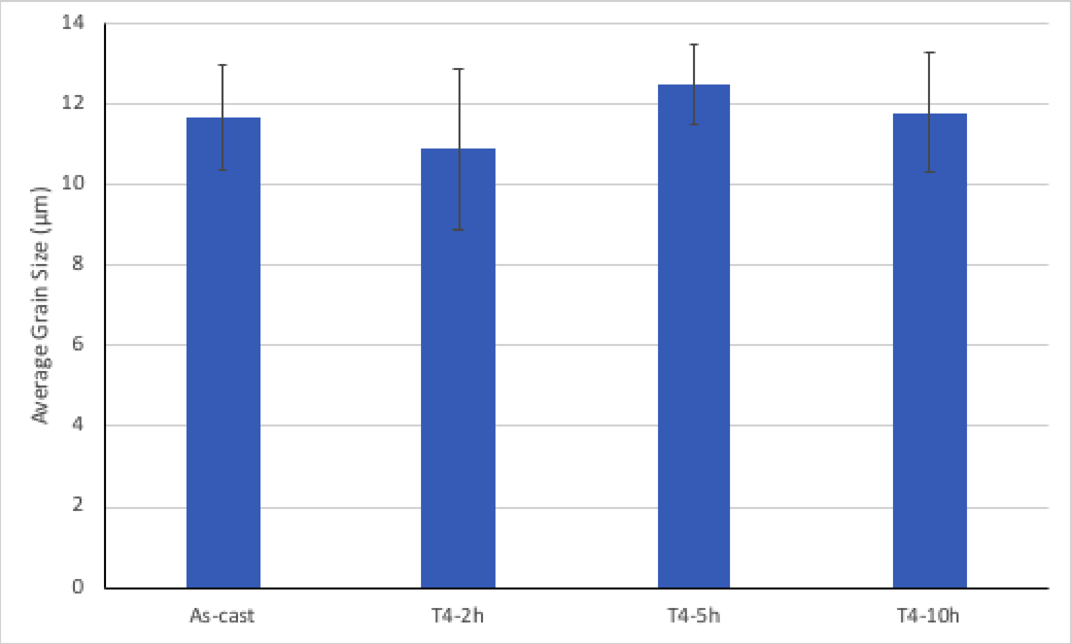

Figure 5-19: The bar graph of the average grain sizes of the Al-Zn-Mg-Fe alloy compared between F- and T4-tempers, values listed in Table 5-6**.**

The grain size distribution was also quantified using ImageJ to determine the approximate percentage of PSGs in the alloy as shown in Figure 5-20. Since the grains were mostly equiaxed in shape, they were assumed to be spherical for the evaluation of the grain size: Effective Circular Diameter (ECD). It is evident that a majority of the grains present in the microstructure consisted of grains that solidified inside the die, after filling; notably, 88% of the grains were less than 15 μm in ECD. Furthermore, PSGs (grain diameter ≥ 20μm approximately) only make up for about 7.9 % of the alloy microstructure.

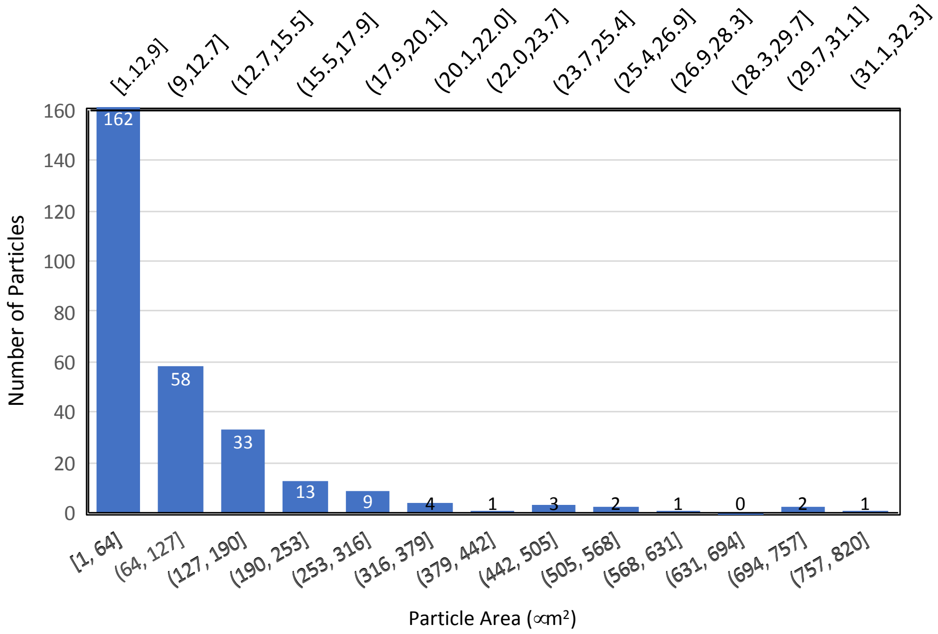

Figure 5-20: Grain size distribution in the Al-Zn-Mg-Fe alloy HVHPDC plate casting.

Table 5-7: The percentage of total grains in each bucket and their respective maximum grain diameters.

Area Bin (μm^2)	**ECD Bin (μm)**	**Percentage of Grains (%)**
[1,64]	9	56.1
(64,127]	12.7	20.1
(127,190]	15.5	11.4
(190,253]	17.9	4.5
(253,316]	20.1	3.1
(316,379]	22.0	1.4
(379,442]	23.7	0.35
(442,505]	25.4	1.03
(505,568]	26.9	0.69
(568,631]	28.3	0.35
(631,694]	-	-
(694,757]	31.1	0.69
(757,820]	32.3	0.35

5.3.4 Elemental Line Scans

Figure 5-21 shows the results obtained by the EDX line scan from the microstructure of a plate sample in the as-cast state. The white dotted lines separate the locations of the individual grains. The yellow line is the location of the line scan and the red curve shows the parabolic shaped concentration profile of elemental Al. Similarly, Figure 5-22 presents the concentration profiles of Zn and Mg, the two main diffusing species in the alloy. It is evident that both profiles follow a very similar parabolic shape, suggesting that the diffusion of both elements occur simultaneously. In Figure 5-22, the anomalous large peak in both the Zn and Mg elemental profiles were due to the σ-Mg(Al,Zn)$_2$ phase, that is circled in red in Figure 5-21. The data that make up the concentration profiles were extracted and used in the calculation for grain homogenization time during the T4 solution heat treatment.

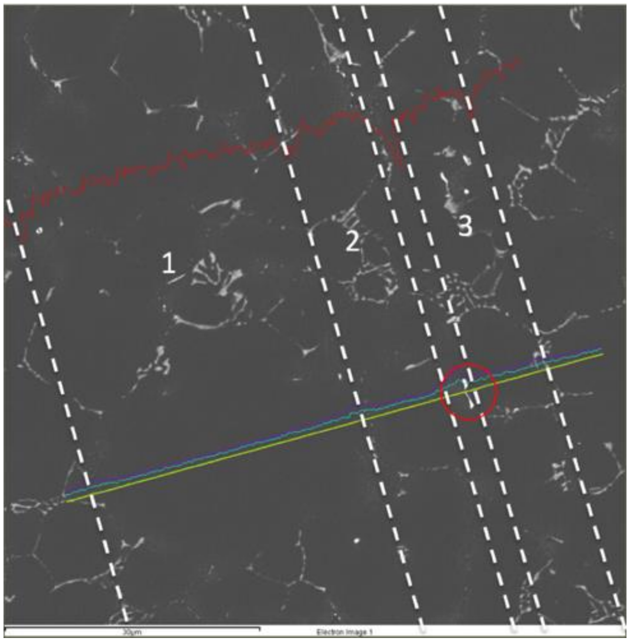

Figure 5-21: The resultant image from an EDX elemental line scan in the as-cast state, showing the location of the line scan and the concentration profiles of each element. The white dotted lines separate the locations of the individual grains, the yellow line is the location of the scan. The red circle is the σ-Mg(Al,Zn)$_2$ phase.

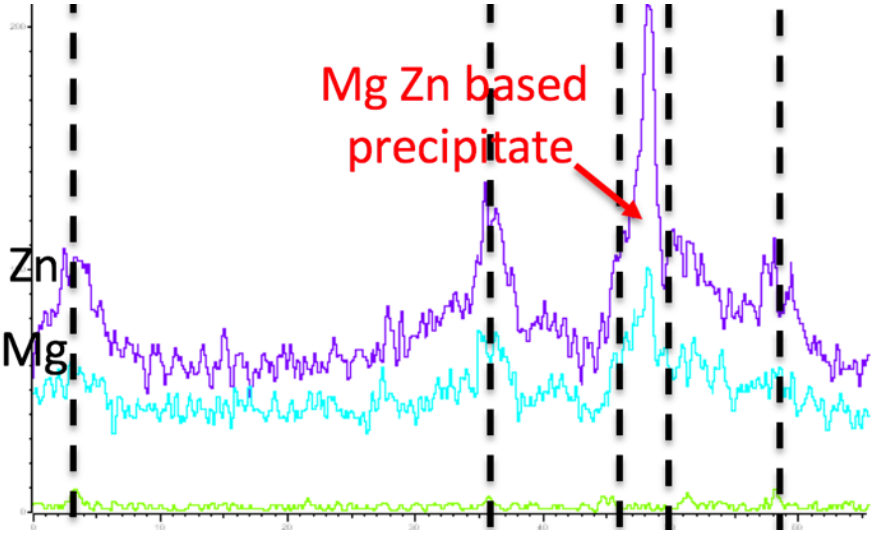

Figure 5-22: The concentration profiles of Zn and Mg in the as-cast sample, energy counts vs. distance. The anomalous peak in Zn and Mg is due to the σ-$Mg(Al,Zn)_2$ phase.

Figure 5-23 and Figure 5-24 show the EDX line scan data and corresponding concentration profile of the T4-solutionized sample with 2-hour incubation time, respectively. It is evident that no concentration gradient can be seen between the grain boundaries and the centre of the grain, showing complete homogenization by this solutionizing time. Also, the microstructural comparison in Figure 5-16 shows completely homogenized grains in the 2-hour T4 sample, compared to the grains with coring, found in the as-cast image. Therefore, it can be concluded that complete homogenization of the grains occurs in less than 2 hours of solution heat treatment. EDX line scans of heat-treated samples with incubation times of 0.25 to 1.75 hours were all completed and will be used in the homogenization model in order to predict the time for complete homogenization of solutes within the primary Al grains.

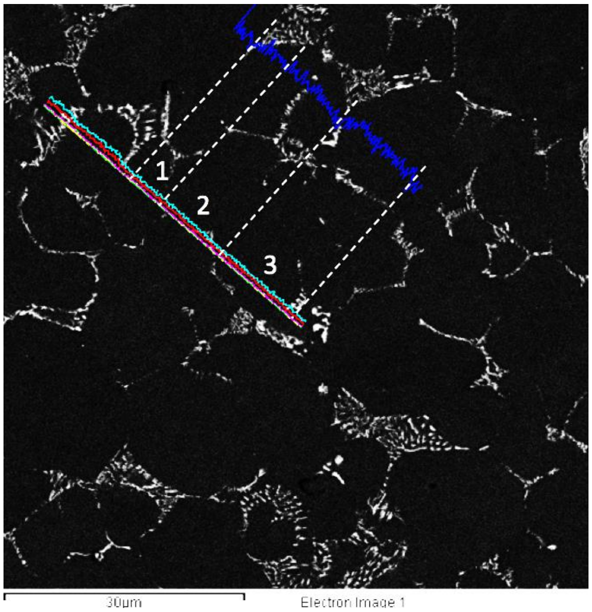

Figure 5-23: The resultant image from the EDX line scans of the T4-solutionized sample, incubation time, 2 hours. The white dotted lines show the outlines of the grains.

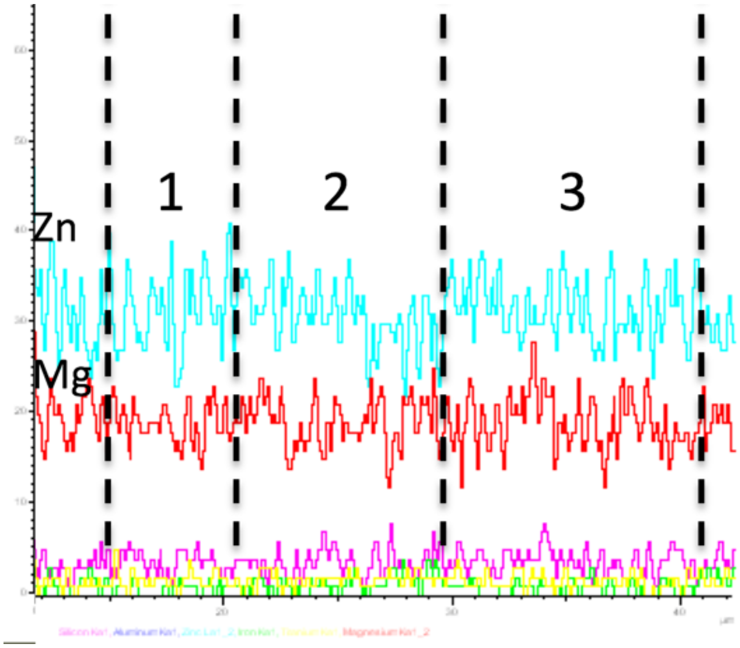

Figure 5-24: The concentration profiles of Zn and Mg of the T4-solutionized sample, showing almost no change in the concentration gradient between the edge and the centre of the grains because of complete homogenization of the solute elements.

5.4 Uniaxial Tensile Properties

Table 5-8 and Figure 5-25 show the average tensile properties with standard deviations obtained from uniaxial tensile tests from as-cast to 24-hour solution heat treatment time (5 to 6 samples in each heat treatment condition). It was noticed upon initial inspection of the fracture surfaces, in Figure 5-26(a), that the samples with clean fractures surfaces (i.e.: good mechanical properties) fractured with a nearly 45° angle with respect to the loading direction in the uniaxial tensile test, as predicted by the orientation of the Critically Resolves Shear Stress (CRSS) in an FCC structure such as Al. Alternately, the fracture surfaces with inclusions and porosities (resulting in poor tensile properties), had fractured with a jagged irregular profile, indicating that the failure was due to a combination of brittle and ductile fracture modes initiated by defects. As mentioned earlier in this thesis, in Section 5.2 on Casting Quality, the defects from uncontrollable non-optimized variables in the HVHPDC process trials in this project, arising from manual operations such as gate design, melt pouring, lubricant spray, die opening and closing, and shot initiation would lead to the introduction of one or more of the defects such as PSGs, shrinkage porosity from unfavourable die thermal management and gas porosity. These defects would have a significant effect on the results of the uniaxial tensile tests as shown by the variations in the strength and elongation in Table 5-8. Typically the presence of PSGs would only have a marginal effect on the uniaxial tensile properties (<3% of total yield strength), as shown in Section 3.5.4, while, the presence of shrinkage porosity caused by non-optimal die thermal management and/or choking of the melt flow through the gates and die cavity due to PSGs, would lower the yield strength (0.2% proof stress). The presence of gas porosity would typically affect the plastic behaviour in the tensile test and hence, lowers the UTS and elongation in the tensile test. The presence of inclusions and Mg_2Si phases would affect both the elastic and plastic regimes of the tensile test and hence, lowers UTS, YS and elongation of the sample. Table 5-8 shows that there are two general regimes of YS (around 180 MPa and around 150 MPa), that is not dependant on the time of T4 solution treatment; suggesting, that the location of the tensile test bar in the plate (Figure 4-2) may have included abnormally high shrinkage porosity causing the YS to be lower. Further, the presence of one or more of the gas porosities, inclusions or Mg_2Si phases in the tensile bar location on the plate may reduce the UTS and elongation in Table 5-8. These defects, detrimental to the uniaxial tensile properties would not represent those of the alloy cast with optimal alloy treatment and process conditions in the HVHPDC process, in a commercial environment. In other words, typically, with a completely automated and controlled HVHPDC process, the peak tensile properties could be attained within half hour (30 min) of T4 solutionizing heat treatment.

Table 5-8: Mechanical properties of the Al-Zn-Mg-Fe alloy, determined from the uniaxial tensile test.

Heat Treatment Time (h)	UTS (MPa)		YS (MPa)		El (%)	
0 (As-cast)	275	±15	136	±4	9.5	±2.4
0.25	346	±21	184	±5	13.7	±4.9
0.5	302	±21	150	±15	13.0	±1.6
0.75	350	±15	185	±8	12.7	±2.9
1	320	±22	157	±8	15.5	±3.7
1.25	342	±9	185	±3	11.3	±1.5
1.5	342	±12	184	±5	13.3	±1.6
1.75	327	±10	169	±3	13.3	±2.0
2	320	±12	156	±3	16.7	±4.4
3	290	±12	147	±1	11.3	±4.4
4	304	±12	155	±1	12.9	±5.0
5	318	±19	159	±9	16.3	±5.0
6	312	±4	154	±4	14.2	±5.0
7	292	±80	155	±54	14.5	±1.8
8	375	±7	180	±6	18.9	±2.0
9	300	±70	153	±26	12.0	±0.8
10	292	±25	147	±7	14.0	±3.2
24	294	±43	143	±18	11.4	±2.6

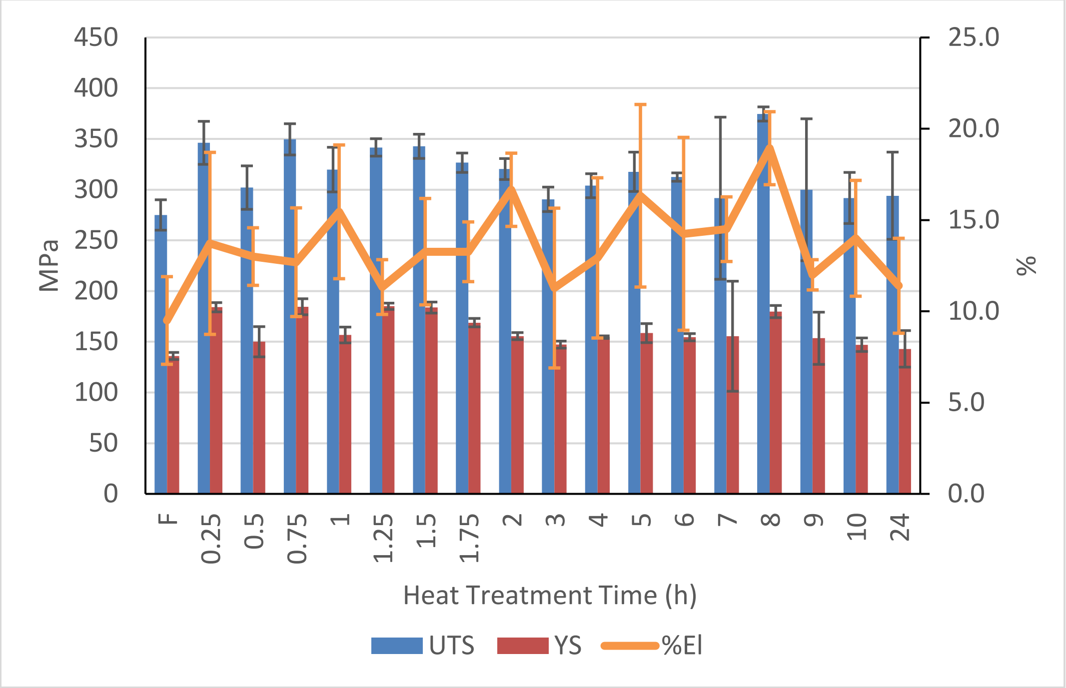

Figure 5-25: The uniaxial tensile properties of as-cast (F) and heat-treated (T4) samples of the Al-Zn-Mg-Fe alloy, from Table 5-8.

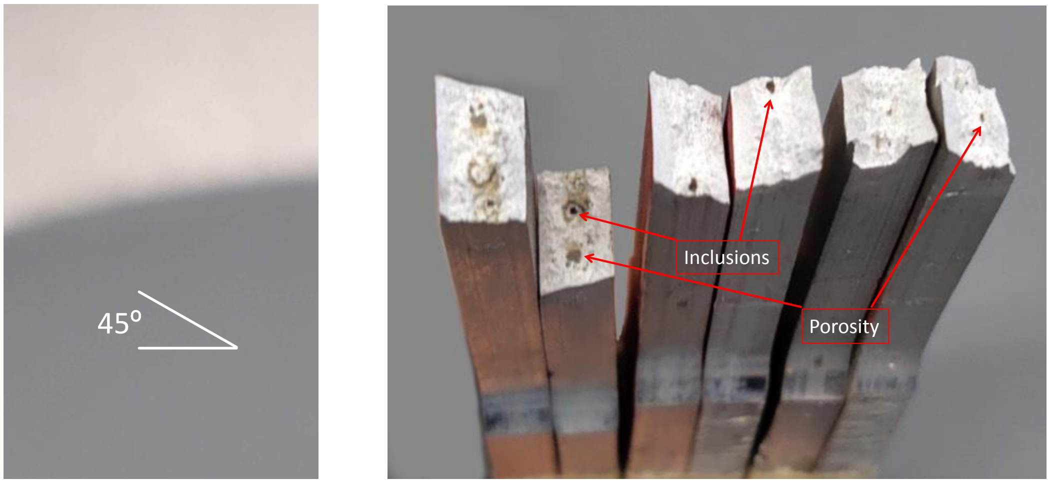

(a) (b)

Figure 5-26: Fracture surfaces of tensile bars (a) sound sample and, (b) samples with defects (porosities and inclusions).

5.4.1 *Fractography*

A detailed fracture surface analysis was done using SEM imaging and EDX techniques. Figure 5-27 shows the typical fracture surface of a tensile bar in the as-cast state with average mechanical properties. It consists of two main sections, the shear lips around the perimeter of the sample and fibrous region in the middle, indicative of a ductile fracture. The crack initiation point occurs on the bottom centre of the sample and propagates inwards. The shear lips are the locations that correspond to the maximum shear stress [26]; they are usually oriented at about 45° from loading axis in the tensile test. Significant amounts of plastic deformation can be seen in the fibrous region in the middle area. In the fibrous region, the nucleation and coalescence of microvoids occur. Shrinkage porosities are potential nucleation sites for microcracks. They can be seen in the magnified image, where they shear through the porosities that are already inside the casting.

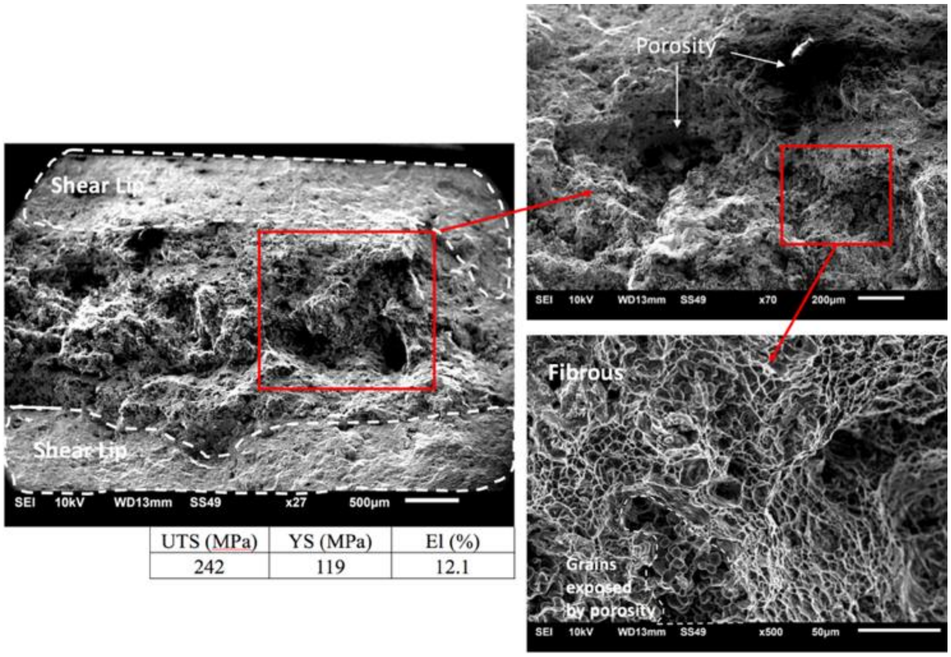

UTS (MPa)	YS (MPa)	El (%)
242	119	12.1

Figure 5-27: Fracture surface of a tensile bar in the as-cast state.

EDS mapping (Figure 5-28) shows the intermetallic phases on the fracture surface. The two main intermetallic phases that can be seen are Mg_2Si and σ-Mg(Al,Zn)$_2$. Mg_2Si, circled in yellow, was only found in very small quantities, and difficult to spot. The σ-Mg(Al,Zn)$_2$ phases, circled in red, can be seen as brittle cleavage marks in the middle of α-Al dimples. This suggests that they were most likely participants in the last stage of crack propagation. The exposed grains seen in the microstructure are due to the shearing of porosities inside the casting.

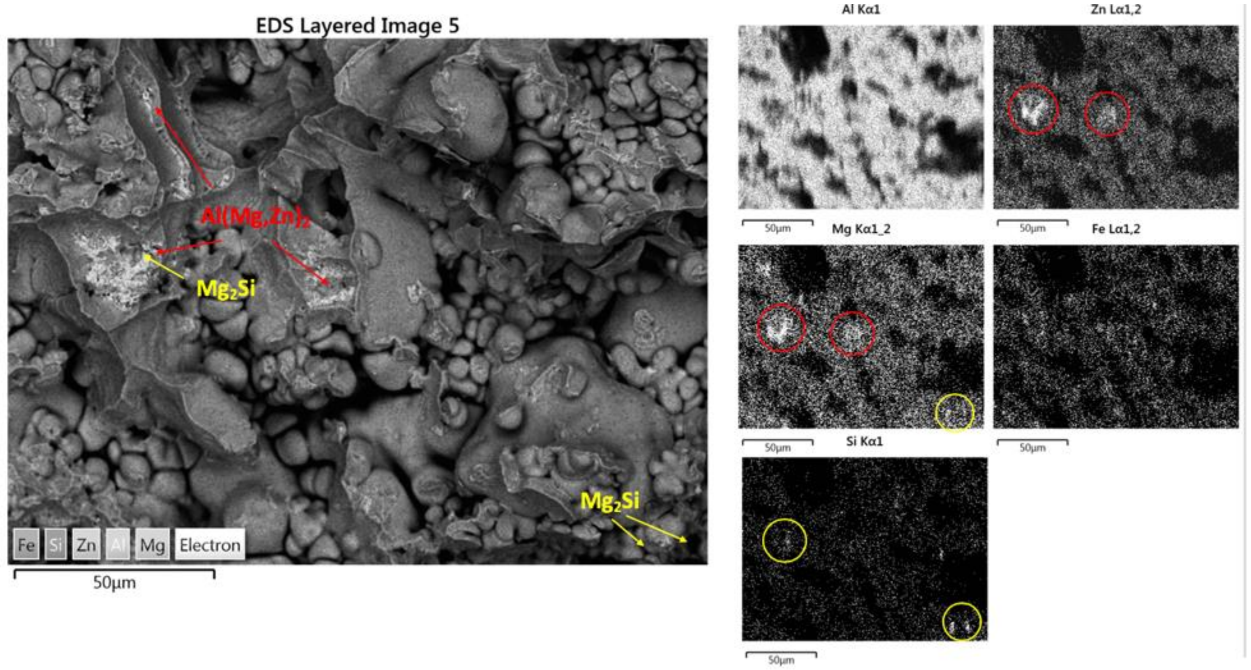

Figure 5-28: SEM map showing the intermetallic phases on the fracture surface. Mg$_2$Si is labelled in yellow and σ-Mg(Al,Zn)$_2$ is labelled in red.

5.5 *Bulk Hardness Curves*

The bulk hardness curves for the heat-treated Al-4zn-1Mg-1.2Fe-0.1Ti alloy are presented in this section. Figure 5-29 presents the bulk hardness curves in two graphs separated by the respective time for T4 solution treatment: (a) 0.25 to 2 hours, (b) 3 to 10 hours. It was hypothesized that the bulk hardness of the alloy will change as the SSSS (formed during quenching) transforms into VRCs and finally into GP-zones.

In both Figure 5-29 (a) and (b), three distinct regions can be seen in the hardness graphs. The initial region is indicated by a sharp increase in the hardness. This is thought to be the formation of the Mg self-clusters, which are formed initially due to the faster diffuion of the dissolved Mg solute in the Al matrix, than the Zn solute. The beginning of the second stage of the hardness curve is denoted by a significant change in the hardening rate. For the short solution times (0.25 to 2 h, in Figure 5-29 (a)), rate of change was calculated to be 0.11h^{-1} to 0.15h^{-1}, whereas for the longer solution times (3 to 10h, in Figure 5-29 (b)), the rate of change was $0.14h^{-1}$ to $0.2h^{-1}$. This stage was speculated to be highlighted by the joining of Zn atoms onto the Mg clusters, beginning the formation of GP-I zones. The rate of hardness change for the shorter solution times is lower due to the lower amount of VRC retained created and retained after quenching, post the T4 treatment. The second stage is prolonged for the shorter heat treatments for the same reason; causing slower mobility of the Zn atoms in the Al matrix. In the third stage, the hardness is stabilized as the GP-I zones form and stabilize. Once hardness reaches stability, tensile tests were performed on the samples, as shown in the Figure 5-29 (a) and (b).

The hardness is speculated to be higher in this alloy due to the penetration depth of the hardness indenter, which is approximately 20μm to 100μm (for hardness ranges from 80-120, which are typical hardness values for this alloy), as shown in Equation 5-1.

Equation 5-1

$$\boldsymbol{HR = N - \frac{d}{s}}$$

where N and s are geometric constants based on the scale of the hardness test, and d is the penetration depth from zero load. Since the typical skin thickness for this casting is approximately 250μm, it is reasonable to assume the hardness measured for this alloy was that of the skin area. The grain size within the skin area is very fine; therefore, it will result in a significantly higher hardness value.

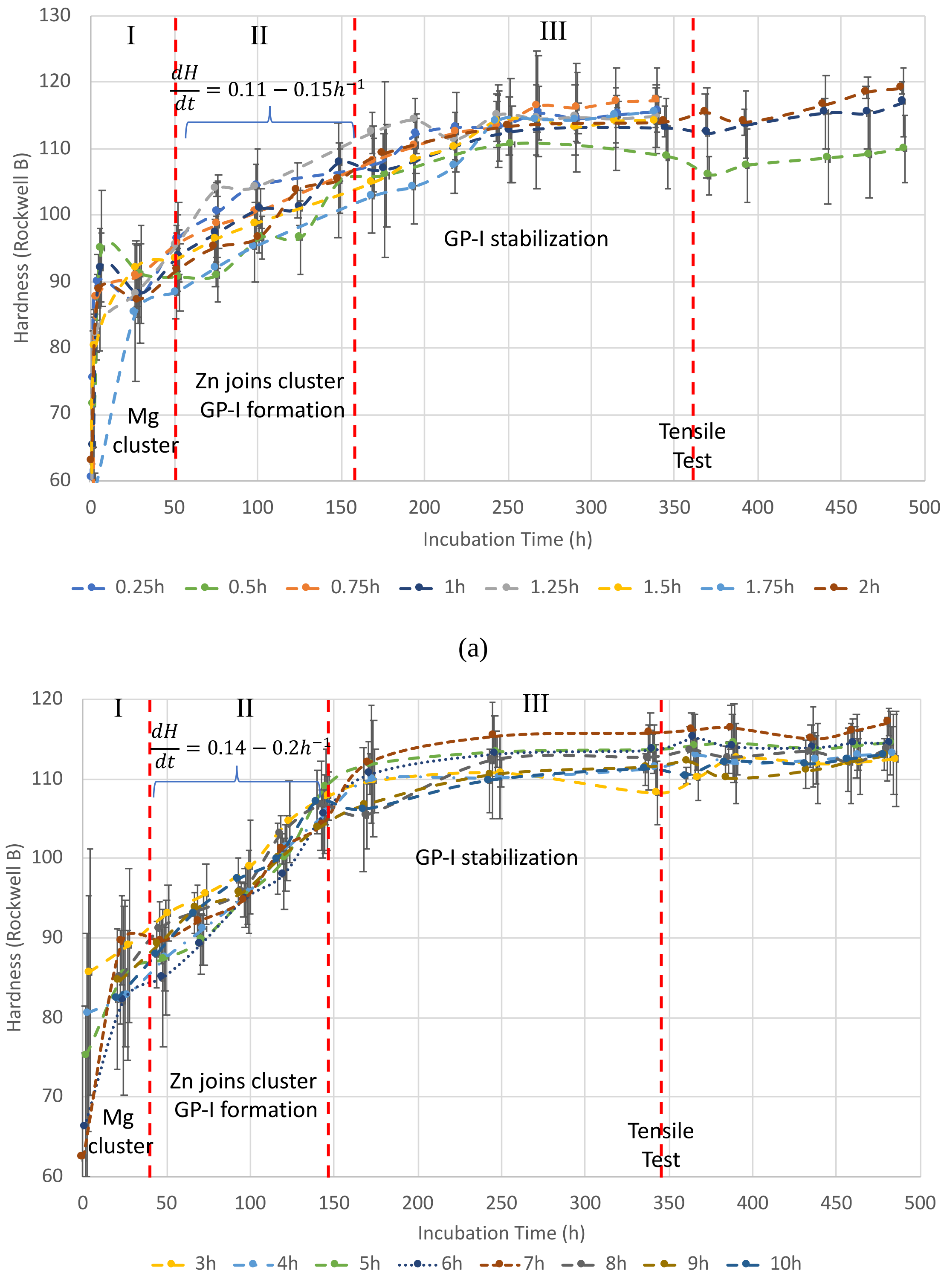

(a)

(b)

Figure 5-29: The bulk hardness curves for the following incubation times (a) 0.25-2 hours (b) 3-10 hours.

5.6 Homogenization Model

The homogenization model was used to determine the solution heat treatment time needed for homogenization of the diffusing species, Zn and Mg solutes, within the primary Al grains. In the as-cast state, there is solute segregation (coring), which can be seen in the EDX line scan in Figure 5-22, as well as the coring effects from the as-cast microstructure in Figure 5-16 (a). As the metal is heat treated, the rate of diffusion increases, and eventually solute segregation is eliminated (Figure 5-16 (b)). Since the grains in the casting microstructure is nearly equiaxed shape (see Section 5.3.3), it was reasonable to assume them as spherical. Therefore, the homogenization model can be simplified into a one-dimensional diffusion equation (Fick's second law) with a spherical coordinate geometry. Additionally, the solutes were regarded to be diffusing independently from each other (no interaction between Zn and Mg in the Al matrix during diffusion). The impact of the assumption of the lack of interaction between Zn and Mg would be verified by comparing the simulation of the model with experiment results.

For this project, the electron counts profile obtained from EDX line scans were regarded as a measure for the concentration of solutes. From Section 5.3.4, it is evident that separate concentration profiles can be obtained for zinc and magnesium. Initially, the profiles were visually divided into individual grains, and each grain is then divided into two half-grain sections, domain symmetry. Figure 5-30 presents a schematic of a concentration profile of a half-grain, where the c_0 represents the initial concentration in the middle of the grain and c_r represents the initial concentration at radius R.

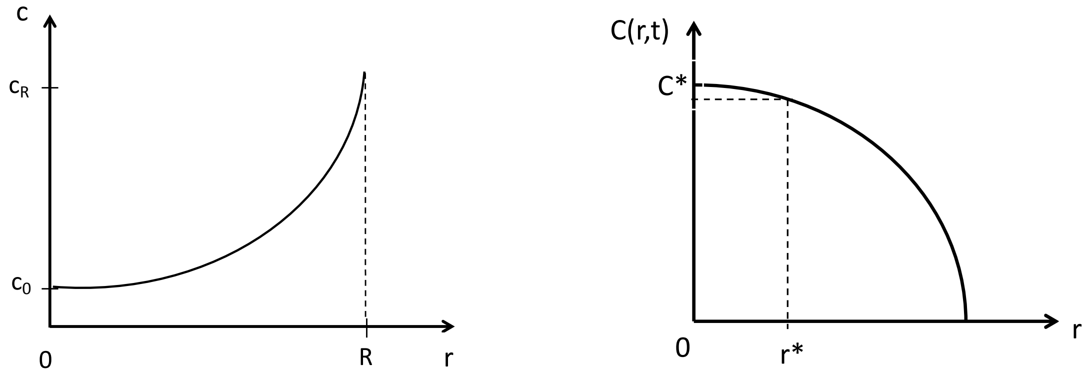

(a) (b)

Figure 5-30: The schematic of a half-grain concentration profile. (a) measured energy counts from EDX and (b) dimensionless concentration profile as a function of grain radius. The subscript *o* represents the initial concentration in the middle of the grain and subscript *R* represents the initial concentration at radius R.

The concentration is then made dimensionless using the equation:

Equation 5-2

$$\mathbf{C}(\boldsymbol{r},\boldsymbol{t}) = \frac{\boldsymbol{c}-\boldsymbol{c_R}}{\boldsymbol{c_o}-\boldsymbol{c_R}}$$

The general diffusion equation without a source term is given by Equation 5-3. Figure 5-18 shows that there is no discernible dissolution of the σ- Mg[Al,Zn]$_2$ phase during T4 solution heat treatment; hence, there would not be a source term for the Zn and Mg solutes from the grain boundary from these phases.

Equation 5-3

$$\frac{\partial \boldsymbol{C}}{\partial \boldsymbol{t}} = \frac{\boldsymbol{D}}{\boldsymbol{r}^2}\frac{\partial}{\partial \boldsymbol{r}}\left[\boldsymbol{r}^2\left(\frac{\partial \boldsymbol{C}}{\partial \boldsymbol{r}}\right)\right]$$

The initial condition is:

Equation 5-4

$$\boldsymbol{C}(\boldsymbol{r},\mathbf{0}) = \boldsymbol{f}(\boldsymbol{r})$$

The two boundary conditions are:

Equation 5-5 $\frac{\partial C}{\partial r}(0,t) = 0$ and $C(R,t) = 0$

Since the Equation 5-3 and Equation 5-5 are homogenous and linear, the separation of variables could be adopted for solution, as shown below:

Equation 5-6 $C(r,t) = \phi(r)\theta(t)$

By substituting Equation 5-6 in Equation 5-3, we get:

Equation 5-7 $\phi\dot{\theta} = \frac{D}{r^2}\frac{\partial}{\partial r}(r^2\theta\phi') = \frac{D}{r^2}(2r\phi' + r^2\phi'')$

Isolating the variables, results in:

Equation 5-8 $\frac{\dot{\theta}}{D\theta} = \frac{r^2\phi''+2r\phi'}{\phi r^2} = \gamma; \text{where } \gamma < 0 \text{ or } \gamma = -\omega^2$

In Equation 5-8, there are no solutions for $\gamma \geq 0$. Further, Equation 5-8 could be divided into two ordinary differential equations (ODEs), as below:

Equation 5-9 $r^2\phi'' + 2r\phi' - \omega^2 r^2\phi = 0$, and

Equation 5-10 $\theta + \omega^2\dot{D}\theta = 0$

The general solution for Equation 5-9 is given in Equation 5-11.

Equation 5-11 $\phi(r) = \frac{A\sin(\overline{\omega r})}{r} + \frac{B\cos(\overline{\omega r})}{r}$

In Equation 5-11, A and B are constants.

A check was performed to validate that Equation 5-11 is the general solution for the Equation 5-9. The expressions for $\phi'(r)$ and $\phi''(r)$ were obtained by differentiation of Equation 5-11 with respect to r and substituting in Equation 5-9 provided the required validation. By implementing the boundary condition, ϕ'(0)=0, the constant B must equal 0 to satisfy the Equation 5-11 and generate a finite number of solutions at r=0. Therefore, the final solution is refined as below:

Equation 5-12 $\phi(r) = \frac{A\sin(\omega r)}{r}$

The general solution for Equation 5-10 is:

Equation 5-13 $\boldsymbol{\theta(t) = Ce^{-\omega^2 Dt}}$

In Equation 5-13, C is a constant. The combined final solution for C(r,t) in Equation (8) is:

Equation 5-14 $\boldsymbol{C(r,t) = \phi(r)\theta(t) = A\frac{\sin(\omega r)}{r}e^{-\omega^2 Dt}}$

Applying the boundary condition for C(R,t)=0 Equation 5-14, we get,

Equation 5-15 $\boldsymbol{C(R,t) = A\frac{\sin(\omega R)}{R}e^{-\omega^2 Dt} = 0}$

In Equation 5-15, since only $\sin(\varpi R)=0$, the variable ϖ will have an infinitely many eigenvalues, such that:

Equation 5-16 $\boldsymbol{\omega_n = \frac{n\pi}{R} \quad for\ n = 1, 2, 3 \ldots\ldots \infty}$

For each eigenvalue of ϖ, there is a unique solution for C(r,t), and all these unique solutions could be superimposed as a summation to form a general solution for C(r,t) in Equation 5-3. The general solution becomes a sum of all of the eigenvalue solutions with a unique constant, A_n:

Equation 5-17 $\boldsymbol{C_n(r,t) = \sum_{n=1}^{\infty}\left[A_n\frac{\sin(\omega_n r)}{r}e^{-\omega_n^2 Dt}\right]}$

The constant A_n can be evaluated using the initial condition C(r,0) = f(r) (Equation 5-4) and using the orthogonality of $\frac{1}{r}sin\left(\frac{n\pi r}{R}\right)$, such that,

Equation 5-18 $\boldsymbol{A_n = \frac{2}{R}\int_0^R\{r \cdot f(r) \cdot \sin(\omega_n r)\}dr}$

Equation 5-16, Equation 5-17 and Equation 5-18, combined, present the general solution for evaluating C(r,t) in Equation 5-3.

5.6.1 EDX Line Scan Analysis

The raw data obtained from an EDX line scan for the concentration profiles of the Zn and Mg solutes were plotted, typically as shown in Figure 5-31. The outline of the grain can be seen in between the two small green lines, pointed out with the yellow arrow. Polynomial curves were fitted for Zn and Mg (typically 2nd order) and the equation for Zn is displayed on Figure 5-31 (b). Since the homogenization model uses the half-grain curve, so half of the fitted curve was used. The concentration values obtained from the fitted curve were made dimensionless using Equation (1) and plotted. Figure 5-31 (c) shows the plotted results. The equation of the dimensionless concentration profile was used as the equation f(r) in Equation (20) for calculating A_n.

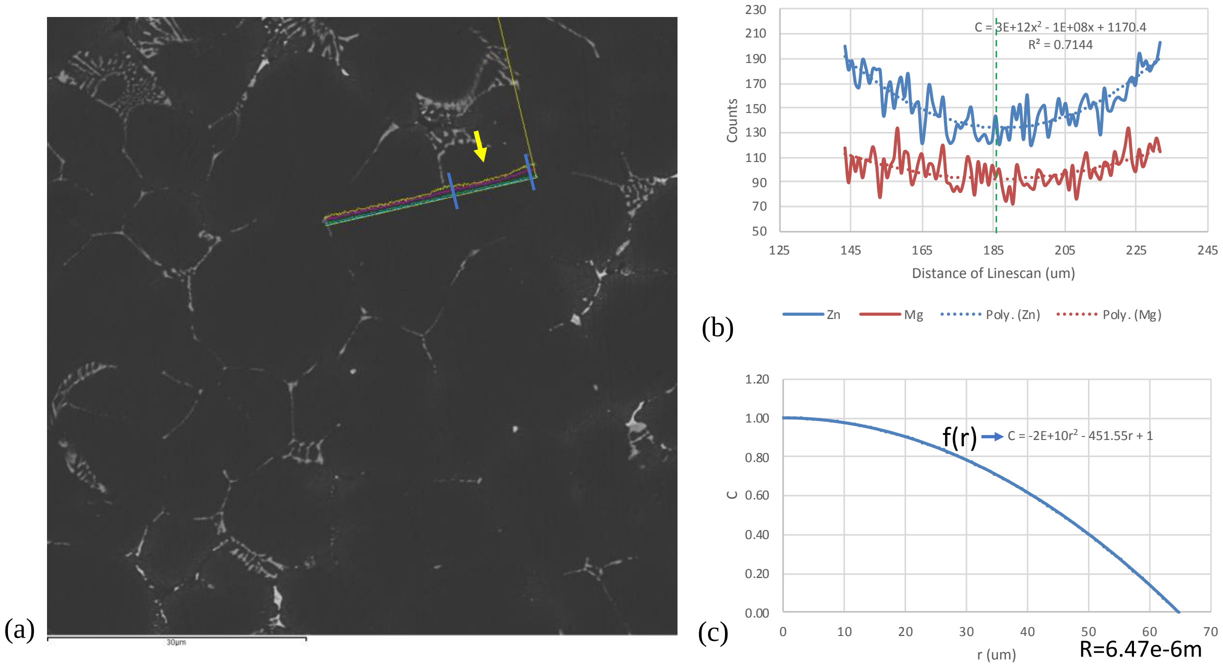

Figure 5-31: The concentration profile (counts vs. distance) of Zn and Mg in an as-cast sample, (a) original EDX line scan image, the blue lines show the selected grain, (b) the initial profiles with the fitted polynomial curve and equation, and displayed R^2 value; half-grain selected for analysis, is denoted, (c) the dimensionless half-grain concentration profile of Zn obtained from the fitted curve, evaluated by Equation 5-2; the radius of this particular grain is 6.47×10^{-6} m.

Figure 5-32 presents the concentration profiles for Zn and Mg as a function of dimensionless distance at different incubation times at T4 treatment temperature, respectively. An initial observation suggests that homogenization is achieved within 2 hours for both Zn and Mg solutes, independently.

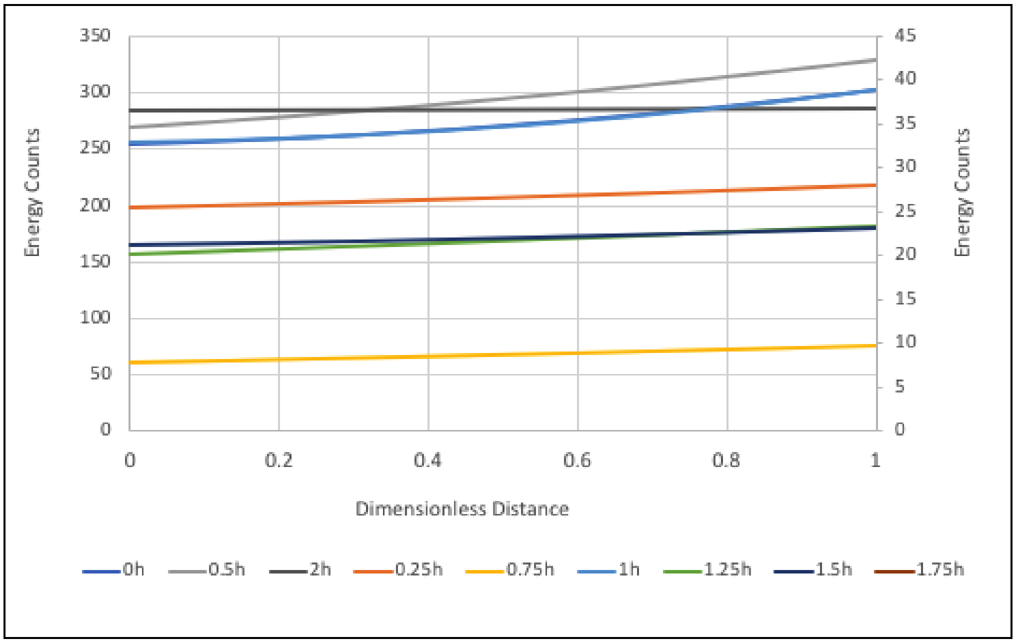

(a)

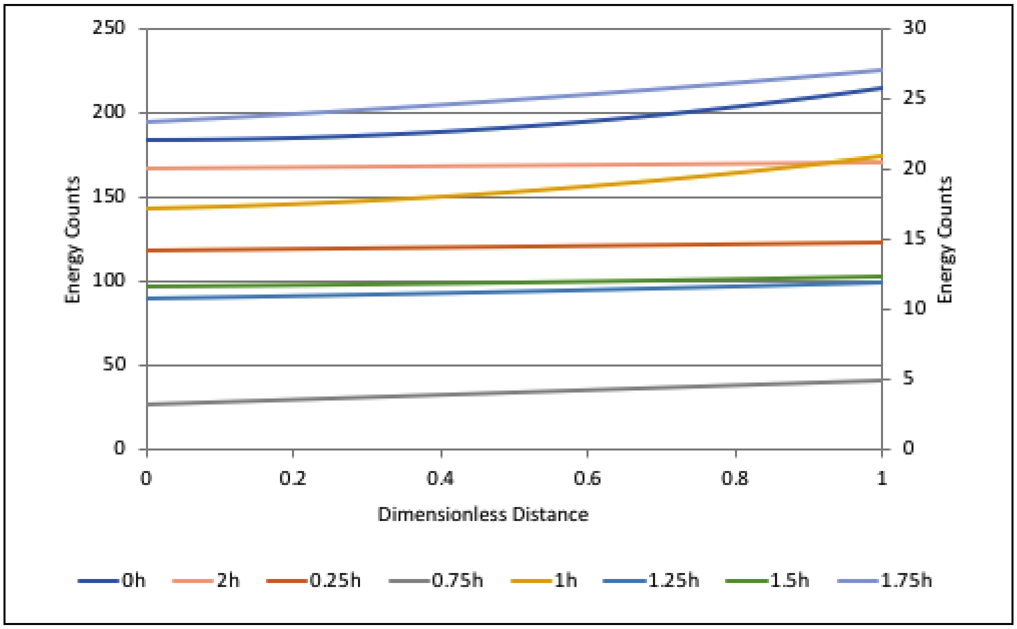

(b)

Figure 5-32: Fitted curves for concentration as a function of solutionizing treatment times for (a) Zn (b) Mg.

5.6.2 Numerical Solution - MATLAB Simulation

A MATLAB code was written to determine the analytical solution of this homogenization model, as shown in Equation 5-16, Equation 5-17 and Equation 5-18, combined. The input data for the code is as follows:

- A matrix containing the grain radius, in metres, and the concentration of the diffusing species (Zn and Mg separately), calculated from the fitted curve.
- The corresponding heat treatment time, in seconds.
- The diffusion constant for Zn and Mg in solid Al, determined separately, calculated at 475°C, as obtained from background literature.

The values for concentration were automatically converted to dimensionless form. The outputs of the code are given by two graphs, dimensionless C vs. time and C vs. r. The homogenization time can then be determined using the dimensionless C vs time for a specific grain size.

5.6.3 Comparison with Experimental Results

The time for complete solute homogenization within the Al grains was the time taken for C(r,t)=0.005. It is evident that larger grains would have a longer homogenization time compared to smaller grains; therefore, it is important to have experimental data from grains of varying sizes. A total of 5 grains, ranging from 5.12 to11.36 μm in diameter, in the as-cast condition was used as the input data for both Zn and Mg, separately. Notably, none of the PSGs were considered for the homogenization model because of two reasons: firstly, they constituted less than 8 area % of the microstructure and a typical controlled HVHPDC commercial process would mitigate the formation of PSGs.

In order to establish a verifiable comparison with the experimental results, it was critical to identify valid diffusion coefficient for each of Zn and Mg in solid Al matrix. Diffusion constants, outlined in Table 5-9, were obtained from different sources in the background literature and calculated using the following Arrhenius type equation, at T=475°C.

Equation 5-19

$$\boldsymbol{D = D_0 \exp\left(\frac{-Q}{RT}\right)}$$

All of constants were tested using the MATLAB code in combination with the line scan data from both the as-cast and heat-treated of similar-sized grain, alike. Table 5-9 shows a list of all of the diffusion constants obtained from the relevant background literature information. All the diffusion equations were tested with the MATLAB code and verified with the experiment results from this project.

Table 5-9: Diffusion coefficient values for Zn and Mg, in solid Al matrix, obtained from literature.

Reference	**D_o (cm^2/s)**	**Q (kJ/mol)**	**$D_{Zn}^{475°C}$ (m^2/s)**	**Reference**	**D_o (cm^2/s)**	**Q (kJ/mol)**	**$D_{Mg}^{475°C}$ (m^2/s)**
[85]	0.1	125.5	6.10e-15	[28]	1.2	131.0	8.56e-13
[86]	0.3	121.4	1.02e-12	[87]	6.23	114.8	3.81e-14
[88]	1.1	129.4	9.65e-13	[26]	0.6	125.0	5.27e-14
[89]	0.2	120.6	8.22e-14				
[90]	0.17	118	7.05e-14				

5.6.3.1 Diffusion of Zinc

In order to determine the correct diffusion constant to use in the model, the results from MATLAB, using an average-sized, as-cast grain as the input and the diffusion coefficients for Zn in Table 5-9 were simulated. The 0.25h data was selected, and the calculated results were compared to the experimental results obtained from EDX line scans of the sample after 0.25h solution time. The experimental data was converted into dimensionless radius and concentration and plotted with the calculated data in Figure 5-33 for two values of D_{Zn}^{Al}; it is evident that the curve corresponding to the diffusion coefficient, $D_{Zn}^{Al} = 6.1 \times 10^{-15}\ m^2/_s$ was the closest to mimic the experiment conditions of homogenization. There are several factors that would contribute to the observed deviations between experiment and simulation in Figure 5-33, some of the salient ones would include:

- The accuracy of the energy data obtained from the elemental line scan due to the interference of the interaction volume of the incident X-Ray beam on the sample (refer to Section 4.6.1),
- The amount of retained vacancies after quenching the sample from the solutionizing temperature of 475 °C has a significant impact on the diffusion of solute in the matrix.
- Diffusion coefficient is dependent on the composition of the diffusing species in the matrix and only constant values of D_{Zn}^{Al} and D_{Mg}^{Al}, respectively, was used in this study as the variable data was unavailable in the literature.
- Validity of the assumption that there is no interaction between Mg and Zn in their respective mobility in primary Al matrix.
- Empirical fitting of the experiment elemental line scan data along with the respective standard errors.

The optimum number of summation terms in Equation 5-16, Equation 5-17 and Equation 5-18, were evaluated and it was determined that 25 terms were sufficient to present a valid result; Figure 5-34 shows the comparison of using 100, 50 and 25 terms in the summation, on the concentration profile after 0.25 h of homogenization simulation, showing no discernable difference among the three curves. Hence, 25 terms were used in the summation for all the simulations in this work.

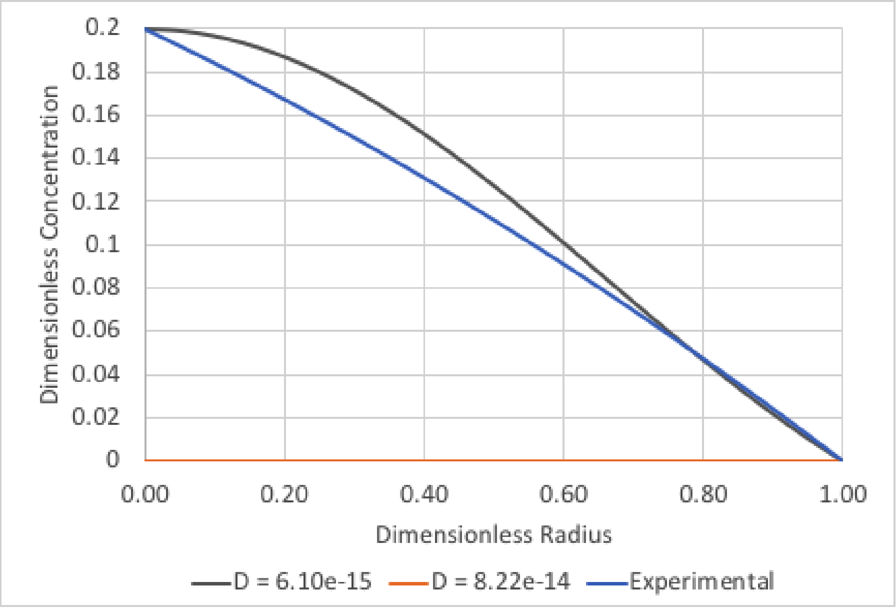

Figure 5-33: The comparison between the theoretical concentration curves at 0.25h solutionizing time for Zn, calculated using the diffusion constants found in Table 5-9 with the concentration profile obtained from EDX line scans.

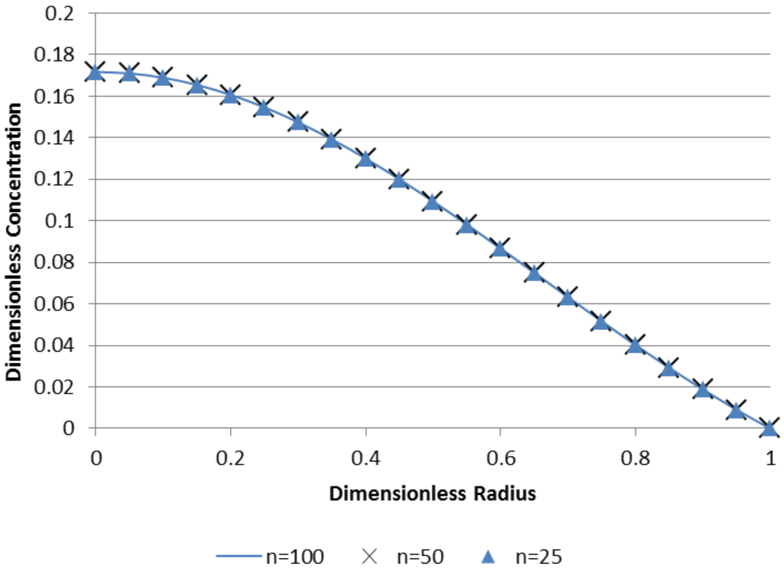

Figure 5-34: Comparison *C* versus *r* after 0.25 h of diffusion simulation, using 100, 50 and 25 terms for the series summation in Equation 5-16, Equation 5-17 and Equation 5-18; the use of 25 terms would suffice for valid results in the simulation.

Figure 5-35 shows the resultant graphs for dimensionless concentration vs. solutionizing time of Zn. The input data used was the concentration curve obtained in the as-cast condition of an average sized grain (grain size = 11.2μm) using the diffusion coefficient D = 6.10e-15 m^2/s. The homogenization time for Zn is predicted to be approximately 2700s or 0.75h.

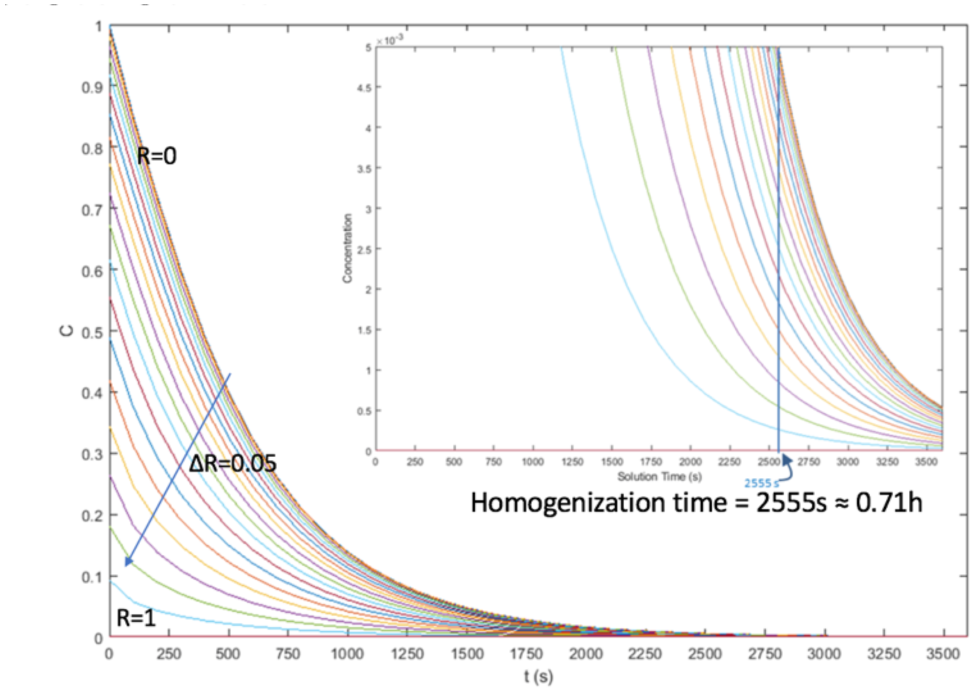

Figure 5-35: The homogenization curve of Zn in the Al-4Zn-1Mg-1.2Fe alloy, based on the homogenization model, using D = 6.10e-15m^2/s. The inlay graph is the magnified section to show that it takes 2555s for C=0.005, which was assumed to be complete homogenization of the Al grain.

To verify this homogenization time, the experimental data obtained for Zn with 1h solution treatment was used as the input for MATLAB to calculate its homogenization time with D = 6.10e-15m^2/s. The resultant graph can be seen in Figure 5-36, where the initial C was 1.8e-3, thus signifying that homogenization was complete before 1h (3600s).

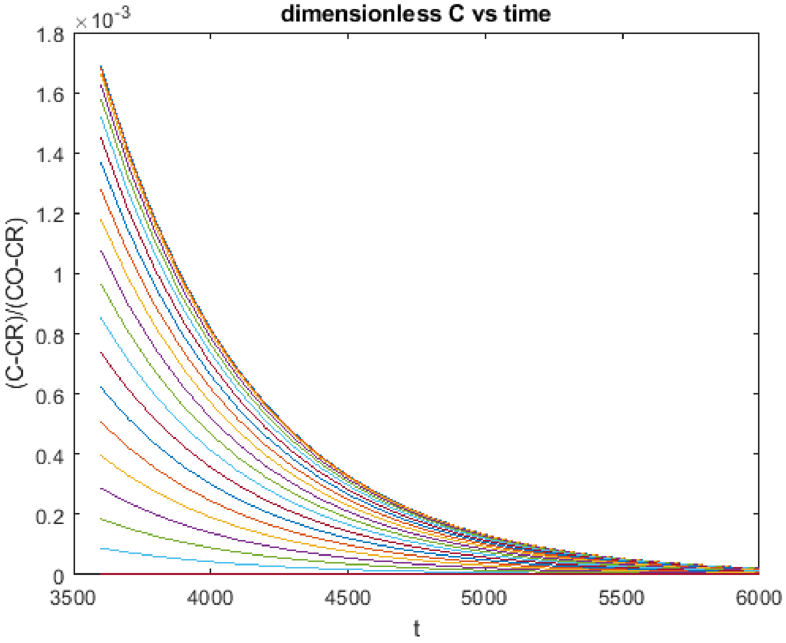

Figure 5-36: The homogenization curve of Zn, calculated using the 1h data obtained from EDX line scans as initial condition in Equation 5-4 and D = 6.10e-15m^2/s.

5.6.3.2 Diffusion of Magnesium

From the homogenization curves plotted in Figure 5-37 using the MATLAB simulation, it suggests that for an 11.5 μm diameter grain (which is approximately equivalent to the average grain size), using the lowest diffusion coefficient from Table 5-9 (3.81e-14 m^2/s), the time for complete homogenization was about 475 s. Therefore, it was concluded that the homogenization of solute Mg was always completed before that of solute Zn in solid Al grain matrix.

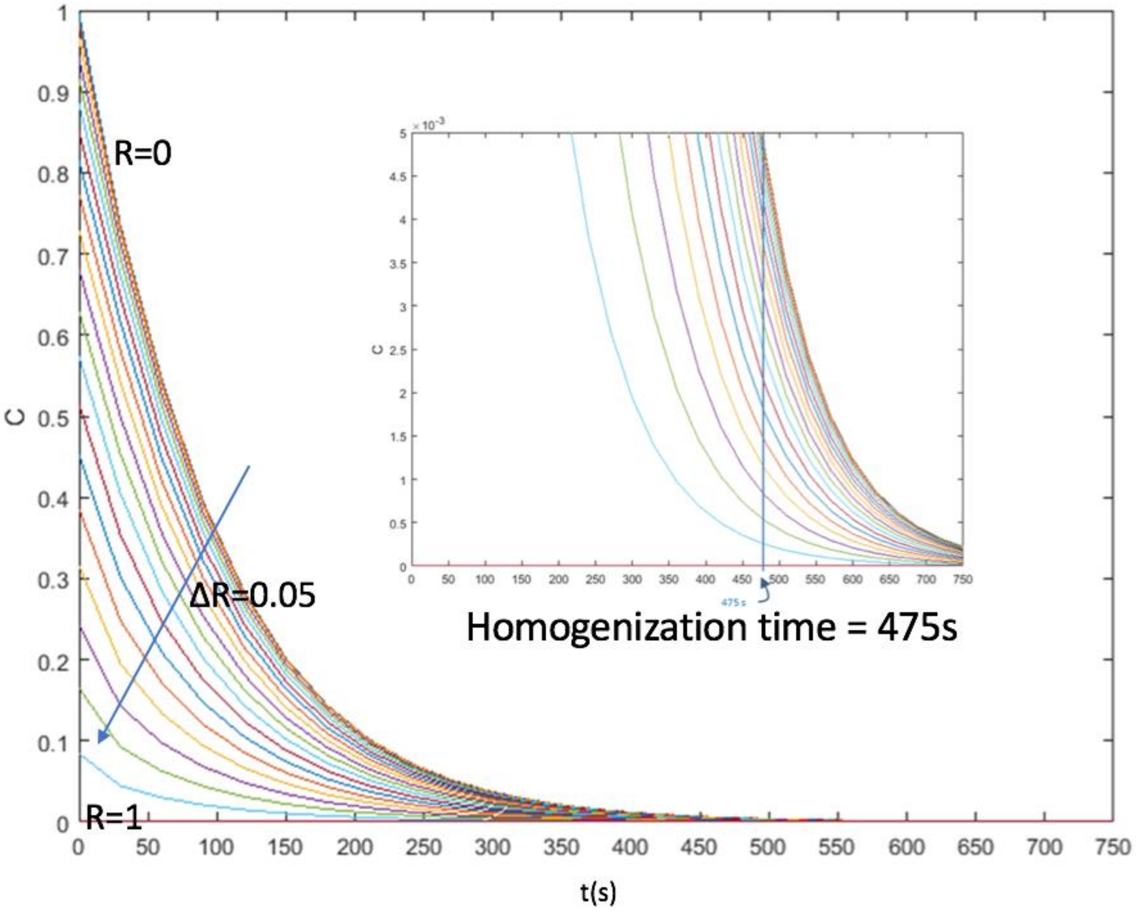

Figure 5-37: The dimensionless concentration vs. time in seconds for the homogenization of Mg, using the diffusion constant, D = 3.81e-14 m^2/s. (a) shows the entire homogenization curve at C = 0.005 is approximately 475s.

In order to make this homogenization model applicable for multiple applications, a relationship between grain size and homogenization time was evaluated. With the established relationship, the homogenization time needed for the largest grain diameter or average grain size could be determined, as well. The concentration profiles for solute Zn in the Al grains of the as-cast condition, ranging from 5.1μm to 11.34 μm in diameter, were used and the homogenization times were determined. A graph (Figure 5-38) was plotted based on these results. A first order equation was fitted to the graph and extrapolated to determine the relationship of homogenization time and grain size (GS), as given in Equation 5-20.

Equation 5-20 $GS = 0.\cdot 194t^{\frac{1}{2}}$

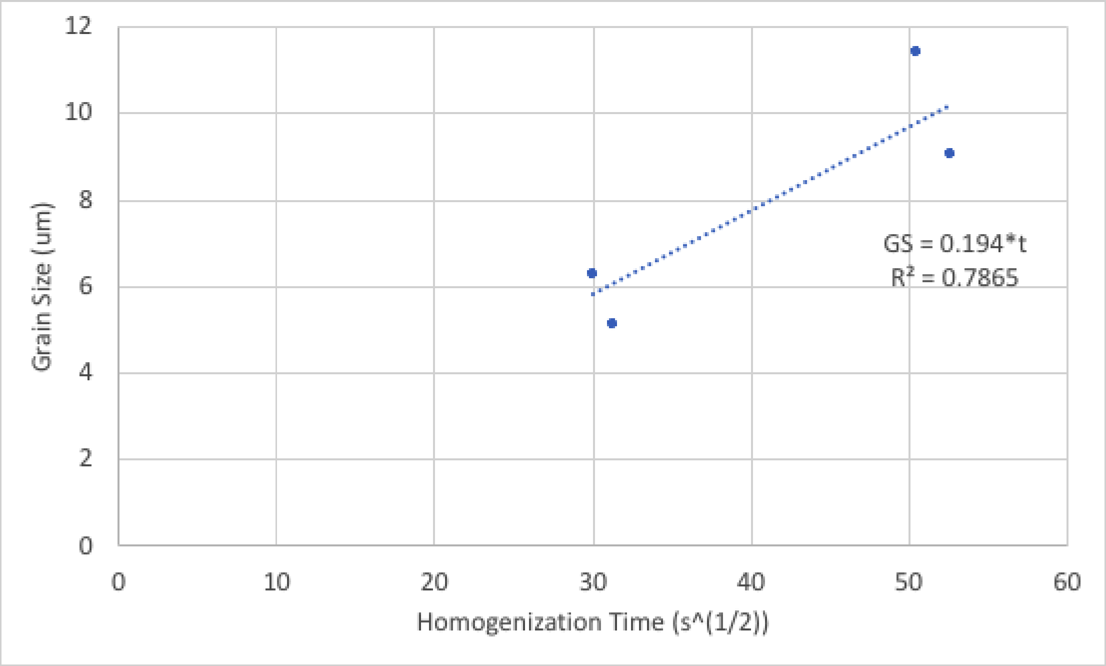

Figure 5-38: The plotted relationship between homogenization time and grain size of the Al-4Zn-1Mg-1.2Fe-0.1Ti alloy.

Chapter 6 CONCLUSIONS AND FUTURE WORK

6.1 Conclusions

The newly developed 7xxx series, Al-4Zn-1Mg-1.2Fe-0.1Ti alloy, cast using HVHPDC, proves to be a favourable candidate for structural automotive applications. The uniaxial tensile properties of the alloy castings showed similar elongation as that of the current state-of-the-art structural alloy components in A365, while, the tensile and yield strengths was notably higher. Further, the grain size of the alloy was about 11 μm and was quite uniformly consistent throughout the sample microstructure. The addition of iron in this alloy improves its hot tearing tendencies by forming favourable Al-Fe intermetallics at high solidification rates (Al_6Fe and Al_mFe) that increases the liquid feeding in the interdendritic channels during the last stages of solidification. Further, the Fe addition also mitigated the problem of die soldering, wherein, the molten metal bonds with the die tool due to a diffusion reaction. The addition of Ti alters the morphology of the primary Al-grains from dendritic to equiaxed, by the process of grain refinement; decreasing the hot tearing tendency of the alloy.

It is noteworthy that the tensile properties and microstructure obtain in the castings of this study could be significantly improved by eliminating the presence of Pre-Solidified Grains (PSG) in the cast microstructure. PSG can be alleviated by optimizing the casting parameters; specifically, the thermal management of the shot sleeve and die tool so as to prevent any premature solidification of the alloy melt prior to filling the die cavity. Apart from reducing the PSG, castings obtained with optimum filling and solidification conditions showed a significant reduction in gas and shrinkage porosities, as well. The presence of PSG could be detected by analyzing the HVHPDC shot profiles, wherein, a notable spike in the pressure (hump) is observed during the slow shot section of the pressure profile when there are PSG in the liquid metal that is being injected in the mould. Elimination of these *humps* could be carried out by one or more of increasing the alloy melt temperature, increasing the temperature of the shot sleeve and minimizing the distance in the shot sleeve when the transition of slow shot to fast shot takes place.

The microstructure of the cross-section of the casting revealed a thick skin section, approximately 250μm in size, which is at least three times wider than those obtained for castings with the conventional A365 alloy. Larger skin imparts more beneficial properties and performance to the casting such as in static and dynamic loading, high strain rate loading and corrosive environments. The secondary phases of the alloy was analyzed to be mostly Al_mFe/Al_6Fe, with a small percentage of σ-$Mg(Al,Zn)_2$ that did not dissolve with increased solutionizing time. The prediction by the solidification simulation using Scheil-Gulliver paradigm revealed that only the $Al_{13}Fe_4$ was terminal solidified phase apart from primary Al grains; however, the rapid heat extraction in the HVHPDC process suppresses the formation of the detrimental $Al_{13}Fe_4$ with its plate-like morphology and promoted the formation of the Al_mFe and Al_6Fe phases (~3 area % of microstructure) which have a more favourable script-like morphology. Further, the σ-$Mg(Al,Zn)_2$ formed as a non-equilibrium phase (~0.2 area% of microstructure) on the grain boundaries and the small fraction of these phases did not seem to pose any significant threat to the properties and performance of the alloy.

The as-cast tensile properties showed that the alloy castings could be used in the F temper state due to the high strength and elongation exhibited. Further, a T4 solutionizing heat treatment further improved the tensile properties (strength and elongation) from the homogenization of the solutes (Mg and Zn) in the primary Al grain matrix. It was shows that, an average grain size of about 11 μm would take about 2600 s to nearly complete the homogenization of all the solutes in the grains. Typically, Zn has a significantly slower mobility than Mg, in the Al matrix and as such determines the rate of homogenization. A quantitative relationship between the grain size and time to complete homogenization has been presented for future reference. The quenching of the castings with forced air (~4 °C/s at the start of the quenching) presented a viable substitute to quenching in water at ambient temperature. The latter quenching process imparted distortions in the cast component and residual stress fields in the casting, both of which would require elimination by other secondary post processes after casting and add capital and operations costs.

The combination of solutes in this alloy presents a unique scenario in that, the alloy continues to age at room temperature in both the F and T4 tempers due to the mobility of the Zn and Mg atoms and formation of the GP-I precipitates zones in the primary Al grain matrix. The rate of ageing in ambient conditions after quenching from the T4 treatment was quantified through measurement of transient hardness values for the matrix bulk. The rate of formation of GP-I precipitate zones was quantified for various samples quenched after various solution treatment times at 475 °C. It was found that as the solution treatment time increased, the rate of formation of GP-I zones at ambient conditions also increased.

The observations and results of this project have shown that the Al-4Zn-1Mg-1.2Fe-0.1Ti alloy is a viable candidate for structural automotive casting applications and presents a less expensive options to the current state-of-the-art.

6.2 Future work

This project attempted to present a first look into the viability of using the Al-4Zn-1Mg-1.2Fe-0.1Ti alloy for structural automotive casting applications and presented critical quantitative information necessary to carry out a sound casting process to produce high integrity components. The outcome of this project has shown that this alloy seems to be a better substitute to the current Al-Si-Mg based systems such as Silafont 36, Mercalloy, Castasil, etc., and hence, significant research and development work would have to be carried out in further evaluating and improving on the alloy and casting performance; some of the salient ones are presented herein.

- A fully automatic HVHPDC process with minimal to no manual intervention would be necessary to cast components with the optimal microstructure.
- Characterization of the mechanical properties of under static, dynamic and high strain rate loading conditions. These could be carried out at both room temperature and at higher temperatures that are akin to automotive operations.
- Transmission electron Microscopy (TEM) to characterize the nature and distribution of Al_mFe and Al_6Fe phases in the microstructure and relate their volume fraction ratios in the microstructure to the casting wall thickness of the location.
- Explore the viability of joining these alloy castings to the automotive superstructure through conventional processes such as riveting and friction stir welding.
- There is a remarkably wide range of precipitation hardening treatments available for this alloy due to the flexibility in controlling the state of the solutes, Zn and Mg in the Al matrix. Hence, an elaborate R&D effort to better understand the range of artificial ageing possible for this

alloy to attain several variations of T6 (near peak age) and T7 (overage) conditions is necessary to realize the additional potential of this alloy.

- In case the alloy is adopted for structural automotive component manufacturing, then studies on the solidification and shrinkage characteristics of the alloy is mandatory, in addition to evaluation of critical thermo-physical properties of the same, such as thermal conductivity, specific heat capacity, density, electrical conductivity, etc. so as to develop a database for simulation of filling and solidification using models. Further, the flow behaviour of the alloy would also need characterization.
- The deformation maps for the alloy at various temperatures would have to be developed to incorporate the alloy in finite element models to better design the components manufactured with this alloy; to realize the entire lightweighting potential of the same.
- The design of the HVHPDC die tool used in net shaped casting this alloy would have to be carried out with evaluated properties of the alloy and its solidification characteristics.

APPENDIX

The MATLAB Code for simulation of solute homogenization during T4 solution treatment. The code evaluates the following solution:

$$C_n(r,t) = \sum_{n=1}^{\infty}\left[A_n \frac{\sin(\omega_n r)}{r} e^{-\omega_n^2 Dt}\right]$$

$$where, \quad \omega_n = \frac{n\pi}{R} \quad for\, n = 1, 2, 3 \ldots \ldots \infty$$

$$and, \qquad A_n = \frac{2}{R}\int_0^R \{r \cdot f(r) \cdot \sin(\omega_n r)\} dr$$

```
%%%%%%%%%%%%%%%%%%%%%%%%%%%%%%%%%%%%%%%%%%%%%%%%%%%%%%%%%%%%%%%%%%%%%%%%%%
%
%%%%%%%%%%%%%%%%%%%%%%%%HOMOGENIZATION MODEL CODE
V.001%%%%%%%%%%%%%%%%%%%%
%Code: Homogenization Model V.001
%About: this code is used to calculate analytical solution.
%supervisor: Sumanth Shankar, shankar@mcmaster.ca
%Researcher: Chufan Wu, wuc44@mcmaster.ca
%Developer: Mohamed A. Salim, salimm3@mcmaster.ca
%All rights reserved
%%%%%%%%%%%%%%%%%%%%%%%%%%%%%%%%%%%%%%%%%%%%%%%%%%%%%%%%%%%%%%%%%%%%%%%%%%
%
%inputs
fr=input('enter fr matrix name(C at zero time as radial distance(m) is
first column and C(t=0) is second column:');
r1=fr(:,1);
R=r1(end);
sta=input('Does the fr data is dimensional or not? if yes enter(Yes),if
not enter (No) as string');
deg=input('enter degree of polynomial for fr fitting:');
D=input('enter diffusion coefficient,(m2/Sec):');
ti=input('enter the initial time: ');
dt=input('enter time step,(Sec):') ;
tf=input('enter final time,(sec):');
dr=input('enter radial step for final calculations :');
N=input('enter the maximum value of n ((for summation),Recommended
value=1000):');
ou=input('enter name of output file')
%%%%%%%%%%%%%%%%%%%%%%%%%%%%%%%%%%%%%%%%%%%%%%%%%%%%%%%%%%%%%%%%%%%%%%%%%%
%
%processing
tic
switch sta
    case 'Yes'
    frc=(fr(:,2)-fr(end,2))./(fr(1,2)-fr(end,2))  ;
    otherwise
    frc=fr(:,2);
```

```
end
A=num2str(deg);
degree=strcat('poly',A);
[a b]=fit(r1,frc,degree);
frcf=feval(a,r1);
xx=struct2cell(b);
R2=cell2mat(xx(2));
RMSE=cell2mat(xx(5));
ff=polyfit(r1,frc,2);
syms r n
fr2=(r.*poly2sym(ff,r)).*(sin((n.*pi().*r)./R)).*(2./R);
An=(int(fr2,r,[0 R]));
w=(n.*pi())./R;
rr=1e-14:dr:R;
NNN=length(rr);
rr(NNN+1)=R;
t=ti:dt:tf;
for j=1:1:length(t)
    for i=1:1:length(rr)
        for ii=1:1:N
        Anv=double(subs(An,ii));
        wv=double(subs(w,ii));
        q(ii)=(Anv).*(sin(wv.*rr(i))./rr(i)).*(exp(-wv.^2.*D.*t(j)));
        end
        C(i,j)=sum(q);
    end
end
%%%%%%%%%%%%%%%%%%%%%%%%%%%%%%%%%%%%%%%%%%%%%%%%%%%%%%%%%%%%%%%%%%%%%%%%%%%
%
%outputs and postprocessing
%plotting
figure(1)
r1=(r1./R)
plot(r1,frc,r1,frcf)
xlabel('r/R');
ylabel('(C-CR)/(CO-CR)');
legend('F(r) without fitting','F(r) with fitting')
text(r1(3),frc(5),strcat('RMSE=',num2str(RMSE)))
text(r1(3),frc(7),strcat('R2=',num2str(R2)))
title('dimensionless C vs dimensionless r');
n=size(C);
rr=(rr.')./R;
figure(2)
for i=1:1:n(2)
    plot(rr,C(:,i))
    hold on
end
xlabel('r/R');
ylabel('(C-CR)/(CO-CR)');
title('dimensionless C vs dimensionless r');
hold off
figure(3)
for i=1:1:n(1)
    plot(t,C(i,:))
    hold on
end
xlabel('t');
```

```
ylabel('(C-CR)/(CO-CR)');
title('dimensionless C vs time');
hold off
AA=strcat(ou,'.xlsx')
xlswrite(AA,r1,1)
xlswrite(AA,t,2)
xlswrite(AA,C,3)
toc
%%%%%%%%%%%%%%%%%%%%%%%%%%%%%%%%%%%%%%%%%%%%%%%%%%%%%%%%%%%%%%%%%%%%%%%%%%
%
%for more information:M.A.Salim, salimm3@mcmaster.ca
%july,2019
%%%%%%%%%%%%%%%%%%%%%%%%%%%%%%%%%%%%%%%%%%%%%%%%%%%%%%%%%%%%%%%%%%%%%%%%%%
%
```

REFERENCES

---

[1] D. A. Buckingham, "United States Geographical Studies," USGS, rep., Jan. 2006.
[2] "Sources of Greenhouse Gas Emissions," *Sources of Greenhouse Gas Emissions - Transportation*, 08-Aug-2019. [Online]. Available: https://www.epa.gov/ghgemissions/sources-greenhouse-gas-emissions.
[3] A. Bandivadekar, *On the road in 2035: reducing transportations petroleum consumption and GHG emissions*. Cambridge, MA: Massachusetts Institute of Technology, 2008.
[4] S. Angel and L. Mansueti, "National Action Plan for Energy Efficiency Vision for 2025: A Framework for Change," National Action Plan for Energy Efficiency (2008), rep., Nov. 2008.
[5] J. G. Kaufman and E. L. Rooy, *Aluminum alloy castings: properties, processes, and applications*. Schaumburg, IL: American Foundry Soc., 2007, pp. 2-13.
[6] M. Thirugnanam, "Modern High Pressure Die-casting Processes for Aluminium Castings" in *Int. Exh. of Foundry Technology, Equipment, Supplies and Services, Chennai, Tamil Nadu, India, January 19-23, 2013*
[7] R. N. Lumley, *Fundamentals of Aluminum Metallurgy*. Woodhead, 2011, pp. 263-303.
[8] Sumanth Shankar, Private communications, Mechanical Engineering Department, McMaster University, Hamilton, ON, Canada, L8S 4L8
[9] Sumanth Shankar, Private communications, Mechanical Engineering Department, McMaster University, Hamilton, ON, Canada, L8S 4L8
[10] http://rheinfelden-alloys.eu/en/alloys/silafont/#si36
[11] Sumanth Shankar, Private communications, Mechanical Engineering Department, McMaster University, Hamilton, ON, Canada, L8S 4L8
[12] J. R. Davis, *Alloying: understanding the basics*. Materials Park, OH: ASM International, pp. 351-415, 2011.
[13] S. K. Kulkarni. "*Study of effect of process parameter setting on porosity levels of aluminium pressure die casting process using Taguchi Methodology*". IOSR Journal of Mech. and Civ. Eng.
[14] G. T. Kridli, P. A. Friedman, and J. M. Boileau, *Materials, Design and Manufacturing for Lightweight Vehicles*: Woodhead Publishing, 2016, pp. 236-274.
[15] P. Kapranos, D. Brabazon, and T. Haga, *Comprehensive Materials Processing*. Elsevier, vol. 5, pp. 3-37, 2014.
[16] K. G. Swift and J. D. Booker, *Process Selection: from Design to Manufacture*, 2nd ed. London: Butterworth-Heinemann, pp. 35-61, 2006.
[17] "Die Casting 101: Hot Chamber vs. Cold Chamber: Blog," *Chicago White Metal Casting*. [Online]. Available: https://www.cwmdiecast.com/blog/2016/05/24/die-casting-101-hot-chamber-vs-cold-chamber/.
[18] P. Sharifi, "Process-Structure-Property relationships for High Pressure Die-cast Magnesium Alloys," thesis, 2017.
[19] https://pdfs.semanticscholar.org/cb44/af0a47ae8f1b237cc5208459999ece093821.pdf
[20] M. Sirviö, S. Vapalahti, J. Väinöla, *Complete Simulation of High Pressure Die Casting Process*
[21] "SOUNDCAST (Vacuum-assisted high pressure die castings with reduced porosity at low cost)," CORDIS, rep., Nov. 2015.

[22] X. Li, S. M. Xiong, Z. Guo, *Improved mechanical properties in vacuum assisted high-pressure die casting of AZ91D alloy*, Jour. of Matls. Processing Tech., vol. 231, pp. 1-7, 2016

[23] R. Lumley, N. Deeva, and M. Gershenzon, "An Evaluation of Quality Parameters for High Pressure Die Castings," *International Journal of Metalcasting*, vol. 5, no. 3, pp. 37–56, 2011.

[24] Z. Chen, "Skin solidification during high pressure die casting of Al–11Si–2Cu–1Fe alloy," *Materials Science and Engineering: A*, vol. 348, no. 1-2, pp. 145–153, 2003.

[25] K. V. Yang, M. Easton, and C. Cáceres, "The development of the skin in HPDC Mg–Al alloys," *Materials Science and Engineering: A*, vol. 580, pp. 191–195, 2013.

[26] R. Kendrick, G. Muneratti, and F. Voltazza, "The use of Metal Treatment to control the quality of an Aluminium casting produced by the High Pressure Diecasting Process," *Metallurgical Science and Technology*, vol. 30, no. 2, pp. 3–11, 2012.

[27] J. T. Black and R. A. Kohser, *DeGarmo's Materials and Processes in Manufacturing*, 10th ed. Wiley, pp. 268-272, 2008.

[28] R. C. Zeng, K. Jiang, and S.-Q. Li, "Mechanical and corrosion properties of Al/Ti film on magnesium alloy AZ31B," *Frontiers of Materials Science*, vol. 9, no. 1, pp. 66–76, 2014.

[29] M. Uludağ, R. Çetin, and D. Dispinar, "Characterization of the Effect of Melt Treatments on Melt Quality in Al-7wt %Si-Mg Alloys" *Metals*, vol. 7, no. 5, p. 157, 2017.

[30] Sumanth Shankar, Private communications, Mechanical Engineering Department, McMaster University, Hamilton, ON, Canada, L8S 4L8

[31] M. Uludag, R. Cetin, and D. Dispinar, "Characterization of the Effect of Melt Treatments on Melt Quality in Al-7wt %Si-Mg Alloys," *Metals*, vol. 7, no. 157, 2017.

[32] B. Vanko, L. Stanček, and R. Moravčík, "EN AW-2024 Wrought Aluminum Alloy Processed by Casting with Crystallization under Pressure," *Strojnícky casopis – Journal of Mechanical Engineering*, vol. 67, no. 2, pp. 109–116, Jan. 2017.

[33] C. M. Gourlay, A. K. Dahle, and H. I. Laukli, "Segregation band formation in Al-Si die castings," *Metallurgical and Materials Transactions A*, vol. 35, no. 9, pp. 2881–2891, 2004.

[34] A. Dahle and D. Stjohn, "Rheological behaviour of the mushy zone and its effect on the formation of casting defects during solidification," *Acta Materialia*, vol. 47, no. 1, pp. 31–41, 1998.

[35] X. Li, S. Xiong, and Z. Guo, "On the porosity induced by externally solidified crystals in high-pressure die-cast of AM60B alloy and its effect on crack initiation and propagation," *Materials Science and Engineering: A*, vol. 633, pp. 35–41, 2015.

[36] M.-W. Wu, X.-B. Li, Z.-P. Guo, and S.-M. Xiong, "Effects of process parameters on morphology and distribution of externally solidified crystals in microstructure of magnesium alloy die castings," *China Foundry*, vol. 15, no. 2, pp. 139–144, 2018.

[37] A. Mazahery, "Shape Casting High Strength Al-Zn-Mg-Cu Alloys: Introducing Composition-Behaviour Relationships," thesis, 2016.

[38] S. R. Ghiaasiaan, "Controlled Diffusion Solidification Process (CDS) of Al-7xxx Wrought Alloys: Heat Treatments, Microstructures and Mechanical Properties," thesis, 2015.

[39] Sumanth Shankar, Private communications, Mechanical Engineering Department, McMaster University, Hamilton, ON, Canada, L8S 4L8

[40] D. G. Eskin and L. Katgerman, "A Quest for a New Hot Tearing Criterion," *Metallurgical and Materials Transactions A*, vol. 38, no. 7, pp. 1511–1519, 2007.

[41] S. Li, "Hot Tearing in Cast Aluminum Alloys: Measures and Effects of Process Variables," thesis, 2010.

[42] I. Gómez, E. Viteri, and J. Montero, "The Determination of Dendrite Coherency Point Characteristics Using Three New Methods for Aluminum Alloys," *Applied Sciences*, vol. 8, no. 8, p. 1236, 2018.

[43] M. Rappaz, J. M. Drezet, and M. Gremaud, "A New Hot-Tearing Criterion," *Metallurgical and Materials Transactions A*, vol. 30, no. A, pp. 449–455, 1999.

[44] N. Hatami, R. Babaei, and M. Dadashzadeh, "Modeling of hot tearing formation during solidification," *Journal of Materials Processing technology*, vol. 205, no. 1-3, pp. 506–513, 2008.

[45] Pellini, W. S., "Criteria for Fracture Control Plans," Washington, D.C., Naval Research Laboratory, Report 7406 (May, 1972).

[46] S. K. Kim, Y. D. Lee, and K. Hansson, "Influence of Cooling Rate on the Hot Cracking Formation of Nickel Rich Alloys.," *ISIJ International*, vol. 42, no. 5, pp. 512–519, 2002.

[47] Pumphrey WI, Jennings PH (1948) A consideration of the nature of brittleness and temperature above the solidus in castings and welds in aluminum alloys. J Inst Metals 75: 235–256

[48] I. Durrans: Thesis–Part II, Oxford University, Oxford, United Kingdom, 1981.

[49] C. Puncreobutr, P. Lee, and K. Kareh, "Influence of Fe-rich intermetallics on solidification defects in Al–Si–Cu alloys," *Acta Materialia*, vol. 68, pp. 42–51, 2014.

[50] Z. Zhang, G. Li, and X.-G. Chen, "Effect of nickel and vanadium on iron bearing intermetallic phases in AA 5657 simulated DC castings" *Materials Science and Technology*, vol. 30, no. 8, pp. 951–961, 2013.

[51] Z. Zhang, G. Li, and X.-G. Chen, "Identification and Distribution of Fe Intermetallic Phases in AA 5657 DC Cast Ingots," *ICAA13 Pittsburgh*, pp. 1857–1863, 2012.

[52] J. G. Kaufman, *Introduction to aluminum alloys and tempers*. Materials Park, OH: ASM International, pp.39-76, 2000.

[53] Fink, W. L., Wiley, L. A., Trans. AIME 175 (1948) 414.

[54] M. Newkirk "Quench Factor Analysis for Heat Treatment Optimization of 7xxx Aluminum Alloys"

[55] M. Chemingui, M. Khitouni, G. Mesmacque, and A. Kolsi, "Effect of heat treatment on plasticity of Al–Zn–Mg alloy: Microstructure evolution and mechanical properties," *Physics Procedia*, vol. 2, no. 3, pp. 1167–1174, 2009.

[56] E. A. Ashrafi and A. Hasan, Lambert Academic Publishing, 2013.

[57] GUINIER A., Ann. Pllys. 13 (1939) 161.

[58] PRESTON G-D-, Pliilos. Mag. 26 (1938) 855.

[59] Auld, H. and Cousland, S. M.,Austr. J. Metal., 1974,19, 194.8.

[60] J. Embury and R. Nicholson, "The nucleation of precipitates: The system Al-Zn-Mg," *Acta Metallurgica*, vol. 13, no. 4, pp. 403–417, 1965.

[61] L. K. Berg and V. Hansen, "GP-ZONES IN Al–Zn–Mg alloys and their role in artificial aging," *acta materialia*, vol. 49, pp. 3443–3451, 2001.

[62] Rubio, R. A., Haouala, S., & LLorca, J. (2019). Grain boundary strengthening of FCC polycrystals. Journal of Materials Research, 1–12.doi:10.1557/jmr.2019.58

[63] Bieler, T. R., Eisenlohr, P., Zhang, C., Phukan, H. J., & Crimp, M. A. (2014). Grain boundaries and interfaces in slip transfer. Current Opinion in Solid State and Materials Science, 18(4), 212–226. doi:10.1016/j.cossms.2014.05.003

[64] W. D. Callister and D. G. Rethwisch, *Fundamentals of materials science and engineering*. Hoboken, NJ: Wiley, 2013.

[65] R. Mahmudi, "Grain boundary strengthening in a fine grained aluminium alloy," *Scripta Metallurgica et Materialia*, vol. 32, no. 5, pp. 781–786, 1995.

[66] N. Hansen, "Hall–Petch relation and boundary strengthening," *Scripta Materialia*, vol. 51, no. 8, pp. 801–806, 2004.

[67] A. Akhtar and E. Teghtsoonian, "Solid solution strengthening of magnesium single crystals—I alloying behaviour in basal slip," *Acta Metallurgica*, vol. 17, no. 11, pp. 1339–1349, 1969.

[68] Khachaturyan, "Ordering in substitutional and interstitial solid solutions," *Progress in Materials Science*, vol. 22, no. 1-2, pp. 1–150, 1978.

[69] W. Hume-Rothery, G. W. Mabbott, and K. M. Channel-Evans. The freezing points, melting points, and solid solubility limits of the alloys of silver and copper with the elements of the B Sub-Groups. Philos. Trans. R. Soc. London, Ser. A. 233, 1934, 1-97.

[70] P. W. Reynolds and W. Hume-Rothery. The constitution of silver-rich antimony-silver alloys. J. Inst. Metals. 60, 1937, 365-374.

[71] W. Hume-Rothery. Factors affecting the stability of metallic phases. In: P. S. Rudman, J. Stringer and R. I. Jaffee, eds. Phase Stability in Metals and Alloys. New York: McGraw-Hill, 1967. pp. 3-23.

[72] Starke, E.A. JOM (1970) 22: 54. https://doi.org/10.1007/BF03355628

[73] D. Lloyd, "Precipitation Hardening," *Strength of Metals and Alloys (ICSMA 7)*, pp. 1745–1778, 1986.

[74] R. E. Smallman, *Modern physical metallurgy*. London u.a.: Butterworth, pp. 499-527, 2014

[75] W. D. Callister and D. G. Rethwisch, *Materials science and engineering: an introduction*. Hoboken, NJ: Wiley, 2018.

[76] Wu, Chufan & Shankar, Sumanth & Zeng, Xiaochun & Birsan, Gabriel & Sadayappan, Kumar & Lombardi, Anthony & Byczynski, Glenn. (2018). Microstructure and Uniaxial Tensile Properties of Heat Treatable Al-Zn Alloy for Structural HPDC Components.

[77] https://compass.astm.org/EDIT/html_annot.cgi?B557M

[78] L. Backerud, E. Krol, and J. Tamminen: Solidification Characteristics of Aluminum Alloys, Vol 1: Wrought Alloys, SkanAluminum, Oslo, Norway, 1986

[79] https://www.astm.org/Standards/A833.htm

[80] https://www.astm.org/Standards/E1245.htm

[81] Gulliver, G.H., *J. Inst. Met.*, 9:120, 1913.

[82] Scheil, E., *Z. Metallk.*, 34:70, 1942.

[83] Zeng, X., Ferguson, C., Sadayappan, K., & Shankar, S. (2018). *Effect of Titanium Levels on the Hot Tearing Sensitivity and Abnormal Grain Growth After T4 Heat Treatment of Al–Zn–Mg–Cu Alloys. International Journal of Metalcasting, 12(3), 457–468.* doi:10.1007/s40962-018-0227-2

[84] "Compacted Graphite Iron Castings," *Casting*, pp. 872–883, 2008.

[85] T.G. Stoebe, R.D. Gulliver II, T.O. Ogurtani, and R.A. Huggins, Nuclear Magnetic Resonance Studies of Diffusion of Al^{27} in Aluminum and Aluminum Alloys, *Acta Metall.*, 1965, **13**(7), p 701–708
[86] J.E. Hilliard, B.L. Averbach, and M. Cohen, Self and Interdiffusion in Aluminum-Zinc Alloys, *Acta Metall.*, 1959, **7**(2), p 86–92
[87] A. Beerwald, Z. Elektrochem. 45 (1939) 789
[88] S. Fujikawa and K. Hirano, Diffusion of ^{65}Zn in Aluminum and Al−Zn−Mg Alloy over a Wide Range of Temperature, *Trans. JIM*, 1976, **17**(12), p 809–818
[89] Erdélyi, G., Beke, D. L., Kedves, F. J., & Gödény, I. (1978). Determination of diffusion coefficients of Zn, Co and Ni in aluminium by a resistometric method. Philosophical Magazine B, 38(5), 445–462.doi:10.1080/13642817808246394
[90] N. L. Peterson and S. J. Rothman, "Impurity Diffusion in Aluminum," *Physical Review B*, vol. 1, no. 8, pp. 3264–3273, 1970.